Evaporation Residue Measurements of Compound Nuclei in A ≈ 200 Region

Thesis submitted to The University of Calicut for the award of the Degree of

Doctor of Philosophy in Physics

By

Jisha P

Under the guidance of

Dr. A. M. Vinodkumar

DEPARTMENT OF PHYSICS

UNIVERSITY OF CALICUT

JULY 2023

UNIVERSITY OF CALICUT

DR. A. M. Vinodkumar
Professor
Department of Physics

Calicut University P.O.
Kerala INDIA 673 635
Tel: 0494-2407415
Fax: 0494-2400269
Mob: 9645078924
Email: amv@uoc.ac.in

DP/AMV/2023/07-04

04 July 2023

CERTIFICATION OF SUPERVISOR

This is to certify that all the corrections/suggestions from the adjudicators have been incorporated in the thesis and that the content in the thesis and the soft copy are one and the same.

University of Calicut

A M Vinodkumar

Date : 04/07/2023

UNIVERSITY OF CALICUT

DR. A. M. Vinodkumar
Professor
Department of Physics

Calicut University P.O.
Kerala INDIA 673 635
Tel: 0494-2407415
Fax: 0494-2400269
Mob: 9645078924
Email: amv@uoc.ac.in

DP/AMV/2023/07-04

04 July 2023

CERTIFICATION OF SUPERVISOR

Certified that the work presented in this thesis entitled **"Evaporation Residue Measurements of Compound Nuclei in A~200 Region"** is a bonafide work done by Ms. Jisha P under My guidance for the award of the degree of Doctor of Philosophy in Physics at the Department of Physics, University of Calicut and that this work has not been included in any other thesis submitted previously for the award of any degree and has undergone plagiarism check using OURIGINAL software at C. H. M. K. Library, University of Calicut, and the similarity index found within the permissible limit.

University of Calicut

A M Vinodkumar

Date : 04/07/2023

DECLARATION

I hereby declare that this thesis entitled "**Evaporation Residue Measurements Of Compound Nuclei In A≈ 200 Region"** is a bonafide record of research work carried out by me under the guidance of Dr. A. M. Vinodkumar (Professor, Department of Physics, University of Calicut) and that no part of this thesis has been presented before the award of any other degree or diploma.

University of Calicut

Date: 04/07/2023

Jisha P

Acknowledgments

I express my incredible gratitude to My supervisor, Dr. A. M. Vinodkumar, who inspired me to pursue a career in nuclear physics. He patiently guided me and made sure that I fully grasped the subject. His enthusiasm for nuclear physics has always served as a model to me. During the discussions with him, he encouraged me to come up with unique solutions to overcome obstacles in my research work. He has always inspired me and helped to achieve more self-assurance.

I am grateful to Dr. C. D. Ravikumar, Head, Dept. of Physics, the University of Calicut, for the help and support during my thesis submission. I would like to thank the former heads of the Physics department, Prof. Antony Joseph, Prof. M. M. Musthafa, and Prof. P. P. Predyumnan, for their prompt advice and activities throughout my research career. I also like to thank all the Calicut University Physics department faculty members for their constant encouragement and support.

My collaborator, Prof. B. R. S. Babu, deserves my gratitude for his unconditional support throughout my research. Being a very skilled teacher, he has helped me to learn the subject thoroughly. He broadened my understanding through insightful discussions throughout the experiment and constructive criticism during manuscript writing.

The experimental part of my research work has been carried out at IUAC using Pelletron and HIRA facility. I am grateful to the Pelletron group of IUAC for providing an excellent beam of the required pulse width throughout the experiment. I am indebted for the support received from the target and data support laboratories of IUAC. I especially thank the HIRA group of IUAC for their support throughout my experiment. I use this opportunity to express my sincere thanks to Dr. Subir Nath, Dr. N. Madhavan and Dr. J. Gehlot for their

constant support and active involvement in my experiments. I am extending my special gratitude to Dr. J. Gehlot for his wholehearted support throughout my research. I would like to thank all the collaborators at IUAC, Dr. A. Jhingan, Dr. T. Banerjee, Dr. Ish Mukul, Dr. R. Dubey, Mr. N. Saneesh, Mr. Rohan Biswas, Dr. A. Parihari for their constant support and help during the experiment.

I am grateful to all my collaborators Prof. K. M. Varier, former professor at Calicut university, Dr. E. Prasad, Dr. A. Shamlath, Dr. P.V. Laveen, Dr. M. Shareef, Mr. A. C. Visakh from the Central University of Kerala, Mr. A. Vinayak from Karnatak University and Mr. Amritraj Mahato from the Central University of Jharkhand for their sincere involvement during the experiment and fruitful suggestion during manuscript writing.

I think fondly of all the collogue at Calicut university, past and present, whose companionship energized me during my research career. I would like specially mention the support from my lab-mates Sanila, Arjun, Irshad, Kishan and Bijoy, with whom I spend my quality time. I am extending my special gratitude to Arjun for the technical support he provided unconditionally to me, which helped speed up my work.This acknowledgment would not be complete without mentioning Aswathi, who helped me throughout my personal and professional struggles and whom I love more as a family member than a friend.

I do not know how to express my gratitude to my family for their unconditional support throughout this Journey. I am grateful for my parents, who helped shape who I am today and have always stood by me, especially during my difficulties. I recall my husband's support during my entire research career. As a husband and friend, his support and concern for me have always made it possible for me to commit to my profession. I appreciate his listening to my concerns during my difficulties and others. I also appreciate the good company, love, and support from my sister and all other family members during these days.

Finally, I would like to acknowledge the financial support from UGC-BSR, New Delhi, for carrying out this work.

List of publication

International Journals

1. **Role of positive transfer Q values in fusion cross sections for ^{18}O+^{182,184,186}W reactions**

   P. Jisha, A. M. Vinodkumar, S. Sanila, K. Arjun, B. R. S. Babu, J. Gehlot, S. Nath, N. Madhavan, Rohan Biswas, A. Parihari, A. Vinayak, Amritraj Mahato, E. Prasad, and A. C. Visakh, Phys. Rev. C 105, 054614 (2022)

2. **Evaporation residue measurements of compound nuclei in the A≈200 region**

   P. Jisha, A. M. Vinodkumar, B. R. S. Babu, S. Nath, N. Madhavan, J. Gehlot, A. Jhingan, T. Banerjee, Ish Mukul, R. Dubey, N. Saneesh, K. M. Varier, E. Prasad, A. Shamlath, P. V. Laveen, and M. Shareef, Phys. Rev. C 101, 024611 (2020).

3. **Fusion studies in ^{35,37}Cl+^{181}Ta reactions via evaporation residue cross section measurements**

   P. V. Laveen, E. Prasad, N. Madhavan, A. K. Nasirov, J. Gehlot, S. Nath, G. Mandaglio, G. Giardina, A. M. Vinodkumar, M. Shareef, A. Shamlath, S. K. Duggi, P. Sandya Devi, Tathagata Banerjee, M. M. Hosamani, Khushboo, **P. Jisha**, Neeraj Kumar, Priya Sharma, and T. Varughese, Phys. Rev. C 102, 034613 (2020).

4. **Search for stabilizing effects of the Z=82 shell closure against fission**

   J. Gehlot, S. Nath, Tathagata Banerjee, Ish Mukul, R. Dubey, A. Shamlath, P. V. Laveen, M. Shareef, Md. Moin Shaikh, A. Jhingan, N. Madhavan, Tapan Rajbongshi, **P. Jisha**, and Santanu Pal, Phys. Rev. C 99, 061601(R) (2019)

5. **Evaporation residue cross-section measurements for ^{16}O+^{203,205}Tl**

   J. Gehlot, A. M. Vinodkumar, N. Madhavan, S. Nath, A. Jhingan, T. Varughese, Tathagata Banerjee, A. Shamlath, P. V. Laveen, M. Shareef, **P. Jisha**, P. Sandya Devi, G. Naga Jyothi, M. M. Hosamani, I. Mazumdar, V. I. Chepigin, M. L. Chelnokov, A. V. Yeremin, A. K. Sinha, and B. R. S. Babu, Phys. Rev. C 99, 034615 (2019).

6. **Investigation of fusion hindrance in a soft asymmetric system deep below the barrier**

   Md. Moin Shaikh , S. Nath , J. Gehlot, Tathagata Banerjee , Ish Mukul, R. Dubey, A. Shamlath, P. V. Laveen , M. Shareef , A. Jhingan, N. Madhavan, Tapan Rajbongshi, **P. Jisha**, G. Naga Jyothi , A. Tejaswi , Rudra N. Sahoo and Anjali Rani , J. Phys. G: Nucl. Part. Phys. 45, 095103 (2018).

7. **Fusion and quasifission studies in reactions forming Rn via evaporation residue measurements**

   A.Shamlath, E. Prasad, N. Madhavan, P. V. Laveen, J. Gehlot, A. K. Nasirov, G. Giardina, G. Mandaglio, S. Nath, Tathagata Banerjee, A. M. Vinodkumar, M. Shareef, A. Jhingan, T. Varughese, DVGRKS Kumar, P. Sandya Devi, Khushboo, **P. Jisha**, Neeraj Kumar, M. M. Hosamani, and S. Kailas , Phys. Rev. C 95, 034610 (2017)

8. **Deformation effects on sub-barrier fusion cross sections in ^{16}O+^{174,176}Yb**

   Tapan Rajbongshi, K. Kalita, S. Nath, J. Gehlot, Tathagata Banerjee, Ish Mukul, R. Dubey, N. Madhavan, C. J. Lin, A. Shamlath, P. V. Laveen, M. Shareef, Neeraj Kumar, **P. Jisha** , and P. Sharma ,Phys. Rev. C 93, 054622 (2016)

Oral/Poster presentations in International and National symposium/conferences

1. **Comparisons of evaporation residue cross-section of ^{16}O and ^{18}O induced reactions on W isotopes**

   P. Jisha, A. M. Vinodkumar, S. Sanila, K. Arjun, B. R. S. Babu, J. Gehlot, S. Nath, N. Madhavan, Biswas Rohan, A. Parihari, A. Vinayak, Mahato Amritraj, A. C. Visakh, E. Prasad ,65^{th} DAE-BRNS Symposium on Nuclear Physics, 1-5 December 2021, Bhabha Atomic Research Centre, Mumbai-400 085, India.

2. **Comparisons of fusion cross-section of ^{16}O and ^{18}O induced reactions on W isotopes**

   P. Jisha, A. M. Vinodkumar, S. Sanila, K. Arjun, B. R. S. Babu, J. Gehlot, S. Nath, N. Madhavan, Biswas Rohan, A. Parihari, A. Vinayak, Mahato Amritraj, A. C. Visakh, E. Prasad ,Centenary Celebration Conference on Nuclear Structure and Nuclear Reactions, 2-4 March, 2020 AMU, Aligarh

3. **Evaporation residue cross-section measurements for ^{16,18}O+ ^{181}Ta reactions**

   P. Jisha, A. M. Vinodkumar, B. R. S. Babu, S. Nath, N. Madhavan, J. Gehlot, A. Jhingan, T. Banerjee, Ish Mukul, R. Dubey, N. Saneesh, K. M. Varier, E. Prasad, A. Shamlath, P. V. Laveen, and M. Shareef, 64^{th} DAE-BRNS Symposium on Nuclear Physics, 23- 27 December 2019, Department of Physics, Lucknow University, Lucknow, U.P.

4. **Probing quasifission in reactions forming ^{210}Rn nucleus**

   A. Shamlath, E. Prasad, N. Madhavan, P. V. Laveen, J. Gehlot, A. K.

Nasirov, G. Giardina, G. Mandaglio, S. Nath, Tathagata Banerjee, A. M. Vinodkumar, M. Shareef, A. Jhingan, T. Varughese, D. V. G. R. K. S. Kumar, P. Sandya Devi, Khushboo, **P. Jisha**, Neeraj Kumar, M. M. Hosamani, and S. Kailas , 26th International Nuclear Physics Conference, POS (2016)

5. **Evaporation residue excitation function measurements for reactions forming Rn compound nuclei**

   A. Shamlath, E. Prasad, P. V. Laveen, N. Madhavan, J. Gehlot, A. M. Vinodkumar, A. K. Nasirov, G. Giardina, G. Mandaglio, S. Nath, M. Shareef, Tathagata Banerjee, A. Jhingan, T. Varughese, DVGRKS Kumar, P. Sandya Devi, Khushboo, **P. Jisha**, Neeraj Kumar, M. M. Hosamani, S. Kailas,61^{st} DAE-BRNS Symposium on Nuclear Physics, 2-6 December 2016, Variable Energy Cyclotron Centre, Kolkata.

6. **Measurement of sub-barrier fusion cross sections for ^{19}F+^{181}Ta**

   Md. Moin Shaikh, S. Nath, J. Gehlot, Tathagata Banerjee, Ish Mukul, R. Dubey, A. Shamlath, P. V. Laveen, M. Shareef, A. Jhingan, N. Madhavan, T. Rajbongshi, **P. Jisha**, 61^{st} DAE-BRNS Symposium on Nuclear Physics, 2-6 December 2016, Variable Energy Cyclotron Centre, Kolkata.

7. **Measurement of ER cross-sections across $Z = 82$ shell closure**

   J. Gehlot, S. Nath, Tathagata Banerjee, Ish Mukul, R. Dubey, A. Shamlath, P. V. Laveen, M. Shareef, Md. Moin Shaikh, A. Jhingan, N. Madhavan, T. Rajbongshi, **P. Jisha**, Santanu Pal, 61^{st} DAE-BRNS Symposium on Nuclear Physics, 2-6 December 2016, Variable Energy Cyclotron Centre, Kolkata.

8. **Evaporation residue excitation function for ^{30}Si + ^{180}Hf**

   A. Shamlath, E. Prasad, N. Madhavan, S. Nath, J. Gehlot, A. M. Vin-

odkumar, M. Shareef, P. V. Laveen, A. Jhingan, T. Varughese, Tathagata Banerjee, DVGRKS Kumar, P. Sandya Devi, Khushboo, **P. Jisha**, Neeraj Kumar, M. M. Hosamani, S. Kailas, 60^{th} DAE-BRNS Symposium on Nuclear Physics, 7-11 December 2015, Sri Sathya Sai Institute of Higher Learning, Prasanthi Nilayam, Andhra Pradesh.

9. **ER excitation function measurement for the ^{35,37}Cl+^{181}Ta reactions**

   P.V. Laveen, E. Prasad, N. Madhavan, S. Nath, J. Gehlot, A.M. Vinodkumar, A. Jhingan, T. Varughese, Tathagata Banerjee, DVGRKS. Kumar, P. Sandya Devi, M. Shareef, Khushboo, A. Shamlath, **P. Jisha**, Priya Sharma, Neeraj Kumar, M.M. Hosamani,60^{th} DAE-BRNS Symposium on Nuclear Physics, 7-11 December 2015, Sri Sathya Sai Institute of Higher Learning, Prasanthi Nilayam, Andhra Pradesh.

10. **Influence of hexadecapole deformation on fusion for ^{16}O + ^{174,176}Yb systems**

    Tapan Rajbongshi, K. Kalita, S. Nath, N. Madhavan, J. Gehlot, I. Mukul, Tathagata Banerjee, R. Dubey, T. Varughese, A. Shamlath, P.V. Laveen, M. Shareef, Priya Sharma, NeerajKumar, **P. Jisha**, 60^{th} DAE-BRNS Symposium on Nuclear Physics, 7-11 December 2015, Sri Sathya Sai Institute of Higher Learning, Prasanthi Nilayam, Andhra Pradesh.

Contents

List of Figures

List of Tables

Chapter 1

Introduction

Heavy-ion reactions are crucial tools in nuclear physics for understanding the internal structure and characteristics of the nucleus. The developments of accelerators and thereby the availability of heavy-ion beams helped the physicist to understand the complex heavy-ion reaction dynamics and the nuclear structure. Heavy-ion fusion reactions are significant as they are the most successful mechanisms for super-heavy element (SHE) production. In fusion reactions, a projectile-target system fuse together and a complex composite system called compound nuclei (CN) is formed [1]. The fused system, thus formed is a very intricate many-body system that can disintegrate via several pathways. The intricacies occur due to the dramatic changes in the fusion dynamics with the increasing mass, energy, and angular momenta of the heavy-ion. The studies on SHE production resulted in the discovery of various non-compound nuclear fission (NCNF) reaction mechanisms, such as pre-equilibrium emission fast-fission [2, 3] and quasi-fission [4, 5], which reduce the probability of complete fusion. Different dynamical and statistical models have been proposed to understand these nuclear processes in different energy regimes. Contributions from heavy-ion reactions have introduced several factors which will affect super-heavy element production. Still, a comprehensive understanding of the factors affecting super-heavy element production is missing.

CNs produced in the mass region of ≈ 200 have shown NCNF reactions, even

in a highly asymmetric combination of a projectile-target system. The existence of CN formation along with NCNF in the A $\approx$ 200 region makes this mass region an active research topic. A comprehensive idea of the reaction mechanisms in the A $\approx$ 200 regions will be helpful while studying the fusion hindrances in SHE production [6, 7].

1.1 Nuclear Reactions and their classification

In heavy ion fusion, attractive nuclear and repulsive Coulomb and centrifugal forces will come into play when two nuclei come closer. The presence of these opposing forces produces a barrier and a potential pocket inside it. The projectile can fuse and decay via various modes if it has sufficient energy to overcome the repulsive barrier. The decay mechanisms involved in heavy ion reactions depend on the mass, energy, and angular momentum of colliding nuclei.

Classically these collisions can be described in terms of the impact parameter (b), which is the perpendicular distance between the center of force and the incident beam direction. The concept of classical trajectory is valid in heavy ion collisions as the associated De Broglie wavelength is much smaller than the dimensions involved. Different processes involved in nuclear interaction as a function of impact parameter is depicted in Fig. 1.1.

Various direct reactions can be identified based on the impact parameters. When the impact parameter is too large, such collisions are known as distant collisions. In distant collisions, the projectile-target system is within the range of nuclear forces for a short time ($< 10^{-22}$ s). In such situations, elastic scattering is the most dominant scattering mechanism. As the most peripheral collisions (larger value for impact parameter), the angular momentum transfer associated with such collisions are higher than in other collisions. When impact parameter $b \sim b_{gr}$ (the grazing impact parameter), the grazing collisions sets in. Nuclei begin to experience nuclear interactions in such collisions. In grazing collisions, quasi-elastic reactions begin to dominate. Quasi-elastic reactions include inelas-

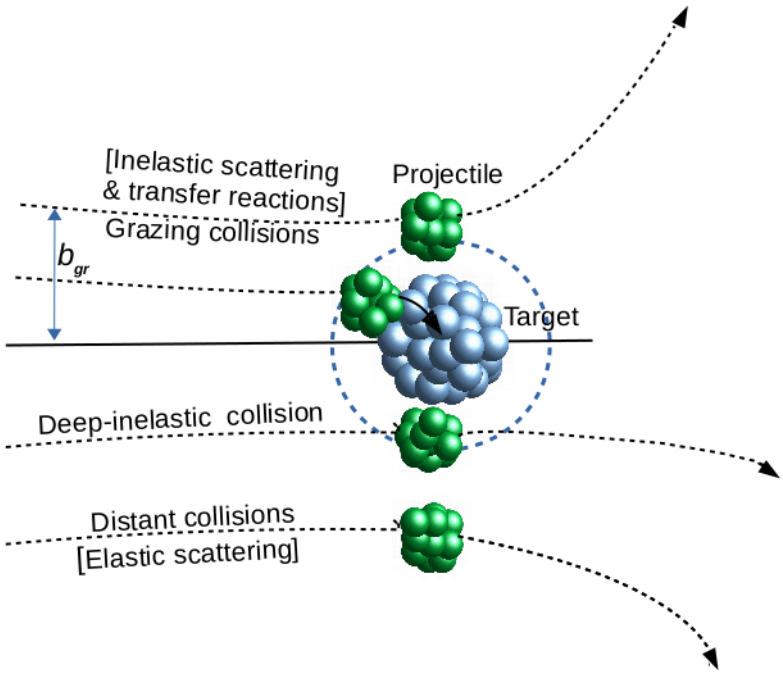

Figure 1.1: Collision categorization schematics based on impact parameter.

tic excitations, break-up reactions and transfer reactions. In transfer reactions, one or more nuclei are transferred between the projectile and the target. When the impact parameter is further reduced from b_{gr}, deep inelastic scattering (DIS) occurs. During DIS, a significant fraction of kinetic energy and angular momentum are converted to internal excitations. Also, projectile nuclei keep their identity up to a net exchange of a few nucleons even though a large amount of energy transfer occurs. Central collisions result in the fusion of the projectile with the target and form a composite system called the compound nucleus.

1.2 Compound nucleus formation and decay mechanisms

Head-on collisions of the projectile and the target lead to a highly excited composite system called compound nucleus (CN). Each nucleon in the projectile and

target is involved in CN-type reactions. Through several collisions, the nucleons of the colliding partners share total kinetic energy, angular momentum and mass. The angular momentum transfer associated with head-on collisions is lower than in other collisions with higher impact parameters. The average increase in energy of nucleons is not enough to free them from the nucleus. Thus, the formed composite system takes a long time (10^{-18}- 10^{-15} s) to equilibrate. This thermally equilibrated composite system loses its memory of how it was formed and de-excite to the ground state either by the emission of particles (neutron, protons, alphas, etc.) and gamma rays or by fission [8, 9]. Neutron emission is the most probable decay mechanism for asymmetric systems at lower energy and angular momentum [8]. Residual nuclei left after the particle emission were referred to as evaporation residue (ER), an entity almost identical to CN. Neutron emission is the most probable decay mode, even for highly proton-rich CN. Thus heavy-ion reactions act as an excellent tool to search for stable or nearly stable super-heavy elements [10]. Often, due to its high excitation energy and fissility, the equilibrated CN reaches a mass-symmetric contact configuration through shape oscillations and eventually goes by binary fission [9]. Compound nucleus formation generally dominates in low and medium-energy heavy mass systems, where the projectile has a small chance of escaping from the composite system.

Another unique characteristic of CN-type reactions is the transfer of a large amount of angular momentum to CN even at lower impact parameters. Such angular momentum transfer even occurs at higher energies. In such high energies, merely passing through the fusion barrier does not guarantee the formation of CN. At such high energy and angular momentum, nuclear force fails to provide necessary centripetal forces [10]. The possible potential pocket can also vanish at such a high angular momentum and the system will not have enough time to equilibrate before re-separation. This leads to the evolution of an elongated, completely unstable nuclear entity called a di-nuclear system (DNS) [11, 12]. Before complete equilibration, DNS, which retains a considerable memory of its formation, breaks into the same configurations of

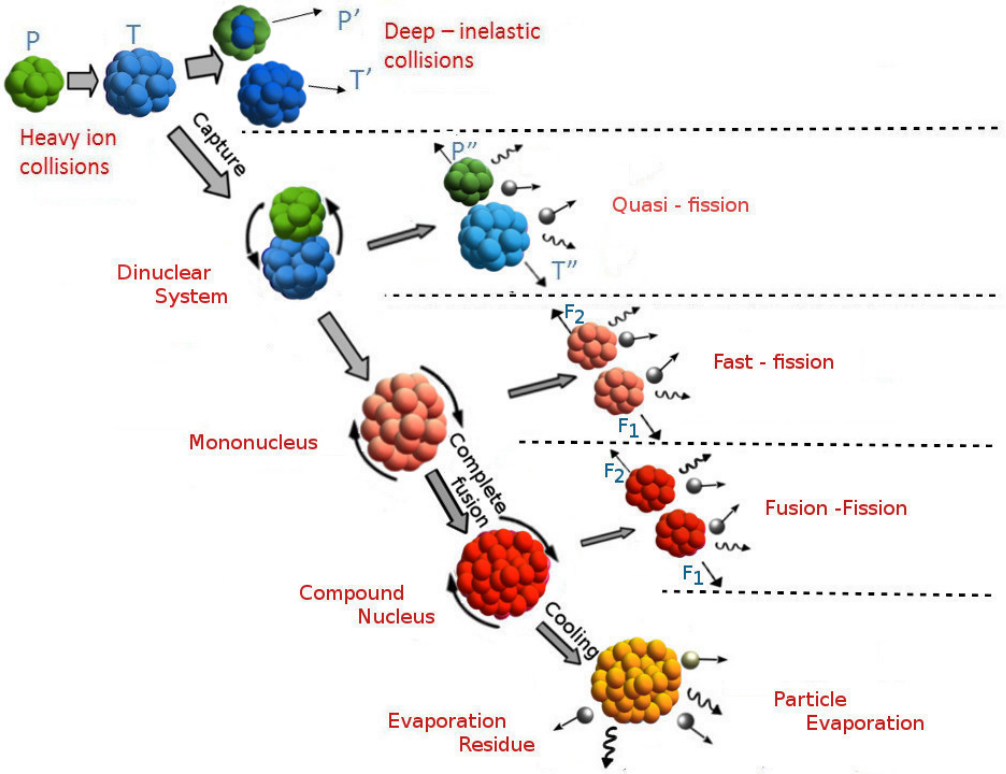

Figure 1.2: A schematic diagram of the CN produced during a heavy-ion fusion process.

the incident particle and is known as quasi-fission (QF) [11, 13, 14]]. Fast fission (FF) [2, 3] is another process that dominates at higher energies. Processes such as QF, FF, etc., are known as non-compound nuclear fission (NCNF), as no CN is produced during these processes. They generally act as hurdles to the production of super-heavy elements. A dramatic change in reaction mechanism occurs for collisions with charge product $Z_P Z_T$ $\geq$1600 [15]. In the case of reactions with massive nuclei, the DNS and compound nuclei break down into two parts. A splitting of DNS is called quasi-fission, while that of CN is called fusion-fission. The difference between fusion-fission, fast-fission and quasi-fission processes is schematically demonstrated in Fig. 1.2. After capture the composite system passes through many stages before forming a CN. The intermediate steps involved in heavy-ion fusion are so high in numbers, that they can only be handled using statistical models.

All the reactions described in terms of impact parameters (Fig. 1.1) can

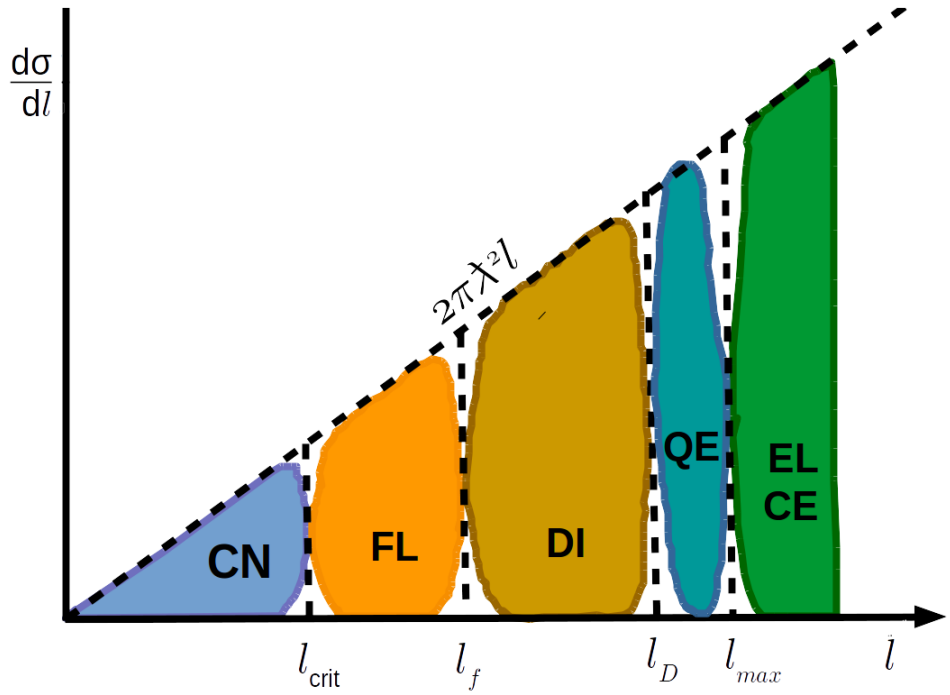

Figure 1.3: Schematic illustration of the angular momentum dependence of the partial cross-section for CN nucleus (CN), fusion like(FL), deep inelastic (DI), quasi-elastic (QE), Coulomb excitation (CE), and elastic (EL) processes.

also represent in terms of angular momentum transfer associated with each of them. In Fig. 1.3, the spin distribution ($d\sigma/d\ell$) of various reactions is shown as a function of angular momenta. The areas below different curves represents the corresponding cross-sections. The elastic scattering being the most peripheral collision, angular momentum ℓ associated with such collisions will be the highest. Grazing collisions generally lead to inelastic scattering and nucleon exchange reactions and are termed quasi-elastic reactions in Fig. 1.3 and the corresponding maximum possible angular momentum as ℓ_{max}. DIS results from the contact collisions and is related to an intermediate value of angular momentum equivalent, ℓ_D. Being the most head-on collision (lowest value of impact parameter), CN-type reactions possess the lowest value for angular momentum transfer ℓ_{crit}. Momentum transfer for slightly more peripheral collisions leads to fusion-like or quasi-fission reactions and associated angular momentum as ℓ_f.

1.3 Nucleus-nucleus interaction in A ≈ 200 region

In heavy-ion collisions, two opposing forces came into action, the repulsive Coulomb interaction between the positively charged nuclei and the short-range attractive nuclear force. These two opposing forces constitute a barrier with a potential pocket. Another term contributing to the barrier height is the repulsive centrifugal force formed from the angular momentum of the heavy nuclei. The height of the barrier is known as fusion barrier height. The barrier is termed as one-dimensional barrier, as the nucleus-nucleus separation is the only degree of freedom (Refer Fig. 2.1 for the potential energy curves of the forces involved in the collision process). Depending on the energy they possess, the colliding ions may overcome or pass through this barrier. When the ions pass over or penetrate this barrier, it gets captured inside the potential pocket, and fusion is said to have occurred. At higher energies, with the increase in angular momentum, the centrifugal force increases, thereby reducing the depth of the potential trap. Beyond a specific value of angular momentum, called critical angular momentum, the energy pocket vanishes and the system, after capture, re-separates immediately before complete equilibration. With further angular momentum, non-compound nucleus processes and other inelastic processes begin to dominate.

1.3.1 Fusion at below and around the Coulomb barrier

Classically, the probability of the system to overcome the barrier is taken as one at energies above the Coulomb barrier and zero below the Coulomb barrier [16]. Therefore, classically there should be no fusion below the barrier energies. However, Sikora *et al.* [17] observed a considerable amount of fusion cross-sections in this classically forbidden region [17, 18]. This was explained through fusion via quantum mechanical tunneling [16]. The first experimental proof for quantum mechanical tunneling originates from α-decay [19, 20]. The quantum mechanical

tunneling successfully explained the experimental fusion cross-sections induced by a low-energy light projectile below and above the Coulomb barrier region by considering the radial motion being the only degree of freedom [16]. The model is known as the one-dimensional barrier penetration model (1D-BPM). However, for systems with heavy projectiles, the experimental fusion excitation function below the Coulomb barrier was found to overestimate the 1D-BPM by several orders of magnitude [21, 22].

The enhancement in experimental fusion cross-section with respect to the 1D-BPM demands a new form of potential, including more microscopical properties of the colliding systems and the relative motion of nuclei. Studies on below-barrier fusion cross-section associated this enhancement with the collective modes of the interacting nuclei [21]. The measured fusion cross-sections of many heavy-ion reactions were explained by including internal degrees of freedom and the relative motion of the colliding nuclei. Measurements for ^{16}O+^{144,150,152,154}Sm reactions showed a large variations in fusion enhancement with respect to 1D-BPM in sub-barrier fusion cross-sections with increasing neutron number [23, 24]. A similar kind of large variation in enhancement (with respect to 1D-BPM) with an increase in neutron number is also exhibited by the fusion cross-sections of ^{40}Ar+^{144,148,154}Sm reactions. The enhancement in below barrier fusion cross-sections of these sets of reactions was attributed to the difference in deformations of the target nuclei. Compared with the spherical ^{144}Sm nuclei, the Coulomb barrier changes when the projectile approaches a deformed nuclei [15]. Accordingly, fusion cross-sections in the below-barrier energy region also changes. Several studies verified the effects of the deformation of target and projectile on below-barrier fusion enhancement [25–28].

Experimental studies by Beckerman *et al.* [29–31] on the fusion cross-sections for the ^{58}Ni +^{58}Ni, ^{58}Ni + ^{64}Ni, and ^{64}Ni + ^{64}Ni reactions showed an additional below-barrier fusion enhancement in ^{58}Ni + ^{64}Ni fusion cross-section, even after including the inelastic excitations in the coupling. Among these systems, only ^{58}Ni + ^{64}Ni have a positive Q-value for transfer reaction. Positive Q-value for

neutron transfer indicate that no external energy is needed to transfer a neutron from one nucleus to other. The importance of neutron transfer with positive Q-values on nuclear fusion originates from the fact that neutrons are insensitive to the Coulomb barrier and therefore they can start being transferred at larger separations before the projectile is captured by target-nucleus. Therefore, it is generally thought that the sub-barrier fusion cross section will increase because of the neutron transfer. Further, for neutron transfer with positive Q-value, the kinetic energy of reaction system may increase, leading to fusion enhancement too. For the above reasons, the effect of positive Q-value neutron transfer (PQNT) on fusion, especially at sub-barrier energies, becomes an important topic of interest. Several studies on systems with PQNT channel showed a fusion enhancement in the below-barrier energy region [32–36]. Thus in the presence of couplings, the single fusion barrier was transformed into a distribution of barriers. The barrier energies and probabilities are characteristic of the couplings and can be correlated with the configurations of nuclei in contact. Stelson *et al.* [37] proposed a model, wherein the neutron transfer may start at distances far away from the barrier distance itself, which creates a neck between the colliding nuclei. This neck formation reduces the barrier and causes fusion enhancement. From the fusion cross-section, the barrier distribution can be obtained by twice differentiating the product of energy and fusion cross-section with respect to the energy [15].

1.3.2 Non-compound nuclear fission processes

If the intermediate composite system does not get enough time to equilibrate in mass and energy, it can not equilibrate in all degrees of freedom. Fast-fission or quasi-fission like non-compound nuclear fission processes begin to dominate in such cases. Such processes are common in systems with $Z_P Z_T > 1600$. This can be considered as a decay mechanism for very heavy composite systems. The potential pocket formed inside the barrier becomes shallow at higher energy and angular momentum. For heavy composite systems, mere passage inside

the fusion barrier is insufficient to ensure CN formation. A model for nuclear amalgamation suggested by Swiatecki *et al.* [11, 12] predicted a dramatic change in reaction mechanism for collisions with charge product $Z_pZ_t > 1600$. Below this threshold, passage inside the fusion barrier guarantees compound nucleus formation. Above this value, extra energy was needed to push the system to a more compact configuration. In the liquid drop model (LDM), potential energy surfaces describes the shapes of the nuclear configuration during CN formation and its decay by three variables. They are (a) the relative distance between the nuclei, (b) neck thickness and (c) mass-asymmetry. The saddle point is obtained on this potential energy surface by allowing all these three degrees of freedom to vary. This saddle point is called an un-conditional saddle point (or Bohr-Wheeler saddle point). However, the di-nuclear system (DNS) formed will have a definite mass asymmetry in reactions. Hence, the potential energy surface seen by the DNS at the time of projectile target contact can be calculated by freezing the mass asymmetry. The resulting saddle point is the conditional saddle point for that particular configuration. The maximum value of all conditional saddle point configurations is known as Businaro-Gallone (BG) point, and the corresponding mass-asymmetry is known as BG mass-asymmetry (α_{BG}). The corresponding barrier is the conditional (fixed mass asymmetry) fission saddle point. Those systems trapped inside the conditional saddle point and outside the fission barrier are expected to undergo quasi-fission like the NCNF process. The possibility of a system to trap inside the conditional saddle point mainly depends on the elongation of the nuclei undergoing collision and a higher charge product [15]. Depending on the configuration of the system, those systems trapped inside the conditional saddle point need an additional *extra-extra-push* energy to attain a more compact configuration [38]. The dissipative nature of nuclear interactions included in Swiatecki's model made it require extra energy to push the nuclear system to a more compact conditional saddle point configuration[11, 12].

Quasi-fission [11, 12] is a major obstacle in extending the limit of the periodic table of elements to super-heavy regions. There has been general agreement that

entrances channel mass asymmetry $\alpha = \frac{A_t - A_p}{A_t + Ap}$,($A_p$ and A_t are projectile and target masses, respectively), charge product of projectile and target ($Z_P Z_T$), mean fissility of the CN (χ_m), static deformation and relative orientation of the reaction partners are the factors affecting quasi-fission. Experimental signatures of quasi-fission include anomalous behavior of fission fragment, angular anisotropy, mass angle correlation, broadened fusion-fission mass distribution and reduction of ER cross-section. This qualitative understanding of quasi-fission evolved from many experiments using various probes.

QF-like NCNF processes are generally observed in $Z_P Z_T$ values around 1600. Several systems with $Z_P Z_T$ values around 700 showed the presence of QF even in a very asymmetric systems [39–47]. Studies on the ER excitation function measurements of ^{219,221}Ac compound nuclei reported the presence of quasi-fission (QF) in ^{16}O-induced reactions [40]. ^{216}Ra compound nucleus showed a marked suppression in ER formation for very asymmetric combinations of colliding nuclei [41–43]. Corradi *et al.* [46, 47] observed fusion suppression effect in very asymmetric reactions leading to a pre-actinide nucleus ^{213}Fr. Signatures of QF is also observed in reactions forming less fissile ^{210}Rn [39, 44], ^{202}Po [45] and ^{202}Pb [48] nuclei with close mass asymmetry in the reaction entrance channel. All the reactions mentioned above have $Z_P Z_T$ around 700. All of them belong to a compound nuclei with mass number in A$\approx$ 200 regions. This means that apart from the dominant fusion mechanisms, QF is observed in systems with smaller charge products also. Studies in systems with compound nuclei mass A $\approx$ 200 regions will help us to explore more factors affecting fusion hindrance. Thus a comprehensive idea on factors affecting QF will make the super heavy element production more easier.

1.4 Present study

The competing reaction mechanisms in the A $\approx$ 200 areas are the focus of the current study. We measured the cross-sections of heavy-ion fusion at an en-

ergy close to and near the Coulomb barriers. Two studies are included in this thesis to investigate the reaction mechanism in $\approx$ 200 regions. Through our measurements, we address the entrance channel behavior of the fusion process at near-barrier energies and other competing reaction mechanisms which hinder fusion. It also includes a detailed investigation of the role of the positive-neutron transfer Q-value and the quadruple deformation parameter of colliding partners on the below-barrier fusion enhancement. For these purposes, the following reactions and methods are taken into consideration.

Evaporation residue measurements of ^{16,18}O+^{181}Ta

Evaporation residues are the valid signatures of CN formation. They are very sensitive probes to study the fusion phenomenon. Any inhibition in the complete fusion process will lead to suppression in ER cross-sections. Based on mass asymmetry α, and its critical value at Businaro-Gallone point (α_{BG}), one expects QF in ^{18}O+^{181}Ta ($\alpha < \alpha_{BG}$) reaction as compared to ^{16}O+^{181}Ta ($\alpha > \alpha_{BG}$). Considering two reactions, where the presence and absence of quasi-fission were expected are taken and compared with nearby systems. Statistical model analysis are done on the system which form the same compound nuclei to find the starting point of quasi-fission.

Evaporation residue measurements of ^{18}O+^{182,184,186}W

Fusion dynamics are affected by the nuclear structure and neutron transfer channels of the colliding nuclei [22]. Existing theoretical models have already established the role of nuclear deformation and vibration through the coupling of inelastic excitations in theoretical models [49]. However, a comprehensive understanding of the role of neutron transfer channels in fusion enhancement remains incomplete. It was identified that reactions with positive Q-values transfer channel (PQNT) channels play a vital role in sub-barrier fusion cross-section enhancement [50]. However, many systems with positive Q-value neutron transfer (PQNT) channels do not exhibit a below-barrier fusion enhancement. Hence, more investigations are needed to find the role of the positive Q-value of neutron transfer in fusion enhancement below the Coulomb barrier energy region.

In order to study the effect of positive transfer Q-value on fusion enhancement, we have performed the ER measurements of ^{18}O+^{182,184,186}W reactions, which have positive 2n-transfers Q-values. One of the main objectives of this work is to compare the ER cross-section with nearby systems, ^{16}O+^{182,184,186}W [51, 52], which have negative Q-values for 2n-transfer.

1.5 Outline of the thesis

This thesis is organized as follows. After a general introduction to heavy-ion reactions, a detailed description on the classification of heavy-ion reactions is given in Chapter 1. Chapter 2 deals with the theoretical models used to analyze the experimental cross-sections of the present study. Chapter 3 covers the experimental set-up used for conducting the experiments. It includes a brief description of the mass spectrometer, solid-state detectors, electronics set-up, and data acquisition. Two sets of heavy-ion reactions to study the competing mechanisms in the A $\approx$ 200 region are reported in Chapters 4 and 5. These chapters includes the description about the experimental set-up, the data-analysis performed, details of Coupled channel and statistical model calculations, comparison of these calculations with our experimental data and their possible implications. The assumption from the study of two sets of reaction are summarised in Chapter 6.

Bibliography

[1] M. Dasgupta, D. J. Hinde, N. Rowley, and A. M. Stefanini, Annu. Rev. Nucl. Part. Sci. **48**, 401 (1998).

[2] C. Ngo, H. Ngo, S. Leray, and M. Spina, Nucl. Phys. A **499**, 148 (1989).

[3] S. Kailas, Phys. Rep. **284**, 381 (1997).

[4] R. du Rietz, D. J. Hinde, M. Dasgupta, R. G. Thomas, L. R. Gasques, M. Evers, N. Lobanov, and A. Wakhle, Phys. Rev. Lett. **106**, 052701 (2011).

[5] Hinde, D. J., du Rietz, R, and Dasgupta, M., EPJ Web of Conferences **17**, 04001 (2011).

[6] J. H. Hamilton, S. Hofmann, and Y. T. Oganessian, Annu. Rev. Nucl. Part. Sci. **63**, 383 (2013).

[7] Y. T. Oganessian and V. K. Utyonkov, Rep. Prog. Phys. **78**, 036301 (2015).

[8] V. Weisskopf, Phys. Rev. C **52**, 295 (1937).

[9] N. Bohr and J. A. Wheeler, Phys. Rev. C **56**, 426 (1939).

[10] K. S. Krane, *Introductory Nuclear Physics* (Wiley India 2008).

[11] W. J. Swiatecki, Phys. Scr. **24**, 113 (1981).

[12] W. Swiatecki, Nucl. Phys. A **376**, 275 (1982).

[13] S. Bjrnholm and W. Swiatecki, Nucl. Phys. A **391**, 471 (1982).

[14] B. B. Back, R. R. Betts, J. E. Gindler, B. D. Wilkins, S. Saini, M. B. Tsang, C. K. Gelbke, W. G. Lynch, M. A. McMahan, and P. A. Baisden, Phys. Rev. C **32**, 195 (1985).

[15] M. Dasgupta, D. J. Hinde, N. Rowley, and A. M. Stefanini, Ann. Rev. Nucl. Part. Sci **48**, 401 (1998).

[16] D. Allan Bromley, *Treatise on Heavy-Ion Science*, volume 6 (Plenum Press, New York 1984).

[17] B. Sikora, J. Bisplinghoff, W. Scobel, M. Beckerman, and M. Blann, Phys. Rev. C **20**, 2219 (1979).

[18] L. C. Vaz, J. M. Alexander, and G. Satchler, Phys. Rep. **69**, 373 (1981).

[19] G. Gamow, Z. Phys **51**, 204 (1928).

[20] G. Gamow, Z. Phys **52**, 510 (1929).

[21] S. G. Steadman and M. J. Rhoades-Brown, Ann. Rev. Nucl. Part. Sci **36**, 649 (1986).

[22] M. Beckerman, Rep. Prog. Phys **51**, 1047 (1988).

[23] R. G. Stokstad, Y. Eisen, S. Kaplanis, D. Pelte, U. Smilansky, and I. Tserruya, Phys. Rev. Lett. **41**, 465 (1978).

[24] R. G. Stokstad, Y. Eisen, S. Kaplanis, D. Pelte, U. Smilansky, and I. Tserruya, Phys. Rev. C **21**, 2427 (1980).

[25] J. R. Leigh, M. Dasgupta, D. J. Hinde, J. C. Mein, C. R. Morton, R. C. Lemmon, J. P. Lestone, J. O. Newton, H. Timmers, J. X. Wei, and N. Rowley, Phys. Rev. C **52**, 3151 (1995).

[26] Montagnoli, Giovanna, Stefanini, and A. M., Eur. Phys. J A **53** (2017).

[27] B. B. Back, H. Esbensen, C. L. Jiang, and K. E. Rehm, Rev. Mod. Phys. **86**, 317 (2014).

[28] K. Hagino and N. Takigawa, Prog. Theor. Exp. Phys. **128**, 1061 (2012).

[29] M. Beckerman, M. Salomaa, A. Sperduto, H. Enge, J. Ball, A. DiRienzo, S. Gazes, Y. Chen, J. D. Molitoris, and M. Nai-feng, Phys. Rev. Lett. **45**, 1472 (1980).

[30] M. Beckerman, J. Ball, H. Enge, M. Salomaa, A. Sperduto, S. Gazes, A. DiRienzo, and J. D. Molitoris, Phys. Rev. C **23**, 1581 (1981).

[31] M. Beckerman, M. Salomaa, A. Sperduto, J. D. Molitoris, and A. DiRienzo, Phys. Rev. C **25**, 837 (1982).

[32] G. Montagnoli, S. Beghini, F. Scarlassara, A. Stefanini, L. Corradi, C. Lin, G. Pollarolo, and A. Winther, Eur. Phys. J A **15**, 351 (2002).

[33] M. Trotta, A. M. Stefanini, L. Corradi, A. Gadea, F. Scarlassara, S. Beghini, and G. Montagnoli, Phys. Rev. C **65**, 011601 (2001).

[34] R. Broglia, C. Dasso, S. Landowne, and G. Pollarolo, Phys. Lett. B **133**, 34 (1983).

[35] S. Kalkal, S. Mandal, N. Madhavan, E. Prasad, S. Verma, A. Jhingan, R. Sandal, S. Nath, J. Gehlot, B. R. Behera, M. Saxena, S. Goyal, D. Siwal, R. Garg, U. D. Pramanik, S. Kumar, T. Varughese, K. S. Golda, S. Muralithar, A. K. Sinha, and R. Singh, Phys. Rev. C **81**, 044610 (2010).

[36] H. Q. Zhang, C. J. Lin, F. Yang, H. M. Jia, X. X. Xu, Z. D. Wu, F. Jia, S. T. Zhang, Z. H. Liu, A. Richard, and C. Beck, Phys. Rev. C **82**, 054609 (2010).

[37] P. Stelson, Phys. Lett. B **205**, 190 (1988).

[38] W. Swiatecki, Physica Scripta **24**, 113 (1981).

[39] A. Shamlath, M. Shareef, E. Prasad, P. Sugathan, R. G. Thomas, A. Jhingan, S. Appannababu, A. K. Nasirov, A. M. Vinodkumar, K. M. Varier, C. Yadav, B. R. S. Babu, S. Nath, G. Mohanto, I. Mukul, D. Singh, and S. Kailas, Nucl. Phys. A **945**, 67 (2016).

[40] J. Gehlot, A. M. Vinodkumar, N. Madhavan, S. Nath, A. Jhingan, T. Varughese, T. Banerjee, A. Shamlath, P. V. Laveen, M. Shareef, P. Jisha, P. S. Devi, G. N. Jyothi, M. M. Hosamani, I. Mazumdar, V. I. Chepigin, M. L. Chelnokov, A. V. Yeremin, A. K. Sinha, and B. R. S. Babu, Phys. Rev. C **99**, 034615 (2019).

[41] D. J. Hinde, A. C. Berriman, D. B. R, M. Dasgupta, I. I. Gontchar, C. R. Morton, A. Mukherjee, and J. O. Newton, J. Nucl. Radiochem. Sci **3**, 31 (2002).

[42] R. N. Sagaidak, G. N. Kniajeva, I. M. Itkis, M. G. Itkis, N. A. Kondratiev, E. M. Kozulin, I. V. Pokrovsky, A. I. Svirikhin, V. M. Voskressensky, A. V. Yeremin, L. Corradi, A. Gadea, A. Latina, A. M. Stefanini, S. Szilner, M. Trotta, A. M. Vinodkumar, S. Beghini, G. Montagnoli, F. Scarlassara, D. Ackermann, F. Hanappe, N. Rowley, and L. Stuttg, Phys. Rev. C **68**, 014603 (2003).

[43] D. J. Hinde, M. Dasgupta, and A. Mukherjee, Phys. Rev. Lett. **89**, 282701 (2002).

[44] A. Shamlath, E. Prasad, N. Madhavan, P. V. Laveen, J. Gehlot, A. K. Nasirov, G. Giardina, G. Mandaglio, S. Nath, T. Banerjee, A. M. Vinodkumar, M. Shareef, A. Jhingan, T. Varughese, D. Kumar, P. S. Devi, Khushboo, P. Jisha, N. Kumar, M. M. Hosamani, and S. Kailas, Phys. Rev. C **95**, 034610 (2017).

[45] R. Rafiei, R. G. Thomas, D. J. Hinde, M. Dasgupta, C. R. Morton, L. R. Gasques, M. L. Brown, and M. D. Rodriguez, Phys. Rev. C **77**, 024606 (2008).

[46] L. Corradi, B. R. Behera, E. Fioretto, A. Gadea, A. Latina, A. M. Stefanini, S. Szilner, M. Trotta, Y. Wu, S. Beghini, G. Montagnoli, F. Scarlassara, R. N. Sagaidak, S. N. Atutov, B. Mai, G. Stancari, L. Tomassetti, E. Mariotti, A. Khanbekyan, and S. Veronesi, Phys. Rev. C **71**, 014609 (2005).

[47] R. N. Sagaidak, A. Y. Chizhov, I. M. Itkis, M. G. Itkis, G. N. Kniajeva, N. A. Kondratiev, E. M. Kozulin, I. V. Pokrovsky, L. Corradi, E. Fioretto, A. Gadea, A. Latina, A. M. Stefanini, S. Beghini, G. Montagnoli, F. Scarlassara, M. Trotta, and S. Szilner, AIP Conf. Proc. **853**, 114 (2006).

[48] G. N. Knyazheva, E. M. Kozulin, R. N. Sagaidak, A. Y. Chizhov, M. G. Itkis, N. A. Kondratiev, V. M. Voskressensky, A. M. Stefanini, B. R. Behera, L. Corradi, E. Fioretto, A. Gadea, A. Latina, S. Szilner, M. Trotta, S. Beghini, G. Montagnoli, F. Scarlassara, F. Haas, N. Rowley, P. R. S. Gomes, and A. S. d. Toledo, Phys. Rev. C **75**, 064602 (2007).

[49] K. Hagino, N. Rowley, and A. Kruppa, Comput. Phys. Commun. **123**, 143 (1999).

[50] V. V. Sargsyan, G. G. Adamian, N. V. Antonenko, W. Scheid, and H. Q. Zhang, Phys. Rev. C **84**, 064614 (2011).

[51] J. R. Leigh, J. J. M. Bokhorst, D. J. Hinde, and J. O. Newton, Journal of Physics G: Nuclear Physics **14**, L55 (1988).

[52] M. Trotta, A. M. Stefanini, L. Corradi, A. Gadea, F. Scarlassara, S. Beghini, and G. Montagnoli, Phys. Rev. C **65**, 011601 (2001).

Chapter 2

Theoretical models

The measurements in this thesis involve fusion reactions induced by low-energy medium-heavy projectiles on a heavy target, which forms CN in the A $\approx$ 200 regions. Different statistical and dynamical models are required for predicting as well as interpreting the experimental results. In this thesis, for theoretical interpretation of the experimental fusion cross-section microscopic model codes like HIVAP [1, 2] and macroscopic model codes like CCFULL [3–5] were used. Also, for efficiency calculations we make use of codes like TERS and [6, 7], PACE [8] in our thesis. The theoretical aspects of the various models and codes utilized in the present work are described in this chapter.

2.1 Compound nucleus formation

The heavy-ion fusion is the process of combining two nuclei into a single fully equilibrated compound nucleus. When a heavy-ion interacts with another heavy-ion, both the nuclei experience mutual Coulomb (V_{Coul}), nuclear (V_{nucl}) and centrifugal (V_{cent}) interactions, resulting in the formation of the fusion barrier. According to classical theory, for heavy-ion fusion to occur, the projectile's energy must be sufficient to surpass the fusion barrier.

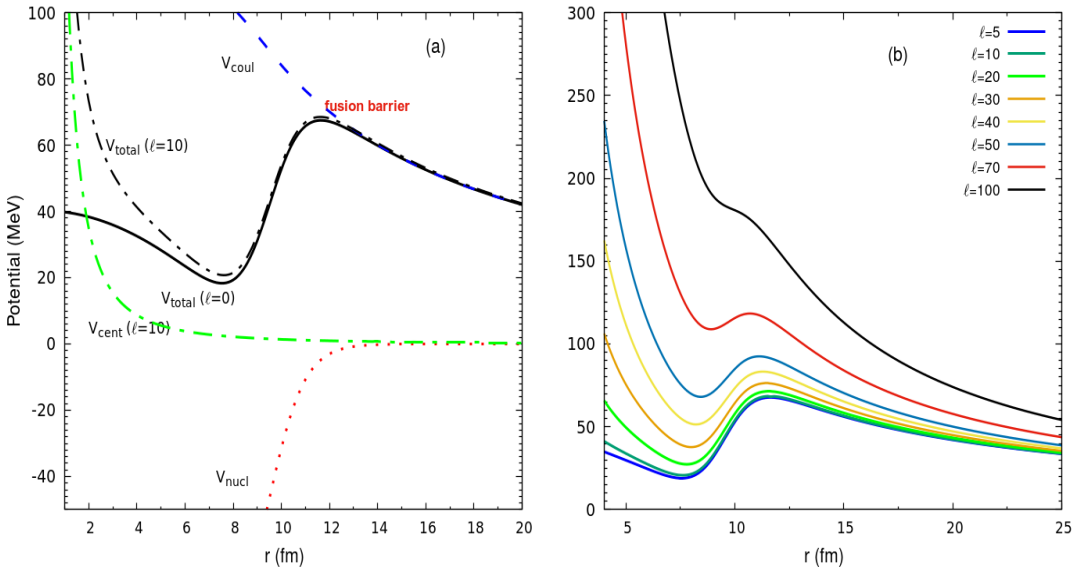

Figure 2.1: Curves in the panel (a) shows the dependence of Coulomb, nuclear, centrifugal and total potential energy on relative distances between the nuclei. Curves in the panel (b) shows the change in the potential energy curve with an increase in angular momentum. Above graphs are for the reaction ^{18}O+^{181}Ta.

Total potential ($V(r)$) experienced by the projectiles and target while approaching each other is given by

$$V(r) = V_{Coul}(r) + V_{nucl}(r) + V_{cent}(r) \tag{2.1}$$

The Coulomb potential is calculated assuming the nucleus to be point charges and the distance r as the distance between the centers of nuclei. V_{Coul} is inversely proportional to distance, showing a smooth variation with distance. The smooth variation of V_{Coul} with internuclear separation r is shown as dashed lies in Fig. 2.1(a). For a given projectile-target combination, the Coulomb potential energy is given by

$$V_{Coul}(r) = \begin{cases} \frac{Z_P Z_T e^2}{2R_c}(3 - \frac{r^2}{R_c^2}) & \text{for } r \leq R_c \\ \frac{Z_P Z_T e^2}{r} & \text{for } r > R_c \end{cases} \tag{2.2}$$

Z_P and Z_T are projectile and target atomic numbers, respectively. The nuclei are expected to be a uniformly charged sphere of radius, R_c , and it is defined as

$$R_c = r_0(A_P^{1/3} + A_T^{1/3}),\ r_0 = 1.2\, fm \tag{2.3}$$

where A_P and A_T respectively are the mass numbers of the projectile and target. On the other hand, nuclear potential, $V_{nucl}(r)$ is effective at short distances (few fm) between the two nuclei and is represented by a Woods-Saxon form as

$$V_{nucl}(r) = \frac{-V_0}{1 + exp^{(\frac{r-r_0}{a})}} \tag{2.4}$$

where V_0 is the depth of the potential well, r_0 is the radius parameter and a is the diffuseness. The centrifugal part is given by

$$V_{cent}(r) = \frac{\hbar^2 \ell(\ell+1)}{2\mu r^2} \tag{2.5}$$

where ℓ is the relative angular momentum quantum number and μ is the reduced mass of the projectile-target system, which is given by μ=$\frac{A_P A_T}{A_P + A_T}$.

2.1.1 Fusion above the Coulomb barrier

The fusion between the two nuclei occurs when the projectile overcomes the Coulomb barrier and enters the potential well, shown in Fig. 2.1(a). For $\ell = 0$, the peak value of the potential is called the Coulomb barrier. The respective values of V and r are called the barrier height (V_B) and barrier radius (R_B) of the fusion

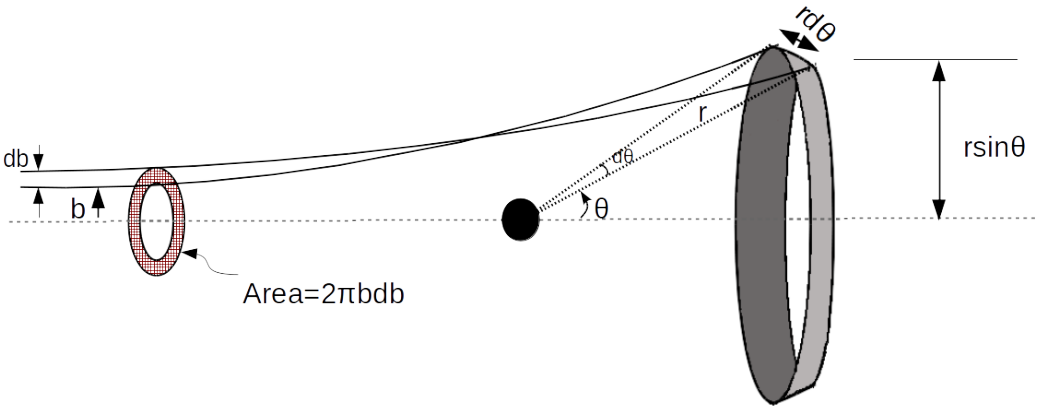

Figure 2.2: Schematic diagram for determining the classical cross-section of trajectories.

barrier. When the angular momentum increases, the potential becomes shallower and gradually disappears. Hence, the angular momentum effect reduces the size of the energy pocket by setting an upper angular momentum limit (ℓ_{crit})for forming a CN. The shape of the potential with increasing angular momentum is shown in Fig. 2.1(b). Thus classically, the projectile may either fuse to the target or scatter by it, depending on its energy. In the presence of these nuclear and Coulomb fields, the projectile with energy E and impact parameter b will experience an effective potential $V_b(r)$

$$V_b(r) = V(r) + E\frac{b^2}{r^2} \tag{2.6}$$

When the impact parameter become the grazing impact parameter (b_{gr}) colliding partners start feeling the nuclear interaction. b_{gr} is slightly higher than the distance between the centers of the projectile and the target. The radial distance

at that point is known as barrier radius (R_B) and the corresponding effective potential is known as barrier potential (V_B). At impact parameter, $b > b_{gr}$, the projectile will be scattered by the potential, and at $b < b_{gr}$ projectile fuses with the target. In this case, Eq. 2.6 can be rewritten as

$$E = V_B + E\frac{b_{gr}^2}{R_B^2} \tag{2.7}$$

After rearranging the Eq. 2.7, we get

$$b_{gr} = R_B\sqrt{\left(1 - \frac{V_B}{E}\right)} \tag{2.8}$$

The trajectories entering through area $2\pi bdb$ will fuse if $b < b_{gr}$ (as shown in Fig. 2.2). Thus the fusion cross-section will be equal to $2\pi bdb$ where db varies from 0 to b_{gr}.

$$\sigma_{fus} = \pi b_{gr}^2 \tag{2.9}$$

Substituting Eq. 2.8, in Eq. 2.9, we obtain the fusion cross-section as

$$\sigma_{fus}(E) = \pi R_B^2\left(1 - \frac{V_B}{E}\right) \tag{2.10}$$

Classically orbital angular momentum ℓ can be expressed as

$$\ell = r \times p = bp \tag{2.11}$$

But, $p = \sqrt{2mE}$, substituting this value of p in above equation

$$\ell = b\sqrt{2mE} \tag{2.12}$$

Quantum mechanically orbital angular momentum can be expressed as $L = \hbar\ell$. On equating the value of ℓ, we get

$$\hbar\ell = b\sqrt{2mE} \tag{2.13}$$

$$\ell = b\frac{\sqrt{2mE}}{\hbar} = bk \tag{2.14}$$

where k is the wave number. Then grazing angular momentum ℓ_{gr} can be expressed as

$$\ell_{gr} = b_{gr}k \tag{2.15}$$

All partial waves with $\ell < \ell_{gr}$ will undergo fusion and that with $\ell > \ell_{gr}$ will be scattered by the potential.

The transmission coefficient can be written as

$$T(\ell) = \begin{cases} 1 & \text{if } \ell < \ell_{gr} \\ 0 & \text{if } \ell > \ell_{gr} \end{cases} \tag{2.16}$$

$T(\ell)$ can be expressed in terms of the action integral S-function in elastic scattering as

$$T(\ell) = 1 - |S_\ell|^2 \tag{2.17}$$

where S_ℓ is the S-function in elastic scattering, which is defined as

$$S_\ell = \sqrt{\frac{2\mu}{\hbar^2}} \int_{r1\ell}^{r2\ell} \sqrt{(V_l(r) - E)}dr \tag{2.18}$$

S-function related to the reflection co-efficient η_ℓ by the relation, $\eta_\ell = |S_\ell|^2$

At particular energy, the partial fusion cross-section is given by

$$\sigma_\ell = \frac{\pi\hbar^2}{2\mu E}(2\ell+1)T_\ell(E) \tag{2.19}$$

In quantum mechanics, the total cross-section is obtained by summing the contributions from all the partial cross-sections.

$$\sigma = \frac{\pi\hbar^2}{2\mu E}\sum_{\ell=0}^{\infty}(2\ell+1)T_\ell(E) \tag{2.20}$$

To obtain total fusion cross-section quantum mechanically, we have to limit the angular momentum to a limiting value that is ℓ_{gr},

$$\sigma_{fus} = \frac{\pi\hbar^2}{2\mu E}\sum_{\ell=0}^{\ell_{gr}}(2\ell+1)T_\ell(E) \tag{2.21}$$

After applying the value of transmission coefficient $T_\ell(E)$ in this equation, we obtain the total fusion cross-section as

$$\sigma_{fus} = \frac{\pi\hbar^2}{2\mu E}\ell_{gr}(1+\ell_{gr}) \tag{2.22}$$

in the classical limit for $\ell_{gr} >> 1$ Eq. 2.22 become

$$\sigma_{fus} = \frac{\pi\hbar^2}{2\mu E}l_{gr}^2 = \frac{\pi}{k^2}l_{gr}^2 = \pi b_{gr} \tag{2.23}$$

when, the $b < b_{gr}$ does not ensure fusion, and CN's stability is influenced by its angular momentum. If the angular momentum involved is much higher than the critical value of angular momentum ℓ_{crit}, it results in fission. That is $b < b_{gr}$ ($\ell < \ell_{gr}$) a necessary but not a sufficient condition for fusion to occur. Thus, a necessary condition for the impact parameter for fusion is that the impact parameter is smaller than the critical value of the impact parameter (b_{crit}). It

relates with the critical value of angular momentum (ℓ_{crit}) by the equation $b_{crit} = l_{crit}/k$. Thus for impact parameter values $b_{gr} < b_{crit}$ fusion is ensured by b_{gr} value, whereas for $b_{gr} > b_{crit}$ fusion is ensured by b_{crit} value. Thus fusion cross-section based on impact parameter can be represented as

$$\sigma_{fus} = \begin{cases} \pi b_{gr}^2 & \text{if } b_{gr} < b_{crit} \\ \pi b_{crit}^2 & \text{if } b_{gr} > b_{crit} \end{cases} \tag{2.24}$$

Here,

$$b_{crit}^2 = \frac{\ell_{crit}^2}{k^2} = \frac{\ell_{crit}^2 \hbar^2}{2\mu E} \tag{2.25}$$

The density overlap of the interacting nuclei is another factor that influences fusion, in addition to the impact parameter and angular momentum. Therefore, if adequate density overlap is not ensured, the collision does not guarantee the CN formation, even if the impact parameter is less than the cut-off limit. As a result, if the relative distance between the interacting nuclei is smaller than a critical distance, then only the interaction will lead to fusion.

2.1.2 Fusion below the Coulomb barrier - One dimensional barrier penetration model

Classically, fusion in below-barrier energies is forbidden, that is, $T_\ell = 0$. However, considerable amount of fusion cross-section were observed in below-barrier energies [9, 10]. It was explained by invoking the concept of quantum mechanical tunnelling [11, 12]. At below-barrier energies, quantum effects play a major role in explaining the fusion cross-section. Solving the radial equation fusion cross-section in below-barrier energies can be obtained.

For the motion of a particle of mass μ in a spherically symmetric potential

$V(r)$, the radial part of the time-independent Schrödinger equation in spherical polar coordinates can be written as,

$$\frac{\hbar^2}{2\mu}\Big[\frac{1}{r^2}\frac{d}{dr}(r^2\frac{d}{dr})\Big]\phi(r) + \Big[E - V(r) - \frac{\ell(\ell+1)\hbar^2}{2\mu r^2}\Big]\phi(r) = 0 \tag{2.26}$$

On re-arranging the Eq. 2.26

$$\frac{1}{r^2}\frac{d}{dr}(r^2\frac{d}{dr})\phi(r) + \frac{\hbar^2}{2\mu}[E - V_\ell(r)]\phi(r) = 0 \tag{2.27}$$

Where $V_\ell(r)$ nucleon-nucleon interaction potential obtained from Eq. 2.1 for angular momentum ℓ, which is given by

$$V_\ell(r) = V(r) + \frac{\ell(\ell+1)\hbar^2}{2\mu r^2} \tag{2.28}$$

The radial Schrödinger equation can be obtained by substituting $\phi = \psi/r$ and wave-number $k_\ell^2(r) = \frac{\hbar^2}{2\mu}[E - V_\ell(r)]$ in Eq. 2.28 it become

$$\frac{d^2\psi_\ell(r)}{dr^2} + k_\ell^2\psi_\ell(r) = 0 \tag{2.29}$$

The total fusion cross-section is obtained by summing over all partial waves below ℓ_{crit}. The potential is considered to be slightly parabolic near the barrier to calculate the fusion cross-section [11–14].

$$\sigma_{fus} = \frac{\pi\hbar^2}{2\mu E}(2\ell+1)T_\ell \tag{2.30}$$

Hill-Wheeler expression of the transmission coefficient T_ℓ [14] can be expressed as

$$T_\ell = (1 + \exp[\frac{2\pi}{\hbar\omega_\ell}(V_\ell - E)])^{-1} \tag{2.31}$$

V_ℓ represents the barrier height in MeV for the ℓ^{th} partial wave, ω_ℓ the vibrational frequency of the harmonic oscillator in the parabolic potential and $\hbar\omega_\ell$ defines the corresponding barrier curvature. We obtain the fusion cross-section by substituting the new transmission coefficient value in Eq. 2.20.

$$\sigma_{fus}(E) = \frac{R_B^2 \hbar\omega_0}{2E} ln\Big[1 + \exp\Big(\frac{2\pi}{\hbar\omega_0}(E - V_B)\Big)\Big] \tag{2.32}$$

which is the 1D-BPM equation. Where R_B, V_B, and $\hbar\omega_0$ are the barrier radius, height and curvature at ℓ=0, respectively. Expression for fusion cross-section for above and below-barrier energies are shown below

$$\sigma_{fus} = \begin{cases} \pi R_B^2(1 - V_B/E) & \text{if } E >> V_B \\ \frac{R_B^2\hbar\omega_0}{2E} exp\Big[\frac{2\pi}{\hbar\omega_0}(E - V_B)\Big] & \text{if } E << V_B \end{cases} \tag{2.33}$$

In the above model, fusion cross-section depends only on a single parameter, that is, the radial separation r, hence the above model is termed as 1D-BPM. 1D-BPM satisfactorily explained the fusion cross-sections of light mass nuclei[15]. However, measured heavy-ions fusion cross-sections were enhanced compared with 1D-BPM in the sub-barrier energy region [16, 17]. The interpretation using inert, spherical nuclei reacting through a one-dimensional potential was inadequate to explain heavy-ion fusion cross-sections. This led to a study on other internal degrees of freedom, such as static deformation, inelastic and transfer coupling, all of which play a significant role in the fusion reactions at near barrier energies [17]. Thus 1D-BPM is improved by adding the channel couplings effects to explain the observed experimental fusion cross-sections. Also, at near barrier energies, the angular momentum associated with heavy-ion fusion reactions was reported to extend to very high values over 1D-BPM predictions.

In 1-DBPM, the incoming nuclei face a single barrier of a certain height, the tunneling that provides a corresponding fusion cross-section. However, it was established that coupling with internal degrees of freedom, such as static deformation, vibrational states of colliding nuclei, neutron transfer, neck formation, etc., increases fusion cross-section in sub-barrier energies. Consider two colliding nuclei, among which the target is deformed. In that case, the barrier height will depend on the orientation of the colliding nuclei. Suppose the nuclei approach through the symmetry axis of prolate nuclei. In that case, the height of the fusion barrier decreases, and the fusion cross-section increases; along with the perpendicular direction, fusion barrier increases and the cross-section decreases.

Similarly, coupling with other degrees of freedom will change the barrier height and, in turn, changes the fusion cross-sections. Thus coupling with various internal degrees of freedom will lead to a distribution of barriers. This spread in the barrier can explain the enhancement in fusion excitation function in the sub-barrier region. Coupled channel calculation successfully incorporated all the internal degrees of freedom and the relative motion of the colliding nuclei [18–20].

2.2 Coupled Channel model

In coupled channel (CC)model, the relative motion of the colliding nuclei is coupled to the internal degrees of freedom of the many-body system. The total wave function can be expanded in terms of the channel states. The effects of internal degrees of freedom on sub-barrier fusion can be studied by solving the coupled channel equation [3, 4]. For this, a radial Schrödinger equation was formed.

$$\Big[-\frac{\hbar^2}{2\mu}\frac{d^2}{dr^2}+\frac{J(J+1)\hbar^2}{2\mu r^2}+V_N^{(0)}(r)+\frac{Z_P Z_T e^2}{r}+\epsilon_n-E\Big]\psi_n(r)+\sum_m V_{nm}(r)\psi_m(r)=0 \tag{2.34}$$

Where r radial component of the coordinate of the relative motion, $V_N^{(0)}$ nuclear potential in the Woods-Saxon parametrization, ϵ_n excitation energy of the nth channel, E incident energy in the center of the mass frame, and V_{nm} matrix elements of the coupling Hamiltonian. Here $V_N^{(0)}$ the nuclear potential can be represented as

$$V_N^{(0)} = \frac{-V_0}{1 + exp(\frac{r-R_0}{a})} \tag{2.35}$$

By imposing the boundary conditions of incoming and outgoing waves [21, 22] in coupled Hamiltonian, Dasso *et al.* [19, 23] solved the coupled channel equations. While solving the coupled channel equations, it was assumed that the couplings to the ground state are similar for each channel, and the cross channel couplings were neglected. Solution of coupled channel equation can be written as the linear combinations of channel states ψ_m.

$$\psi_m = \sum_n T_n \psi_{nm} \tag{2.36}$$

Solutions of coupled channel equation shows that, the coupling of intrinsic degrees of freedom with the relative motions of the colliding nuclei splits the potential into many barriers. The total transmission is the sum of the transmission coefficients of each barrier. The increased transmission through lower barriers leads to the enhancement of cross-section at sub-barrier energies. However, the effect of channel coupling is not very significant at energies well above the Coulomb barrier.

2.2.1 CCFULL- A coupled channel code

All these aspects of coupled channel models explained above are incorporated in the coupled channel code CCFULL [3, 4]. It is a FORTRAN-77 code that

calculates the fusion cross-section and mean angular momentum of the CN in a heavy-ion collision. The CCFULL code have the option to incorporate the vibrational, rotational and transfer degrees of freedom along with the relative motion of the colliding nuclei while calculating the fusion cross-sections. In CCFULL, the effect of internal degrees of freedom is incorporated through a coupling matrix $\hat{O}$. The coupling will make changes in the radial vector R_0 as follows

$$R_0 \longrightarrow R_0 + \hat{O} \tag{2.37}$$

The coupling matrix element for different coupling in CCFULL is discussed below.

2.2.2 Vibrational Coupling

Matrix formalism offers a reliable and straightforward method for determining the coupling matrix elements [17]. The nuclear coupling Hamiltonian operator $\hat{O}$ for vibrational coupling is given by

$$\hat{O} = \frac{\beta_\lambda}{\sqrt{4\pi}} R_T (a^\dagger_{\lambda 0} + a_{\lambda 0}) \tag{2.38}$$

Here $a^\dagger_{\lambda 0}$ and $a_{\lambda 0}$ are the creation and annihilation operators and λ is the multiplicity of the vibrational mode. Matrix element corresponding to the Hamiltonian operator is given by

$$\hat{O}_{mn} = \frac{\beta_\lambda}{\sqrt{4\pi}} R_T (\sqrt{n}\delta_{m,n-1} + \sqrt{m}\delta_{m,n+1}) \tag{2.39}$$

Here $\hat{O}_{mn}$ is the element in m^{th} raw and n^{th} column of the Hamiltonian operator. β_λ is the deformation corresponding to a particular mode of vibration. R_T represents the radius of the target nuclei. If we are considering the vibrational

state of the projectile nuclei for coupling, correspondingly, R_T will be replaced by R_P (projectile radius).

Rotational Coupling

In rotational coupling, the target or projectile orientations are incorporated in the coupling Hamiltonian. The rotational coupling can be incorporated into the Hamiltonian through a dynamical operator. Change in the radius in the nuclear potential by the dynamical operator is given below

$$R_0 \longrightarrow R_0 + \hat{O} = R_0 + \beta_2 R_T Y_{20} + \beta_4 R_T Y_{40} \tag{2.40}$$

here β_2, β_4 are the quadrupole, hexadecapole deformation parameters of the target and $R_T = r_{coup} A_T^{1/3}$. Thus, the potential in the nuclear Hamiltonian is given by,

$$V_N(r, \hat{O}) = \frac{V_0}{1 + exp(\frac{r - R_0 - \hat{O}}{a})} \tag{2.41}$$

The same method can be applied to deformed projectiles also. Then the term R_T in the above equation will be replaced by R_P

Transfer Coupling

Transfer coupling can be incorporated into coupling Hamiltonian through a microscopic transfer coupling form factor. Microscopic coupling form factor corresponding to the transfer coupling is given by,

$$F_{trans}(r) = F_t \frac{dV_n^{(0)}}{dr} \tag{2.42}$$

here F_t is the coupling strength and $V_n(0)$ is the nuclear interaction potential. CCFULL can couple one pair of transfer channels between the ground states of the colliding nuclei at a time [3]. For the microscopic transfer coupling form-factor estimation, in principle, the transfer cross-section and hence the transfer probability measurements are needed [24, 25]. Instead of computing the transfer couplings form factor on a micro-scale, the strength parameter in the form factor is modified. One presumption for this strategy is that the strength of a transfer reaction is concentrated in a single state with a distinct Q-value among the distribution of Q-value [3, 25]

2.3 Statistical models

In the fusion of lighter nuclei, a compound nuclei is formed when projectile overcome the Coulomb barrier. In heavy-ion fusion, hot rapidly rotating CN de-excite excess energy and angular momentum via evaporation of light particles like neutrons, protons, α-particle, and γ-rays or via fusion-fission. The CN divides into two fragments of almost identical size during fission. Evaporation of nucleons occurs concurrently with this process also. The method of evaporation and fission will continue until the excitation energy is less than the particle separation energy. After this, the decay process is taken up by γ-ray emission. If the energy and angular momentum possessed by the colliding nuclei are very high, then after capture the excited di-nucleus undergo non-compound nuclear process.

Statistical models (SM) can be used to model the decay of an equilibrated nucleus. The statistical model calculations were based on the assumption that all of the decay channels are equally likely. Even though the number of nucleons is finite for a nucleus, their numerous possible configurations and decay modes make it statistically promising one, even at the lowest excitation energies.

The capture cross-section (σ_{cap}) for the formation of CN for highly asymmet-

ric light systems can be obtained by measuring fusion evaporation cross section (σ_{ER}) and fusion-fission cross sections (σ_{FF}). In the case of heavy compound nucleus formation, other contributions like quasi-fission cross-section (σ_{QF}), fast-fission cross-sections ($\sigma_{fast-fiss}$), etc. have to incorporate in total capture cross-section.

$$\sigma_{cap} = \sigma_{ER} + \sigma_{FF} + \sigma_{QF} + \sigma_{fast-fiss} \tag{2.43}$$

For asymmetric systems, $\sigma_{fus} = \sigma_{ER} + \sigma_{FF}$

$$\sigma_{cap} = \sigma_{fusion} + \sigma_{QF} + \sigma_{fast-fiss} \tag{2.44}$$

According to the CN hypothesis, the di-nuclear system travels a lengthy dynamical pathway and re-separating into fragments before equilibrating in all degrees of freedom. The corresponding fission is termed as non-compound nuclear fission process. The CN which de-excites via particle evaporation or γ-ray emission and survives fission, ends up as various evaporation residues (ER). Formation of these ERs depends on the capture probability (σ_{cap}), CN formation probability (P_{CN}) and its survival probability against fission (W_{surv}). ER cross-section is given as

$$\sigma_{ER} = \sigma_{cap} P_{CN} W_{surv} \tag{2.45}$$

While explaining the ER excitation function, any reduction in ER cross-section from the standard statistical model predictions is generally attributed to the presence of NCNF. Studying these effects is important, since it is a factor affecting the survival of the super heavy elements. Any value of $P_{CN} < 1$ can be considered as the presence of NCNF processes. For very asymmetric combinations of reaction partners, P_{CN} is taken as one. P_{CN} started to deviate from

unity for systems with high value of symmetry.

The inputs of the statistical model code, crucial in further discussions in the thesis are described in the following subsections.

2.3.1 Fission barrier

In statistical model computations, the fission barrier is an essential parameter. The reaction dynamics are greatly influenced by the height and width of this barrier. In fusion processes, especially those involving heavier projectile-target combinations, overcoming the Coulomb barrier isn't enough to produce a CN; the system also has to overcome the fission barrier after capture.

In the liquid drop model (LDM) [26], the nucleus is assumed to be a uniformly charged incompressible liquid drop. The nucleus possesses surface energy (E_s^0) equivalent to the surface tension of the liquid. Opposing forces like surface tension and Coulomb repulsion (E_c^0) of the liquid drop together form the fission barrier. Extensive work has been carried out [26, 27] using LDM to find the saddle point shape and energies. The most widely used expression for fission barrier height using the LDM model is

$$B_f = \begin{cases} 0.38(0.75 - \chi) \ for \ 1/3 < \chi < 2/3 \\ 0.83(1 - \chi)^3 \ for \ 2/3 < \chi < 1 \end{cases} \tag{2.46}$$

here χ is the fissility parameter given by $\chi = \frac{E_c^0}{2E_s^0}$

In LDM, the angular momentum of the nucleus is not considered, in-order to incorporate the effect of angular momentum in the fission barrier, Cohen *et al.* [27] introduced the Rotating Liquid Drop Model (RLDM). The RLDM estimates symmetric fission barrier heights as a function of angular momentum. In addition to surface and Coulomb forces, RLDM incorporates centrifugal force,

which favors nucleus break-up due to its significant moment of inertia. RLDM introduces a method to estimates fission barrier heights. Though it overestimates the fission barrier in A≈200 mass region. To overcome the drawbacks in LDM and RLDM, Sierk *et al.* [28] introduced a microscopic model of rotating nuclei, which is known as a rotating finite range model (RFRM). In RFRM, the surface energy was replaced by Yukawa-plus-exponential nuclear energy. This model explained the experimental fission barrier most satisfactorily for nuclei in A ≈ 200 mass region [28].

In SM calculations, by including the shell correction in the liquid-drop nuclear mass, the fission barrier $B_f(\ell)$ was estimated using the equation given below

$$B_f(\ell) = k_f B_f^{LD}(\ell) + \delta W_{gs} \tag{2.47}$$

Here δW_{gs} is the shell correction term, B_f^{LD} liquid drop model fission barrier and k_f fission barrier scaling factor. Shell correction is obtained by the difference between the experimental and the LDM masses (M_{expt} -M_{LDM}). The LDM fission barrier was obtained from the FRLDM potential [29], and the ground-state shell corrections were taken from the work of Myers *et al.* [30].

2.3.2 HIVAP - Statistical model code

Reisdorf developed a statistical model code HIVAP [1], to model the cross-section measured in the formation of super-heavy elements. Reisdorf *et al.* [2] improved HIVAP by the incorporation of fission into the de-excitation step as well as by the new insights into level density calculations, interaction barriers, ground-state masses, shell-effects, and fission barriers. The HIVAP code is a modular code that can be used in a multitude of situations. Because of this, a detailed list of the parameters used must be kept to distinguish the results of one parameter set from another. For a specific section of the Chart of Nuclide a particular set

of parameters were used in the HIVAP code, this make cross-section predictions of corresponding region more accurate. The standard set of parameters used in this description of the HIVAP code is referred to as the Reisdorf and Schadel parameters[1]. Among the various input parameters to the HIVAP code, the cross-section calculations are most sensitive to the choice of the fission barrier B_f and a_f/a_n, the ratio of the level density parameters at the saddle point.

An overview of the calculations in the HIVAP code used in this thesis is as follows. The input parameters for HIVAP were set same as Reisdorf and Schȧdel parameters [1, 2]. Compound nucleus formation is considered as separate from the de-excitation step. Fusion occurs when the projectile-target system passes the interaction barrier, which is calculated using the Bass interaction potential [31]. Below the barrier, a WKB (Wentzel-Kramer-Brillouin) approximation is made to estimate barrier penetration. The fusion barrier in HIVAP is allowed to fluctuate using a Gaussian function with a user-defined standard deviation. For systems with charges product $Z_P Z_T$ <1600 the fusion barriers calculated using HIVAP is compatible with experimental fusion barrier within 1 % [32].The de-excitation of the excited compound nuclei is calculated using the following sources: liquid drop masses, level density calculations [1], level density ratios [33], and fission barriers [27]. Invaluable source of information regarding the description of the calculation loop and the various parameters and their associated meanings are available in the Refs. [1, 2]. The standard set of parameters used in this thesis referred to as the Reisdorf and Schȧdel parameters and are given in Table 2.3.2.

2.3.3 PACE4

The PACE-4 is a statistical model evaporation code that stands for Projection Angular-momentum Coupled Evaporation (Version 4) [8]. The code is based on

Variable	Description	Reisdorf's parameters	Our parameters
LEVELPAR	Scale parameter for the level density	1.153	1.16
AF / AN	Level density ratio parameter value	1	1.1
BARFAC	Scale parameter for the fission barrier	1	varying
EDAMP	Shell effect damping energy (MeV)	18	18.5
DELT	Nuclear pairing correction energy (MeV)	11	0.
V0	Value of the nuclear potential (MeV)	70	75
R0	Nuclear radius parameter (fm)	1.12	1.1177
D	Fuzziness in the nuclear radius parameter (fm)	0.75	0.75
Q2	Nuclear quadrupole moment (fm 2)	1050	target dependent
CRED	Scale parameter for the interaction barrier	1	1.0
SIGR0	Fluctuation of the interaction barrier (% of R0)	3	0
CUTOFF	Integration limits in (SIGR0) for barrier fluctuations	5	2.5
XTH	Extra push theory threshold fissility parameter	0.7	0.720
APUSH	Slope coefficient from extra push theory	18	15.
FPUSH	Angular momentum coefficient from extra push theory	0.75	0.75

Table 2.1: Reisdorf and Schadel Parameter set and the parameter set used in this thesis for the HIVAP calculations

the statistical model and uses the Monte-Carlo simulation procedure for the de-excitation of compound nucleus. At various experimental beam energies, PACE4 can be used for examining the major decay channels of a reaction. All of the nuclei in the decay chain have their decay widths and probabilities calculated by the code until the residual nuclei stop decaying. The code may be used to determine the energy spectra and particle angular distributions. Fission cross sections calculated using the Bohr-Wheeler formalism is also provided by the code, along with the evaporation residue cross sections [34]. The code provides the total fusion cross sections only; the incomplete fusion process is not taken into account. The code computes the fusion cross-sections according to the Bass model [35].

Bibliography

[1] W. Reisdorf, Z. Phys. A. **300**, 227 (1981).

[2] W. Reisdorf and M. Schädel, Z. Phy. A. **343**, 47 (1992).

[3] K. Hagino, N. Rowley, and A. Kruppa, Comput. Phys. Commun. **123**, 143 (1999).

[4] K. Hagino and N. Takigawa, Prog. Theor. Phys. **128**, 1061 (2012).

[5] K. Hagino, N. Takigawa, M. Dasgupta, D. J. Hinde, and J. R. Leigh, Phys. Rev. Lett. **79**, 2014 (1997).

[6] S. Nath, Comput. Phys. Commun. **180**, 2392 (2009).

[7] S. Nath, Comput. Phys. Commun. **181**, 1659 (2010).

[8] A. Gavron, Phys. Rev. C **21**, 230 (1980).

[9] J. E. Bjorkholm, R. R. Freeman, A. Ashkin, and D. B. Pearson, Phys. Rev. Lett. **41**, 1361 (1978).

[10] B. Sikora, J. Bisplinghoff, W. Scobel, M. Beckerman, and M. Blann, Phys. Rev. C **20**, 2219 (1979).

[11] G. Gamow, Z. Phys **51**, 204 (1928).

[12] G. Gamow, Z. Phys **52**, 510 (1929).

[13] R. W. Gurney and E. U. Condon, Phys. Rev. **33**, 127 (1929).

[14] D. L. Hill and J. A. Wheeler, Phys. Rev. **89**, 1102 (1953).

[15] S. G. Steadman and M. J. Rhoades-Brown, Annual Review of Nuclear and Particle Science **36**, 649 (1986), https://doi.org/10.1146/annurev.ns.36.120186.003245.

[16] A. B. Balantekin and N. Takigawa, Rev. Mod. Phys. **70**, 77 (1998).

[17] M. Dasgupta, D. J. Hinde, N. Rowley, and A. M. Stefanini, Annual Review of Nuclear and Particle Science **48**, 401 (1998), https://doi.org/10.1146/annurev.nucl.48.1.401.

[18] C. Dasso, S. Landowne, and A. Winther, Nuclear Physics A **432**, 495 (1985).

[19] C. Dasso, S. Landowne, and A. Winther, Nuclear Physics A **405**, 381 (1983).

[20] R. Broglia, C. Dasso, S. Landowne, and G. Pollarolo, Physics Letters B **133**, 34 (1983).

[21] G. Rawitscher, Nuclear Physics **85**, 337 (1966).

[22] P. Bosetti, G. Grssler, G. Otter, H. Seyfert, H. Schreiber, K. Bckmann, J. Hofmann, J. Lowsky, H. Zobernig, V. Karimki, G. Kellner, D. Kocher, F. Triantis, K. Wernhard, T. Coghen, and P. Malecki, Nuclear Physics B **128**, 205 (1977).

[23] C. Dasso, S. Landowne, and A. Winther, Nuclear Physics A **407**, 221 (1983).

[24] S. Saha, Y. K. Agarwal, and C. V. K. Baba, Phys. Rev. C **49**, 2578 (1994).

[25] C. Dasso and G. Pollarolo, Physics Letters B **155**, 223 (1985).

[26] N. Bohr and J. A. Wheeler, Phys. Rev. **56**, 426 (1939).

[27] S. Cohen, F. Plasil, and W. Swiatecki, Annals of Physics **82**, 557 (1974).

[28] A. J. Sierk, Phys. Rev. C **33**, 2039 (1986).

[29] H. J. Krappe, J. R. Nix, and A. J. Sierk, Phys. Rev. C **20**, 992 (1979).

[30] W. Myers and W. Swiatecki, Ark. Fys. 36, 343 **36** (1966).

[31] R. Bass, Phys. Rev. Lett. **39**, 265 (1977).

[32] F. Phlhofer, Nuclear Physics A **280**, 267 (1977).

[33] J. Tke and W. wiatecki, Nuclear Physics A **372**, 141 (1981).

[34] N. Bohr and J. A. Wheeler, Phys. Rev. **56**, 426 (1939).

[35] R. Bass, Phys. Rev. Lett. **39**, 265 (1977).

Chapter 3

Experimental techniques

3.1 Introduction

This chapter provides the details of the experimental set-up, measurements, detectors and electronic set-up used in the present study. In the present study we measured the ER cross-sections of ^{16,18}O+^{181}Ta and ^{18}O+^{182,184,186}W reactions. The experiments were performed at the Inter University Accelerator Centre (IUAC), New Delhi, utilising a heavy ion beam provided by a 15 UD tandem accelerator and a heavy ion reaction analyzer (HIRA). The accelerator facility, different kinds of detectors used, electronics, and other experimental facilities used in the present study are briefly discussed in this chapter.

3.2 The Pelletron accelerator

The beams were provided from the 15 UD Pelletron facility at IUAC, New Delhi. The accelerated beams of ^{16}O and ^{18}O were used in the ER cross-section measurements of two separate experiments. The Pelletron is a tandem electrostatic accelerator [1, 2] that can accelerate ion beams of all stable nuclei (except noble gas). Multi cathode Cesium sputter negative-ion source serves as the ion

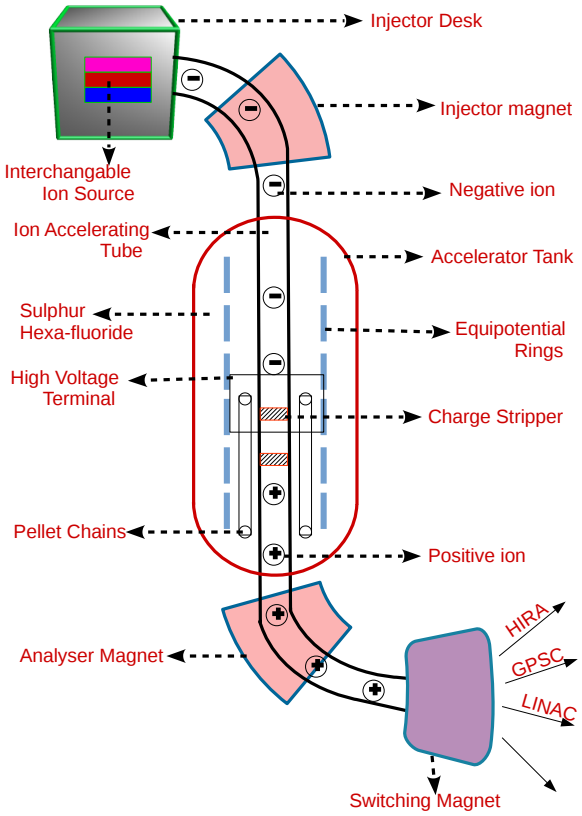

Figure 3.1: Schematic diagram of IUAC Pelletron accelerator.

source for the Pelletron. An injector magnet follows the ion source. The injector magnet bends the ions 90° in the downward direction and injects them into the accelerating tubes. The high voltage terminal is positioned in the center of the vertical accelerating tank. SF_6 insulating gas (with high dielectric constant) at a pressure of $\approx$ 6-7 atm is used to separate the accelerator from the tank. The high voltage terminal can be charged to a very high voltage ranging from 4 MV to 15 MV. A potential gradient is kept throughout the accelerating tube by putting 15 units of 1 MV on either side of the high voltage terminal. Low and high energy sections, respectively, refer to the locations before and after the terminal. Two dead sections (shorted units with no potential gradient that house the vacuum pumps and other beam handling components) are placed, one on either

side of the terminal. The schematic diagram of the Pelletron is shown in Fig. 3.1.

The injected ions are driven down to the high voltage terminal in the middle. The accelerated negative ions pass through a stripper at the terminal, which can be a thin carbon foil or a small volume of gas. Negatively charged ions lose electrons in the stripper and converted to positive charge. The mass and velocity of the ions being accelerated decides the charge state distribution of these ions. The positive terminal repels these positive ions, which then accelerate once more. Using a 90° bending dipole magnet known as the Analyzer magnet, ions with a specific charge state are chosen from this charge distribution according to their energy, mass, and charge state.

The amount of energy obtained by the ions after they exit the accelerator is determined by

$$E = E_0 + V(q + 1) \tag{3.1}$$

where E_0 denotes the energy received from the ion source deck potential in MeV, V the terminal potential in MV, and q the ion's charge state after stripping.
The high energy requirements of many experiments are met by further stripping in the high energy dead region. In the presence of a second stripper, the total energy available in MeV is

$$E = E_0 + V(1 + \frac{6}{15}q_1 + \frac{9}{15}q_2) \tag{3.2}$$

The ion charge states are q_1 and q_2 , respectively. An analyzer magnet of radius 1.8 m is used to bend ions with a specific mass, energy, and charge state 90 ∘ in the horizontal plane. The analyzer magnet's magnetic field B (in Gauss) is

proportional to the energy of the beam E in MeV as

$$B\rho = 0.144\sqrt{\frac{ME}{q^2}} \tag{3.3}$$

where M is the mass number of the ions in amu. The switching magnet deflects the high-energy ion beam into a different experimental facilities which are at 0 °, ± 15°, ± 30° and ± 45° angles for different experiments.

According to the experimental requirements, the IUAC pelletron accelerator produces both dc and pulsed beams at the target. The pulsing system is situated in the pre-acceleration phase, between the injector magnet and the tank top. The beam pulsing system includes (1) a chopper, (2) a buncher, and (3) a traveling wave deflector (TWD). The chopper cuts the dc beam into ion pulses, then compressed further by the buncher into even smaller pulses. The TWD's function is to alter the ion-beam's pulses repetition rate.

3.3 The recoil mass seperators

Recoil separators are devices used for beam rejection and mass analysis of the reaction products in nuclear reactions. They include electromagnetic components such as quadrupoles, magnetic dipoles and electrostatic dipoles [3, 4].

In a nuclear reaction experiment, many types of particles are produced when a powerful primary beam bombards a thin target foil. These species include intense primary beams, products from incomplete fusion or transfer reactions, projectile-target fusion products, fusion products from unintended reactions (reactions between beams and target backing or impurities in the target material) and particles knocked off from the target during head-on collisions. The primary function of the recoil separators is to distinguish these various species when they emerge from the target region. Depending upon the particle species we are look-

ing for, we can alter the settings of mass spectrometer.

In heavy-ion reactions, the yield of the complete fusion particle peaks at a small solid angle along the beam direction. Fusion products come out with primary beams like particles. The intensity of the beam background is very high compared to the fusion products. The beam-like particles should inhibit, to obtain a good separation of beam and evaporation residues. Furthermore, the particle of interest is often much smaller in intensity than the incoming beam. As a result, it is pretty challenging to distinguish and separate them from this background of targets and beams. Either the target thickness or the beam intensity must be raised to boost the production rate of reaction products. If the target thickness is increased too much because of the high energy loss in the target, the reaction products might not exit from the target. For nuclear reaction studies, a target thickness is often fixed at a few hundred $\mu g/cm^2$. Most beam particles will escape from the target if the beam intensity is raised. It will harm a detector in it's way. Without recoil separators, neither semiconductor nor gas detectors can handle these forward-focused reaction products. Recoil separators are therefore used for beam rejection, mass analysis of reaction products, transportation of reaction products to a background-free area and final focusing of these products at the focal plane detector so that it can detect all particles of interest.

3.3.1 Categories of recoil separators

In general, two types of the mass spectrometer are developed to accomplish different features. One is a vacuum mode recoil mass separator and another is gas filled mass separator. Since electrostatic elements cannot work in gaseous environments, only magnets are used in gas-filled separators. So the ability of the gas-filled separators to differentiate the particles depends on variations in their magnetic stiffness only. In contrast, vacuum mode separators involve both

magnetic and electric fields.

Ions in vacuum mode separators [3] follow well-defined trajectories, so spectrometers have an excellent mass resolution, which means that the particles are well-separated according to their m/q ratio. They can effectively reject the beam for asymmetric reactions. However, heavy element production is less efficient due to charge state dispersion because not all charge states can pass through the small spectrometer aperture. The transmission efficiency can be improved by using inverse kinematics. In inverse kinematics, the scattering is in a smaller solid angle resulting in most of the particles being within the angular acceptance of the spectrometer. However, inverse kinematics requires a very high energy beam to overcome the Coulomb barrier for the heavier system. In order to achieve better transmission with normal kinematics, gas-filled separators are used in heavy element production. Heavy Ion Reaction Analyser (HIRA) in IUAC is one of the mass-spectrometer working in vacuum mode [5].

The ions traveling in gas-filled separators [6] dispersed according to their magnetic rigidity in the perpendicular magnetic field. The magnetic field region is filled with a dilute gas in gas-filled separators. The ions undergo atomic collisions with the gas molecules in which electrons can be lost or captured, changing the charge state of the ions. If the number of charge-changing collisions is sufficiently high, their charge state fluctuates around average or mean charge state q/m. The ions will closely follow the trajectory determined by the mean magnetic rigidity corresponding to the mean charge state of the ion. Gas-filled separators have good beam rejection capacity and poor mass resolution. Hybrid Recoil mass Analyzer (HYRA) in IUAC is a recoil mass separator working in gas-filled mode [7].

We measured the ER cross-sections of two sets of asymmetric reaction partners in our work. Recoil mass separators working in vacuum mode, which effec-

tively separate recoils of asymmetric reaction partners, are more suitable for our measurements.

3.4 Vacuum mode separators

The underlying idea behind a recoil separator is the Coulomb and Lorentz forces that a charged particle faces when traveling through the electric and magnetic fields. Vacuum mode separators set apart the desired ions from undesired ones using various ion properties like mass, momentum, velocity, mass to charge ratio, kinetic energy, and angular distribution. The ions in a vacuum mode separator take different trajectories according to their properties. The vacuum mode separator employs a magnetic deflector to separate particles based on their momentum, an electrostatic deflector to separate the particles according to their energy and a combined $\mathbf{E} \times \mathbf{B}$ field for velocity selection. Additionally, magnetic multipoles are employed to rectify higher order aberrations and magnetic quadrupoles for focusing the ions.

In a nuclear reaction, when a beam bombards a target, most of the incident beam particles, the reaction products and some target nuclei escape with their initial momentum at various angles around the primary beam direction. The lighter and more energetic primary beam and the heavier and less energetic reaction products have the same momentum. Consequently, they can only be separated based on their energy or velocity, requiring an electrostatic deflector or $\mathbf{E} \times \mathbf{B}$ filter.

An electrostatic deflector consists of two co-axial cylindrical anode and cathode plates. The radial electric field will not significantly deflect positive ions entering the deflector if the energy of the ions is too high and will collide with the anode plate. If the energy is minimal, the ions will be deflected more and collide with the cathode plate. If $\mathbf{E}$ is the electric field between the plates, then

an ion with charge state q, mass m, and velocity v will follow a trajectory with a radius of curvature ρ. The expression for electric rigidity (reluctance of an ion to vary its trajectory according to the applied electric field) can be obtained as follows

$$q\mathbf{E} = \frac{mv^2}{\rho} \tag{3.4}$$

$$\rho\mathbf{E} = \frac{2T}{q} \tag{3.5}$$

Here $\rho\mathbf{E}$ is the electric rigidity and T is the kinetic energy of the ion.

In the same way, a magnetic dipole consists of two opposite magnetic poles. The field is always perpendicular to the direction of motion of ions. Ions moving in a perpendicular magnetic field will follow a circular path with a radius; if ρ is the radius of the circular path, then magnetic rigidity can be written as

$$q(v \times \mathbf{B}) = \frac{mv^2}{\rho} \tag{3.6}$$

$$\mathbf{B}\rho = \frac{mv}{q} = \frac{P}{q} \tag{3.7}$$

Where $\mathbf{B}\rho$ is the magnetic rigidity and P is the momentum

3.5 Heavy-Ion reaction analyser (HIRA)

The Heavy Ion Reaction Analyzer at IUAC is one of the first generations of recoil mass spectrometers [9]. Recoil mass separators are used to separate heavy-ion reaction products from beam particles as they leave a target. The electromagnetic setup of HIRA is shown in Fig. 3.2. The electromagnetic configuration of HIRA is QQ-ED-M-MD-ED-QQ. QQ stands for quadruple doublets, ED and MD designate electric and magnetic dipoles and M for multi-pole. The HIRA

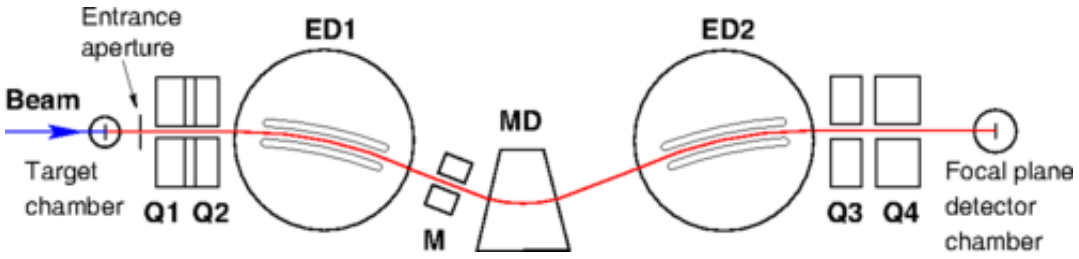

Figure 3.2: Heavy Ion Reaction Analyzer (HIRA) a schematic diagram. Magnetic quadrupole, electrostatic dipole, magnetic multi-pole, and magnetic dipole are represented by the letters Q, ED, M, and MD, respectively [8].

Figure 3.3: A full view of the Heavy Ion Reaction Analyzer (HIRA) setup [8]

has 8.8 meters in length and operates at 0° to the beam direction. It had full acceptance (10 msr). As beam-like and residual particles depart the target, the yield of recoils peaks near 0°, and the recoils mix in with primary beam particles that have not reacted. The beam particles are inhibited at an early stage of the separator to achieve the maximum separation of the beam from recoils. The quadrupole lenses are configured to focus residual particles at the focal plane. The dipole magnetic and electric fields are set to pass a residual particle with energy E_0, mass M_0, and charge Q_0 along the central trajectory.

3.5.1 Target chamber

The spectrometer is positioned on a rotating platform that can rotate from -15 to +40 °. A sliding seal in the target chamber allows the HIRA to rotate freely during experiments while maintaining a high vacuum. These types of vacuum chambers are known as sliding seal chambers. This property will be helpful while investigating multi-nucleon transfer processes [10]. This sliding seal chamber has a 300 mm inner diameter and 200 mm height with replaceable top and bottom plates. The chamber has a large slot on the beam entrance side. During the rotation of HIRA, this chamber can maintain a vacuum in the range of 6×10^{-6} - 4×10^{-6} Torr. A charge reset foil is located 10 cm downstream from the target, to replace the short-lived isomers. HIRA has the option to mount monitor detectors at various angles. Fig. 3.4 shows a photographic view of the target chamber and target mounting.

3.5.2 Quadruple

Two magnetic quadrupole doublets, Q1-Q2 and Q3-Q4, are used respectively before and after the dipoles. HIRA uses Q1-Q2 as the first element in the recoil mass spectrometer to boost the solid angle of acceptance. The first Q1 and

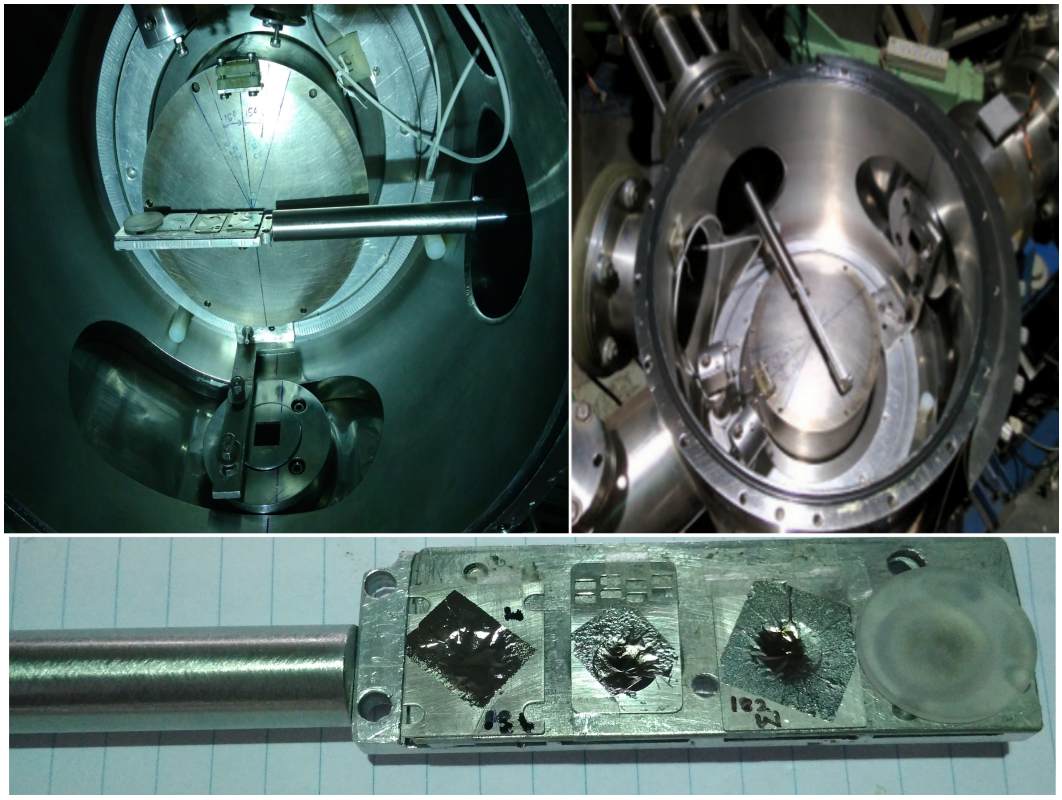

Figure 3.4: The target chamber an interior view, with the target ladder.

Q2 provide a point to parallel focusing of the recoils. Quadrupole doublets are used for the Y-focusing because they have an appropriate mass dispersion at the focal plane. According to the first quadrupole's settings, the second quadrupole is modified. Q1 and Q2 ensure a space where the x and y coordinates are focused at the same location. The m/q value of incoming particles determines the magnetic quadrupole's focusing power. The spectrometer's last quadrupole doublet creates a nearly symmetric configuration. Also, it makes a vertical cross-over at MD, resulting in a smaller vertical size of the image at the focal plane. Apart from a decreased vertical size at the focal plane, the second quadrupole doublet can also give variable mass dispersion across a wide range.

3.5.3 Dispersive elements

Dispersive elements of HIRA, particularly the electrostatic dipoles (EDs) and the magnetic dipole (MD) are arranged symmetrically. Multi-poles are used to correct higher-order aberrations. By using diverse electrical rigidities ($2T/q$)of particles and reaction products, the electric dipole (ED1 and ED2) effectively rejects the beam. On the other hand, magnetic dipole (MD) accomplishes this through m/q selection. A multi-pole (M) element was installed between ED1 and MD to re-optimize the values of the higher aberrations in HIRA. This multi-pole is equipped with a strong sextuple field, which can be used to eliminate position (angle)-related aberrations at the expense of energy-dependent aberrations if necessary. The multi-pole has quadrupole and octupole fields that can be used to correct higher-order aberrations and residual energy dispersion. Mass-dependent aberration is reduced by superimposing appropriate sextupole and octupole fields on the quadrupole field of Q4. Six parameters determine the performance of a dispersive system are the bending radii and angles of the EDs (ρ_E,θ_E) and the MD (ρ_M,θ_M), the separation (d) between the effective field boundaries (EFBs) of ED and MD and the angles ($\aleph$) of the entrance and exit pole faces of MD. The anode plate of the first electric dipole includes a horizontal slot to lead the primary beam onto a beam catcher placed behind it inside the vacuum chamber, improving the spectrometer's beam rejection capabilities.

3.6 Detectors

We used two types of detectors to measure normalised ERs in two highly asymmetric fusion reactions. While measuring ERs as part of the standard HIRA detection system, a multi-wire proportional counter (MWPC) is placed at the focal plane, followed by a position-sensitive silicon detector. Two silicon sur-

face barrier detectors (SSBD) are placed at identical angles (15°) in the target chamber for beam normalization.

3.6.1 Multi wire proportional counter (MWPC)

MWPC is a common detector in heavy-ion-induced nuclear reaction studies. MWPC is a type of proportional counter used to detect charged particles and give positional information on their trajectory. They detect ERs in the focal plane of recoil separators. MWPC is a good choice for heavy-ion detection because of its essential properties such as affordability, radiation resistance, good timing and position resolution, high count rate handling capacity, etc. It can also be created in smaller or larger sizes, depending on the needs of the experiment. Despite its low-energy resolution, the MWPC detector has a high gain and detection efficiency. MWPC used in our measurements are of 4 electrode geometry. They are X, Y, position electrodes, cathode, and anode.

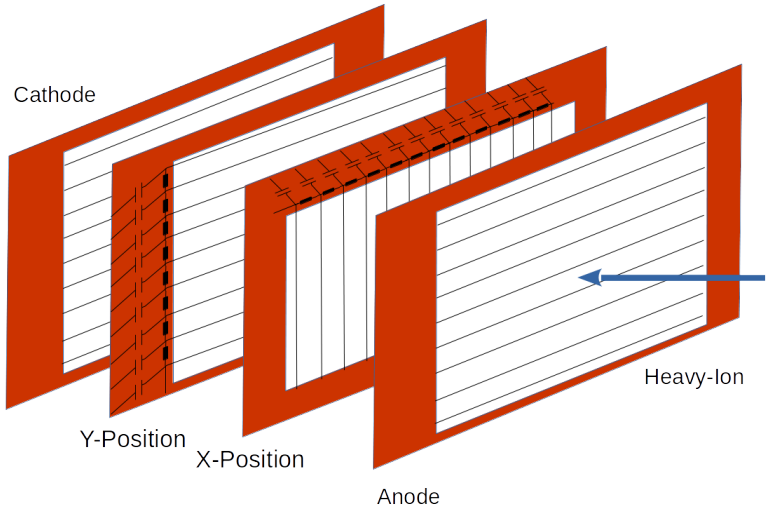

Figure 3.5: The shematic diagram of the MWPC used in ER measurements.

Fig.3.5 shows a schematic diagram of the MWPC detector. In HIRA spectrometer the MWPC used for heavy-ion measurements is Breskin type [11]. The MWPC has a 150×50 mm^2 entrance window. MWPC comprises two position

electrodes (X and Y) sandwiched between anode and cathodes. The reaction product's path is vacuum-sealed ($\approx 10^{-8}$ Torr). A multi-wire proportional counter (MWPC) kept at the focal plane detects particles with various 'm/q' values.

All wire frames of MWPC are made of gold-plated tungsten wires of 20 μm diameter, at a separation of 1.27 mm. The separation between adjacent wire frames is 3.2 mm. The X-wire frame consists of 160 wires, while all other wire frames consist of 80 wires. Position information of the particles hitting the detectors was obtained from resistive network delay-line chips which is shown in Fig. 3.6. A 1 μm thick mylar foil was used to isolate the gas detector from the vacuum chamber. During the ER measurements, isobutane was used as the operating gas at very low pressure (< 3 mbar).

When charged particles enter inside the detector volume, they ionize the medium and results in the production of electric charge pairs. In a gas detector, electron-ion pairs are created. These charge pairs are collected by applying an appropriate electric field and generating electric signals. These signals from the detector contain information about the properties of the incident particle's energy, timing, etc. the amount of charge collected at contact B (in Fig. 3.6) will be proportional to the particle's energy loss ΔE. Also, it will be proportional to the resistance between the point of implantation of the charged particle and the other end. The charge collected at either end of a resistive anode wire is divided in proportion to the length of the wire from the point of injection of the charge to the other end. If Q_A and Q_B are the charges collected at both ends of the anode, as shown in Fig. 3.6, then $\frac{X}{L} = \frac{Q_A}{Q_A+Q_B}$ thus, X and Y Positions can be determined. The delay lines network is coupled to the anode planes of the MWPC using the anode signal or some other triggering signal as a start. The time difference between the arrival of the signals at both ends of the delay line

is measured and given to the Timing filter amplifier(TFA). It acts as the start pulse for TOF measurements.

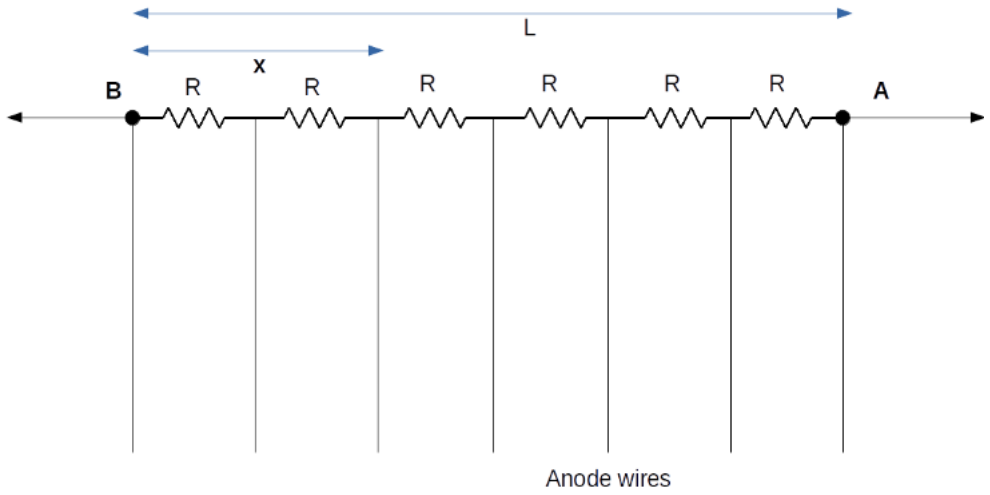

Figure 3.6: The shematic diagram of the delay line set-up for position information in MWPC

3.6.2 Monitor detectors

Inside the target chamber, we used two silicon surface barrier detectors (SSBDs) as monitor detectors. They are essentially p-n junction diodes with electrical characteristics that fall between insulators and conductors. They were designed to detect elastically scattered beam particles and monitor the beam for absolute normalization of ER cross-sections. These detectors were positioned at ≈15° from the beam direction in the horizontal plane. The monitor detectors are of 100 micron thickness with an active area of 1 mm^2. They are placed at around 90 mm distance from the target.

3.7 Data acquisition system

We measured ER cross-sections for $^{16,18}O+^{181}Ta$ and $^{18}O+^{182,184,186}W$ reactions. The block diagram of the electronics set-up used in the data acquisition is shown in Fig. 3.7. The energy and position signals from MWPC (cathode, XL, XR,

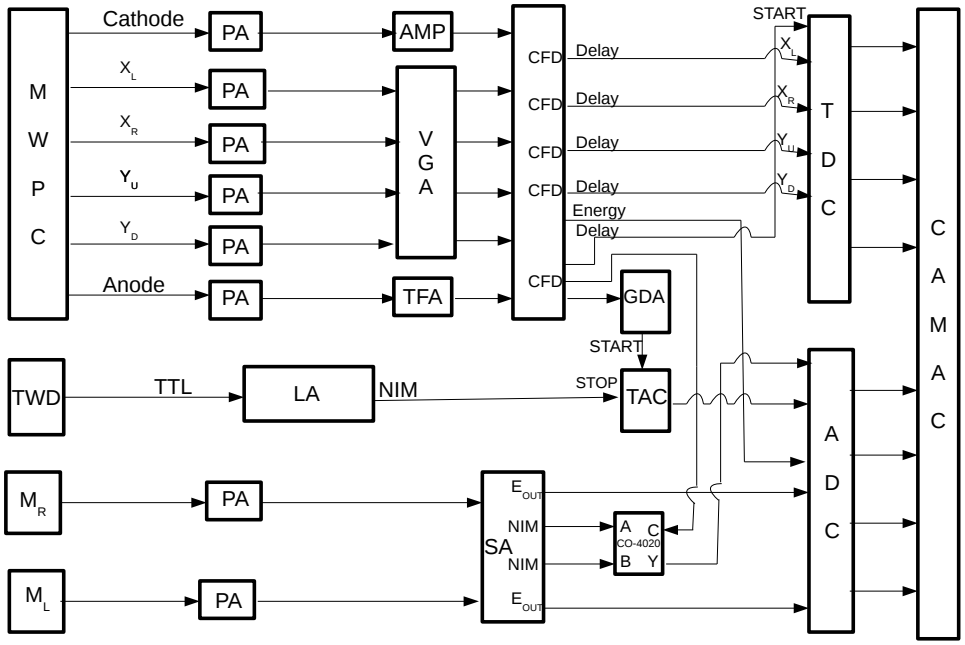

Figure 3.7: Block diagram of the electronics setup used in ER measurements.

YU and YD) were processed through pre-amplifiers and amplifiers. One variable gain amplifier (VGA) was used for four-position signals. The signal is applied to constant fraction discriminator (CFD) after sufficient amplification and shaping to extract excellent time resolution using a Timing filter amplifier (TFA). The four-position and a delayed CFD signal are then fed to the Time to Digital Converter(TDC). Delayed signals are used to put the events recorded within the TDC range. A delayed anode signal was used as a start for TDC. Pre-amplifiers, amplifiers, and the analog to digital converter (ADC) were used to handle the cathode signal from the MWPC and the Monitor detector signal (ML and MR). We employed a "spectroscopic amplifier" (SA) designed by IUAC [12] that shapes the signal and gives the time signal. Using a logic fan in-fan out unit, these time signals and the 'MWPC anode' were logically OR'ed. This signal was used as the ADC's master strobe.

The ER's time-of-flight (TOF) is defined as the time taken by ER to travel

from the center of the target to the focal plane (a distance of 8.6 meters), and it is calculated as the time difference between the reaction time (arrival of beam pulse) and the detection time of ER. The TTL signal from the traveling wave deflector (TWD) (corresponds to RF-signal) is converted to NIM signals by time to amplitude converter (TAC). There is an uncertainty in the reaching of ERs in the FP detector within the the pulse repetition rate (4μs). This will cause an inaccuracy in the in time-of-flight measurement if the 'stop' was from the MWPC anode. To avoid this ADC would have been initiated for the arrival of the next pulse at the reaction point when a delayed ER reaches the focal plane and initiates a 'stop'. Thus, the signal from the anode is used as the 'start' and TWD as the 'stop'. This time difference is the TOF in the true sense.

3.8 Experimental Details

The experiment was performed using the HIRA facility at IUAC. Pulsed beams of ^{16,18}O with 4 μs pulse separations were used to bombard ^{181}Ta and ^{182,184,186}W targets. Two monitor detectors were mounted on the target chamber to monitor the incidence of beam on the target. Monitor counts were used to normalize the absolute ER cross-sections. Apart from the target, one slot in the target ladder was mounted with quarts, used for beam focusing.

The beam was first tuned on the quartz mounted on the target ladder. Targets were introduced to the beam position once the beam was successfully tuned on quartz. The mean charge state was calculated using a simulation code [13] using the empirical formula [14, 15] available in the literature. For maximum transmission efficiency of HIRA, optimum charge states, energy and mass of residual particles for particular energy are obtained through corresponding scanning. The scanning of mass, charge state and energy were done at an E_{lab} which is at the middle of the considered energy range. For ^{16,18}O+ ^{181}Ta the scanning

were done at E_{lab} = 90.0 MeV. The optimum values of mass, charge state and energy were obtained as 197 amu, $8p^+$ and 5.805 MeV.The optimum values of all other energy points are done by scaling the corresponding states. For $^{16}O+ \ ^{181}Ta$ reaction at E_{lab} = 94.0 MeV, the charge states were optimised at $8p^+$, energy are at 6.06 MeV and mass at 197 amu. Correspondingly the dipole field values were set for maximum transmission efficiency. Data were collected for the maximum transmission at the focal plane detector.

To detect the ERs, an MWPC having an active area of 150 mm × 50 mm was placed at the focal plane of the HIRA. The MWPCs entrance window was made of a thin mylar foil, separating the MWPCs gas volume from the vacuum within the HIRA. After losing energy in the target foil, polypropylene foil, and isobutane gas, the ultimate energy of the ER at the focal plane was ≈ 1.5 MeV at the lowest bombarding energy. The forward-focused recoils must be isolated from the background of scattered beam-like and target-like particles in fusion cross-section measurements. The slowly moving ERs produced at the target chamber took ≈ 4 μs to reach the focal plane. The TOF set-up helped us have a very clean separation of ERs from the beam-like and target-like contaminations. Fig. 3.8 shows the two-dimensional plot of energy loss (ΔE) of the particles in MWPC detector versus TOF at E_{lab} = 94.0 MeV ($E_{c.m.}$ = 86.15 MeV) for the reaction $^{16}O+ \ ^{181}Ta$.

In the target ladder, one position was kept empty. In lower energy runs, this blank position aids in background subtraction. The production of ERs drops while the yield of background events increases at below-barrier energies. Thus a clear identification of ERs become difficult as the E_{lab} decreases. So a background subtraction run was taken below the Coulomb barrier energy by putting blank positions of the target ladder at the incident beam. ΔE verses ToF spectrum at 68 MeV for for the reaction $^{16}O+ \ ^{181}Ta$ with and without target are shown

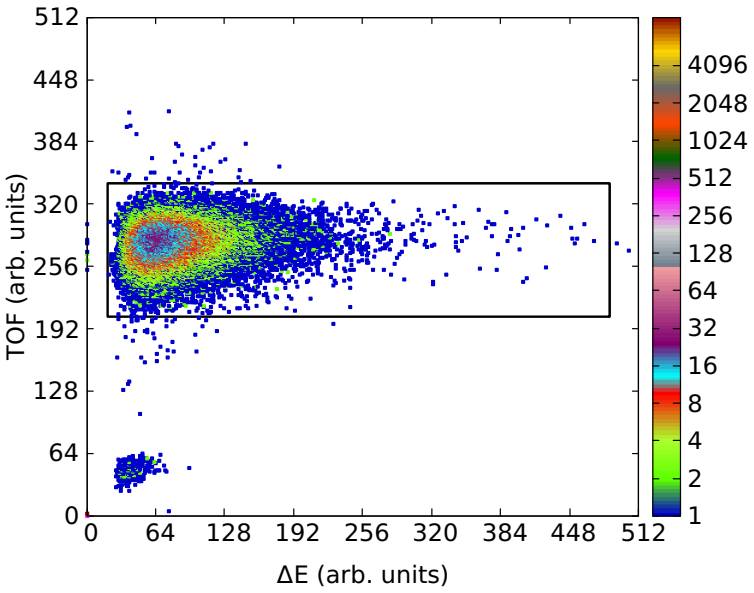

Figure 3.8: ΔE verses TOF spectrum recorded at the focal plane of HIRA for an asymmetric reaction. The spectrum shows the scatter plots of ^{16}O+ ^{181}Ta at 94.0 MeV E_{lab} ($E_{c.m.}$ = 86.15 MeV).

in Fig. 3.9. Freedom [16] and Candle [17], IUAC's in-house data acquisition programs, were used to record and analyse data.

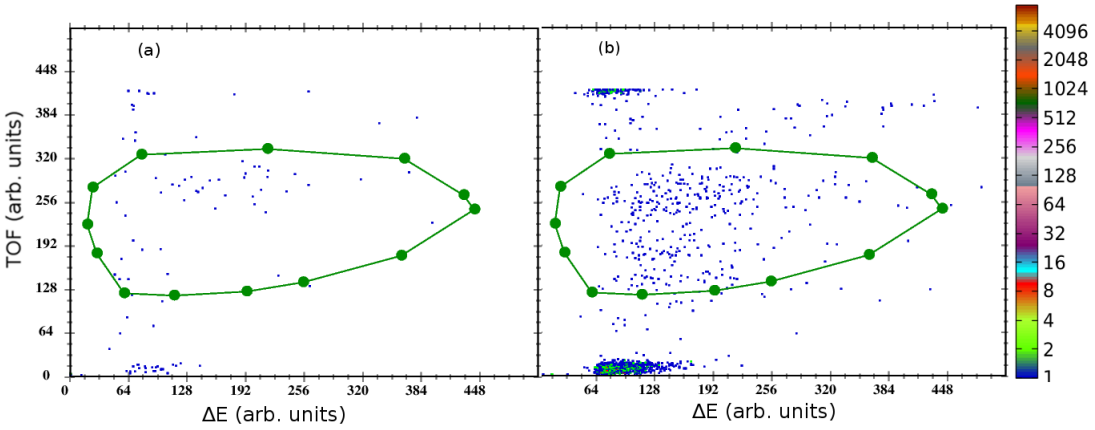

Figure 3.9: ΔE verses TOF spectrum recorded at the focal plane of HIRA for ^{16}O+ ^{181}Ta at 68.0 MeV E_{lab}. (a) shows the scatter plot without target and (b)that of with target.

Another matter of considerable importance in the operation of any recoil mass separator is its transmission efficiency. For proper planning and execution of the experiment with a recoil separator, it is necessary to measure the transmission efficiency of the system accurately. Transmission efficiency of HIRA is defined as

the the ratio of number of ER reaching the focal plain to that of emerging from the target.

$$\epsilon_{HIRA} = \frac{No:\ of\ ER\ reaching\ the\ focal\ plain\ detector}{No:\ of\ ER\ emerging\ from\ target} \tag{3.8}$$

ϵ_{HIRA} is a function of beam energy, target thickness, size of the focal plane detector, entrance channel mass asymmetry, exit channel of interest, angular acceptance of the HIRA, and settings of the HIRA. Among these, the factors that do not change during the experiment are the entrance channel mass asymmetry, target thickness, angular acceptance of the HIRA, and size of the focal plane detector. Therefore, ϵ_{HIRA} would be unique for each E_{lab}. Several evaporation channels will be populated for single beam energy. Usually, HIRA is set for the most dominant channel. The transmission efficiency corresponding to that particular channel will be the maximum. Other less dominant ER channels will transmit with lower efficiency (that is with lower value of ϵ_{HIRA}). That is the efficiency of each channels, that populate at a particular E_{lab} will be different.

The efficiency of HIRA is measurable for each exit channel at a particular E_{lab}. Characteristic γ-rays from ERs have to record in singles, and in coincidence with the ERs, detected at the focal plane of the separator. The ratio of counts of a specific γ-line, corresponding to a particular ER, in coincidence spectrum to that in the singles spectrum gives the absolute transmission efficiency of the separator. This method is successful only for dominant channels since it required good statistics in each γ-line. Experimental determination of transmission efficiency for weak exit channels of a reaction is not practicable due to poor statistics in the γ line. For very weak channels, we needs to depend on a reliable theoretical estimate of transmission efficiency. We can calculate ER angular and energy distributions using a standard statistical model code PACE-4 [18]. Charge state distributions can be estimated using formulae available in literature [14, 15].

These distributions may then be combined with the corresponding acceptances of the separator to estimate transmission efficiency [19].

Considering all these, measuring ϵ_{HIRA} for all exit channels of each E_{lab} will be a tedious task. So a semi-microscopic Monte Carlo code named TERS was developed for calculating absolute Transmission Efficiency of Recoil Separators like HIRA [20, 21]. Several features like trajectory plots, one and two-dimensional position spectra and quantitative information on survival of ERs at different locations of the separator are offered by this code. Efficiency calculations using TERS matches well with measured efficiency values of many reaction sets [22]. So we relied on TERS [20, 21] for efficiency calculation. We have calculated the ϵ_{HIRA} for all channels (which contribute more than $\approx 1\%$ of total ER cross-section) using TERS and estimated $\bar{\epsilon}_{HIRA}$ (average efficiency) for each energy, by taking the weighted average of all ϵ_{HIRA} over total ER. The relative population of each channel for calculating the weighted average was estimated using statistical model code PACE4 [18].

Bibliography

[1] D. Kanjilal, S. Chopra, M. Narayanan, I. Iyer, V. Jha, R. Joshi, and S. Datta, Nuclear Instruments and Methods in Physics Research Section A **328**, 97 (1993).

[2] G. Mehta and A. Patro, Nuclear Instruments and Methods in Physics Research Section A: Accelerators, Spectrometers, Detectors and Associated Equipment **268**, 334 (1988).

[3] C. N. Davids, Nuclear Instruments and Methods in Physics Research Section B: Beam Interactions with Materials and Atoms **204**, 124 (2003), 14th International Conference on Electromagnetic Isotope Separators and Techniques Related to their Applications.

[4] C. E. Dllmann, Nuclear Instruments and Methods in Physics Research Section B: Beam Interactions with Materials and Atoms **266**, 4123 (2008), proceedings of the XVth International Conference on Electromagnetic Isotope Separators and Techniques Related to their Applications.

[5] A. Sinha, N. Madhavan, J. Das, P. Sugathan, D. Kataria, A. Patro, and G. Mehta, Nuclear Instruments and Methods in Physics Research Section A: Accelerators, Spectrometers, Detectors and Associated Equipment **339**, 543 (1994).

[6] A. Ghiorso, S. Yashita, M. Leino, L. Frank, J. Kalnins, P. Armbruster, J.-P. Dufour, and P. Lemmertz, Nuclear Instruments and Methods in Physics Research Section A: Accelerators, Spectrometers, Detectors and Associated Equipment **269**, 192 (1988).

[7] N. Madhavan, S. Nath, T. Varughese, J. Gehlot, A. Jhingan, P. Sugathan, A. K. Sinha, R. Singh, K. M. Varier, M. C. Radhakrishna, E. Prasad,

S. Kalkal, G. Mohanto, J. J. Das, R. Kumar, R. P. Singh, S. Muralithar, R. K. Bhowmik, A. Roy, R. Kumar, S. K. Suman, A. Mandal, T. S. Datta, J. Chakko, A. Choudhury, U. G. Naik, A. J. Malayadri, M. Archunan, J. Zacharias, S. Rao, M. Kumar, P. Barua, E. T. Subramanian, K. Rani, B. P. A. Kumar, and K. S. Golda, Pramana Journal of Physics **75**, 317 (2010).

[8] Heavy ion reaction analyzer.

[9] T. M. Cormier, Annual Review of Nuclear and Particle Science **37**, 537 (1987), https://doi.org/10.1146/annurev.ns.37.120187.002541.

[10] D. O. Kataria, A. K. Sinha, J. J. Das, N. Madhavan, P. Sugathan, L. T. Baby, I. Mazumdar, R. Singh, C. V. K. Baba, Y. K. Agarwal, A. M. Vinodkumar, and K. M. Varier, Phys. Rev. C **56**, 1902 (1997).

[11] A. Breskin, R. Chechik, Z. Fraenkel, P. Jacobs, I. Tserruya, and N. Zwang, Nuclear Instruments and Methods in Physics Research **221**, 363 (1984).

[12] A. Gupta, S. Venkataramanan, and P. Sugathan, Compact dual channel spectroscopy amplifier cum discriminator, in *DAE Symp. Nucl. Phys.* (2013), volume 58, p. 926.

[13] S. Nath and N. Madhavan, in IUAC annual report, section 4.3.3 p. 103-105 (2006) .

[14] V. S. Nikolaev and I. S. Dmitriev, Phy. lett. A **28**, 287 (1968).

[15] R. N. Sagaidak and A. V. Yeremin, Nuclear Instruments and Methods in Physics Research Section B: Beam Interactions with Materials and Atoms **93**, 103 (1994).

[16] B. P. A. Kumar, E. T. Subramaniam, K. Singh, and R. K. Bhowmik, In Pro-ceedings of SANAI-97, Trombay (1997) .

[17] E. T. Subramaniam, B. P. A. Kumar, and R. K. Bhowmik, (http://www.iuac.res.in/NIAS) .

[18] A. Gavron, Phys. Rev. C **21**, 230 (1980).

[19] S. Nath (2011).

[20] S. Nath, Comput. Phys. Commun. **181**, 1659 (2010).

[21] S. Nath, Comput. Phys. Commun. **180**, 2392 (2009).

[22] S. Nath, P. V. M. Rao, S. Pal, J. Gehlot, E. Prasad, G. Mohanto, S. Kalkal, J. Sadhukhan, P. D. Shidling, K. S. Golda, A. Jhingan, N. Madhavan, S. Muralithar, and A. K. Sinha, Phys. Rev. C **81**, 064601 (2010).

Chapter 4

ER measurements, analysis and results for ^{16,18}O+^{181}Ta reactions

4.1 Introduction

In heavy-ion collision, after capture the projectile-target system may re-separate before complete equilibration via quasi-fission [1–5] or fast-fission at higher energies. This reduces the possibility of compound nucleus formation (P_{CN}). At higher energies, the corresponding decrease in ER cross-section is only mildly affected by nuclear potentials [6, 7] and is typically calculated using standard statistical model (SSM) parameters such as level density parameters in fission and evaporation channels (a_f/a_n), rotating liquid drop fission barrier $B_f^{LD}(\ell)$ [8] (through a scaling factor k_f) and ground state shell correction δW_{gs} [9]. Usually, SSM calculations are carried out with a set of parameters [3, 10]. Default values of all these parameters with $P_{CN} < 1$ indicates the presence of fusion suppression for systems forming the same CN. SSM calculations are used to generate the theoretical fission and ER excitation functions of systems having the same compound nuclei, utilising the same nuclear potential parameter values, fission barrier, and various P_{CN} [7, 11]. In such calculations say values of P_{CN} <1 indi-

cates the presence of non-compound nuclear fission processes in systems forming the same CN. However, there is no clear understanding of the factors affecting the P_{CN} [12]. In time-independent or dynamical approaches to approximate the value of P_{CN}, different models assume different dependent factors such as mass asymmetry, elongation, or both. [13, 14]. Also, their predictions differ by order of magnitude [15, 16].

According to studies on the ER excitation function measurements of ^{219,221}Ac nuclei [7], QF was found in ^{16}O induced reactions. For extremely asymmetric combinations of colliding nuclei, the ER production of the compound nucleus ^{216}Ra was markedly suppressed [17–20]. Furthermore, for particularly asymmetric combinations of colliding nuclei, many experiments reported the presence of QF in the pre-actinide region [6, 21–26]. In extremely asymmetric reactions that produced the pre-actinide nucleus ^{213}Fr, Corradi et al. [6, 21] observed a fusion suppression effect. QF is also observed in reactions forming less fissile ^{210}Rn [22, 23], ^{202}Po [24, 26] and ^{202}Pb [25] nuclei with close mass asymmetry in the reaction entrance channel. Recently, certain approximative boundaries for fusion suppression at the BG point were suggested by Banerjee *et al.* [27] based on systematic analysis of fission and ER excitation functions in the mass region 170-220.

Near Businaro-Gallone point, which is the highest of all conditional saddle points, systems with mass asymmetry (α) values less than α_{BG} advance to quasi-fission. Otherwise, they proceed to CN formation [28]. Among several projectile and target combinations leading to the same CN, for systems with quasi-fission, the measured fission cross-section will be the sum of compound and non-compound nuclear fission cross-sections. For systems forming same CN, Sagaidak and co-workers [19, 21] considered fission barrier scaling factor of the most asymmetric system to explain the fission cross-section, and tried to

reproduce the measured ER and fission cross-sections for all others by varying P_{CN}. Also, there were attempts to use an excitation energy dependant fission barrier instead of a single value [29, 30]. The ER cross-sections of ^{19}F+^{194}Pt forming ^{213}Fr compound nuclei are explained through a fission barrier scaling factor k_f =0.78 [21]. This value of k_f is remarkably smaller than that of ^{16}O induced reaction (k_f = 0.82 [6]) forming the same CN. Using the fission barrier scaling factors of ^{16}O+^{197}Au reactions in ^{19}F+^{194}Pt, Sagaidak *et al.*[21] reduced the P_{CN} value of the latter from 1 to 0.75. This reduction in P_{CN} can be considered as evidence for fusion suppression. To have a better understanding of the starting point of NCNF processes in Fr compound nucleus near BG point, Corradi *et al.*[6] considered ^{18}O+^{197}Au and ^{9}Be+^{209}Bi reactions which form ^{215,218}Fr compound nuclei respectively. They obtained the same fission barrier scaling factor 0.85 for both reactions irrespective of their neutron number. This indicates that the triggering point of fusion suppression in Fr compound nuclei may be at ^{19}F. Less fissile systems which form Pb compound nucleus showed contradictory results [31] on carrying out similar investigations. Theoretical calculations on systems, forming ^{200}Pb, using di-nuclear system (DNS) model [32], point to a relevant fusion suppression in ^{19}F induced reactions (^{19}F+^{181}Ta) in comparison with that of ^{16}O induced one(^{16}O+^{184}W). Also, Banerjee *et al.* [27] in their systematics, predicted a fusion probability less than unity for ^{19}F+^{181}Ta and unity for ^{16}O+^{184}W. Sagaidak *et al.*[31] came up with the same fission barrier scaling factor (k_f = 0.85) for both ^{19}F+^{181}Ta and ^{16}O+^{184}W with P_{CN} = 1, which clearly indicates absence of fusion suppression in those systems. This contradicts the concept that fusion suppression can observe even for lighter projectiles, such as ^{19}F, as reported by Ref. [32] and Ref. [27].

As a result, more experimental data in this area is critical for a better

understanding of the interaction between CN production and the formation of competing reaction channels. In the present work, we report the results of ^{16,18}O+^{181}Ta which form compound nuclei ^{197,199}Tl, and their ER excitation function measurements at near and above the Coulomb barrier energies using a mass spectrometer. Among this, ^{18}O+^{181}Ta has $\alpha < \alpha_{BG}$ which indicates the presence of NCNF. Further, a comprehensive comparison of the present work with ^{19}F+^{180}Hf ($\alpha < \alpha_{BG}$) reaction [33] which form the same CN ^{199}Tl was made, to determine the point at which less fissile reactions trigger quasi-fission.

4.2 Experimental details

Pulsed beams of ^{16,18}O with pulse separation 4 μs were bombarded on ^{181}Ta target of thickness 170 μg/cm^2 with 20 μg/cm^2 carbon backing. ER excitation function measurements were carried out in 2 MeV energy steps at laboratory beam energies ranging between 64–110 MeV. ERs were separated from profound primary beam background by the HIRA [34] HIRA was operated at an acceptance of 10 msr. Two silicon surface barrier detectors of active area 50 mm^2 each with a 1 mm collimator diameter were placed at a distance of 95.6 mm from the target, in the sliding-seal scattering chamber at $\pm$ 15° with respect to the beam direction to detect the Rutherford scattered particle. At the FP of HIRA, a two dimensional position sensitive multi-wire proportional counter (MWPC) of an active area 150×50 mm^2 was used to detect the ERs. A 0.5 μm thick mylar foil was used as the entrance window of MWPC, to separate the gas volume from the vacuum of HIRA.

4.3 Data analysis

The measured ER cross-sections were obtained using the equation

$$\sigma_{ER} = \frac{Y_{ER}}{Y_{norm}} \left(\frac{d\sigma}{d\Omega}\right)_{Ruth} \Omega_{norm} \left(\frac{1}{\overline{\epsilon}_{HIRA}}\right) \tag{4.1}$$

where Y_{ER} is the number of ERs detected at the FP of the HIRA, Y_{norm} is the number of scattered beam particles detected by any of the normalization detectors, Ω_{norm} is the solid angle subtended by the normalization detectors and $\overline{\epsilon}_{HIRA}$, is the average ER transmission efficiency of HIRA. The significant part of the error in total cross-section were contributed by efficiency calculations. $(\frac{d\sigma}{d\Omega})_{Ruth}$ is the differential Rutherford-scattering cross-section in the laboratory system which is obtained as

$$\frac{d\sigma}{d\Omega} = 1.296 \left(\frac{Z_p Z_T}{E_{lab}}\right)^2 \left[\frac{1}{sin^4(\theta/2)} - 2\left(\frac{M_p}{M_T}\right)^2 + ...\right] \tag{4.2}$$

here Z_p, Z_t, A_p and A_t are the atomic and mass numbers of the projectile and target, respectively. E_{lab} and θ are the energy of the incident projectile and scattering angle of the projectile-like particles in the laboratory frame of reference, respectively. The scatter plot of ΔE versus TOF at E_{lab} = 100 MeV and 68 MeV for the reaction ^{16}O+^{181}Ta is shown in Fig. 4.1. Scatter plots for the reactions ^{18}O+^{181}Ta at E_{lab} = 100 MeV and 68 MeV are shown in Fig. 4.2. At lower beam energies, a "Blank" target run was used to estimate background at the focal plane of HIRA. Such a background correction was introduced for the low energy measurements.

It is crucial to understand the possible sources of error in each experiment. In measurements with HIRA, the majority of the error in the final cross-section is contributed by $\tilde{\epsilon}_{HIRA}$. The statistical error in each detector output is given by

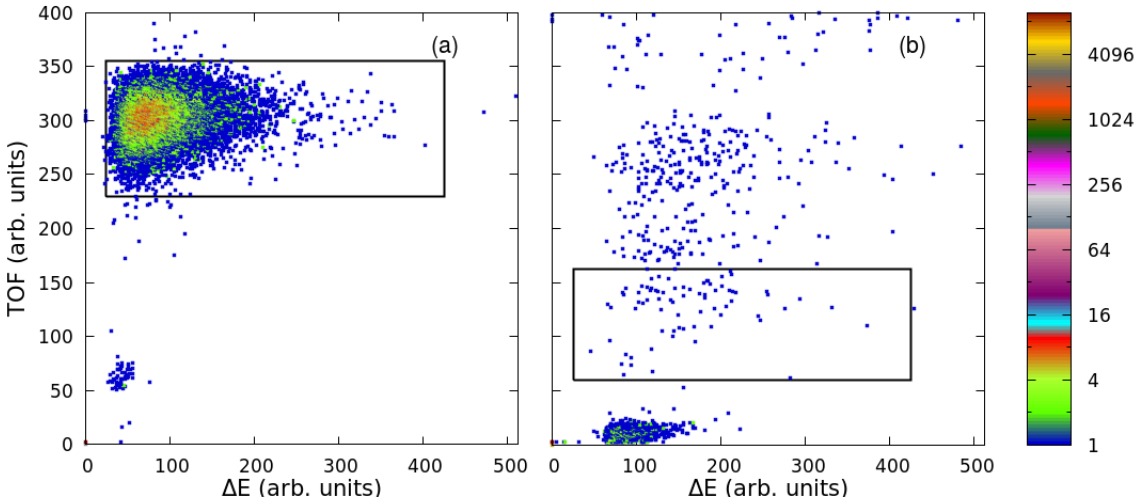

Figure 4.1: ΔE verses TOF spectrum recorded at the focal plane of HIRA for ^{16}O+ ^{181}Ta at 100.0 MeV and 68 MeV E_{lab}

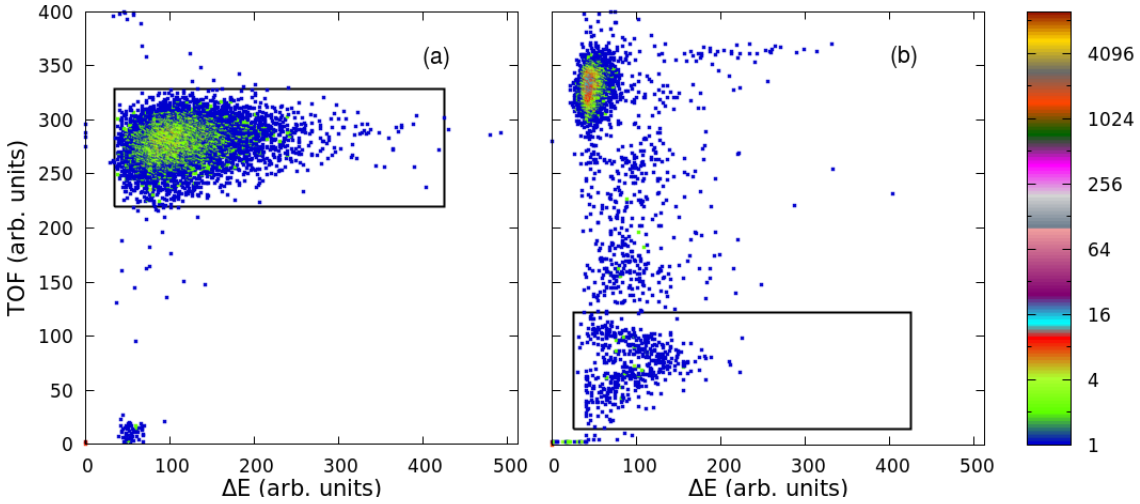

Figure 4.2: ΔE verses TOF spectrum recorded at the focal plane of HIRA for ^{16}O+ ^{181}Ta at 100.0 MeV and 68 MeV E_{lab}

$\frac{1}{\sqrt{N}}$ where N is the number of counts. While taking the sums and ratios of the detector counts, the standard error propagation formula was used to calculate the error involved in the derived quantities.

The ER cross-sections obtained for ^{16,18}O+^{181}Ta reactions after the data reduction are given in Table 4.1. Here E_{lab} is the beam energy obtained from the accelerator. $E_{c.m}$, is the center of mass energy estimated after including the losses in the backing and half thickness of the target. Excitation energies in the Table 4.1 are calculated as $E_{c.m} - Q$. Here Q represents the nuclear reaction Q-value, which is the amount of energy absorbed or released during a nuclear reaction. ^{16,18}O+^{181}Ta reactions Q-value used are -24.83 and -21.16 [35]. The Overall error in the measurement was estimated to be $\leq$15%. Major part of this error was contributed by ϵ_{HIRA}.

^{16}O+^{181}Ta					^{18}O+^{181}Ta				
E_{lab} (MeV)	$E_{c.m.}$ (MeV)	E^* (MeV)	ϵ_{HIRA} (%)	σ_{ER} (mb)	E_{lab} (MeV)	$E_{c.m.}$ (MeV)	E^* (MeV)	ϵ_{HIRA} (%)	σ_{ER} (mb)
110.0	100.88	76.04	1.63	940 ± 108	110.0	99.90	78.73	2.04	983 ± 114
108.0	98.95	74.11	1.77	977 ± 111	108.0	98.16	76.99	2.07	988± 114
106.0	97.26	72.42	1.85	961 ± 107	106.0	96.29	75.12	2.10	1001 ± 112
104.0	95.44	70.60	1.86	998 ± 113	104.0	94.43	73.26	2.12	1033 ± 120
102.0	93.58	68.74	1.90	982 ± 108	102.0	92.61	71.44	2.37	938± 105
100.0	91.68	66.84	1.86	973 ± 108	100.0	90.84	69.67	2.45	945± 110
98.0	89.89	65.06	1.98	870 ± 96	98.0	88.85	67.69	2.41	958± 111
96.0	88.00	63.16	2.08	787 ± 86	96.0	87.19	66.02	2.54	858± 99
94.0	86.15	61.13	2.12	764 ± 81	94.0	85.24	64.08	2.55	835± 90
92.0	84.30	59.46	2.17	737 ± 80	92.0	83.57	62.40	2.75	747± 81
90.0	82.47	57.63	2.28	621 ± 66	90.0	81.74	60.58	2.91	783± 91
88.0	80.73	55.89	2.29	607 ± 67	88.0	79.79	58.62	3.00	681± 77
86.0	78.71	53.87	2.17	533 ± 56	86.0	78.11	56.95	2.92	618± 70
84.0	77.00	52.16	2.05	454 ± 48	84.0	76.29	55.13	2.70	613± 69
82.0	75.18	50.35	1.93	384 ± 41	82.0	74.49	53.33	2.62	453± 48
80.0	73.21	48.37	1.87	281 ± 30	80.0	72.63	51.46	2.45	307± 33
78.0	71.36	46.52	1.92	195 ± 20	78.0	70.61	49.44	2.34	206± 22
76.0	69.64	44.81	1.94	101 ± 15	76.0	69.01	47.84	2.22	131± 14
74.0	67.83	43.00	1.91	47.6± 5.2	74.0	67.12	45.95	2.32	51.0± 5.6
72.0	65.95	41.11	1.59	16.14±1.78	72.0	65.30	44.13	2.34	17.41 ±1.96
70.0	64.11	39.27	1.55	2.93± 0.37	70.0	63.33	42.17	2.18	3.44±0.41
					68.0	61.51	40.35	2.05	0.39±0.06

Table 4.1: Measured evaporation residue cross-sections (σ_{ER}) for ^{16,18}O+^{181}Ta reactions along with transmission efficiency (ϵ_{HIRA}) of the spectrometer. Tabulated energies are in center of mass systems. Here the sum of statistical and systematic errors are quoted as the total error in the measurement.

4.4 Results and discussion

A nucleus is a many-body quantum-mechanical system. The challenge lies in whether to consider degrees of freedom in this many body system statistically or exactly. At lower excitation energies consideration of the different degrees of freedoms such as collective surface vibration, deformation of colliding nuclei and neutron transfer, coupled channels calculation [36] explains the fusion cross-section quite well. Nuclear fission and particle evaporation are the dominant modes of decay at higher excitation energies. Their excitation functions at energies well above the Coulomb barrier are weakly sensitive to the form of nuclear potential and are mainly determined by the standard statistical model parameters. In the present study, coupled channels calculation have been carried out, to explore the effect of different coupling states of target and projectile, below the Coulomb barrier energy region and statistical model calculations to understand the decay mechanisms in the higher excitation energies.

4.5 Coupled channel calculations

Coupled Channels(CC) calculations of ^{16,18}O+^{181}Ta are performed to determine the effect of structure of the colliding nuclei on fusion cross-sections in the energy region below the Coulomb barrier. A modified version of CCFULL code by Hagino et al. [36, 37] is used in the present CC calculation. For ^{16,18}O+^{181}Ta reactions, the estimated fission cross-sections using Pace4 was found to be very less at the highest energies where measurements were carried out. Hence, ER cross-sections in the energy range of measurements were considered as σ_{fus} in the CC calculations. Woods-Saxon parameters, depth of potential (V_0), radius (r_0) and diffuseness (a) for coupled channel calculations are taken from those of the nearest systems (^{16}O+^{186}W) used by Firihu *et al.* [42]. Slight variations in the

Nucleus	^{16}O	^{18}O	^{181}Ta	Ref
E_{2^+} (MeV)		1.982	0.0967	[38, 39]
β_2		0.355	0.262	[38, 40]
E_{3^-} (MeV)	6.130			[41]
β_3	0.729			[41]

Table 4.2: Deformation parameters and excitation energies used in coupled channel calculations for ^{16,18}O+^{181}Ta reactions.

Woods-Saxon parameters used for the CC calculations of ^{16}O+^{186}W by Firihu *et al.* were done. The changes are made in such a way that their combinations produce a fusion barrier which is equal to the experimental fusion barrier of ^{16}O+^{181}Ta reaction. Finally,the Woods-Saxon parameters for the CC calculations of ^{16,18}O+^{181}Ta reactions were fixed as $V_0 = 92.25$ MeV, $r_0 = 1.15$ fm and $a = 0.73$ fm. The cross-sections from CCFULL calculations with these potential parameters without including any coupling are termed as 1D-BPM excitation function and is represented by the dashed lines in Fig. 4.3 and 4.4.

4.5.1 CC calculations for ^{16}O+^{181}Ta

For ^{16}O+^{181}Ta reaction, coupling of relative motion of the nuclei with the rotational state of deformed target (β_4 = -0.090 [43]) explained the sub-barrier fusion enhancement in the lower energy region as shown by the solid lines in Fig. 4.3. Coupling with the lowest 3^- state of ^{16}O at 6.1 MeV with $\beta_3 = 0.729$ destroys the agreement between experiment and theory. The coupling calculations with 3^- vibrational state of ^{16}O is shown by dotted lines in Fig. 4.3. This indicates that the effects of this excitation are already included in the bare potential itself. In such a case, the effect of the coupling to the 3^- state of ^{16}O is double-counted if the coupled-channel calculations explicitly take it into account, resulting in an overestimation of the experimental cross-sections [44]. Therefore, this coupling

was not included in CC calculations. The fusion excitation functions and results of the CCFULL calculations of ^{16}O+^{181}Ta reaction are shown in Fig. 4.3. In this figure the 1D BPM calculations explain the data well in the above-barrier region. The couplings of the relative motion of the colliding nuclei with rotation of target nuclei CC model, explains the data up to the lowest energy.

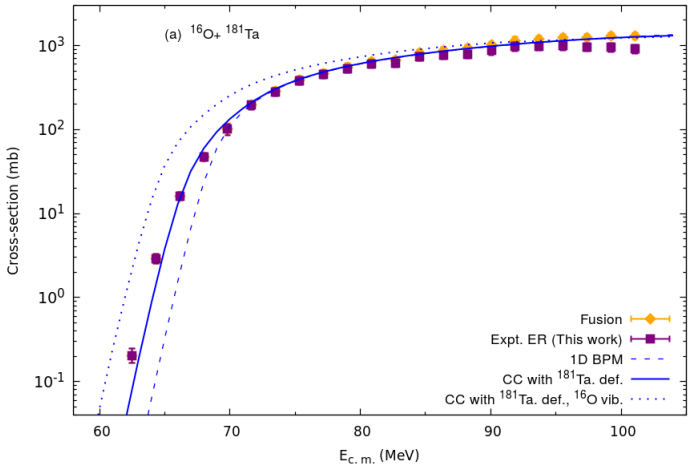

Figure 4.3: Measured ER excitation function as a function of $E_{c.m.}$, for the system ^{16}O+^{181}Ta along with CC calculations. Solid line represent CC calculations with coupling and dashed line represents the 1D-BPM (CC calculations without coupling).

4.5.2 CC calculations for ^{18}O+^{181}Ta

For ^{18}O+^{181}Ta, the 2^+ rotational state the target nuclei with quadrupole deformation 0.335 and hexa-decupole deformation 0.262 fails to explain the experimental cross-sections in the below-barrier energy region. Further, the vibrational effect of the ^{18}O reactions were included in the coupling calculations. 2^+ vibrational states of projectile with single phonon state and quadrupole deformation of target included in the CC calculations shows lower cross-sections than the experimental one as shown by dash dotted lines in Fig. 4.4. On increasing the phonon states to 3 in the vibrational state of the projectile, CC calculations explains the corresponding experimental excitation function in the below barrier

region as shown by solid lines in Fig. 4.4. In Fig. 4.4 the 1D BPM calculations explain the data well in the above-barrier region. The couplings of the relative motion of the colliding nuclei with vibration of projectile and rotation of target nuclei CC model, explains the data up to the lowest energy for both the reactions.

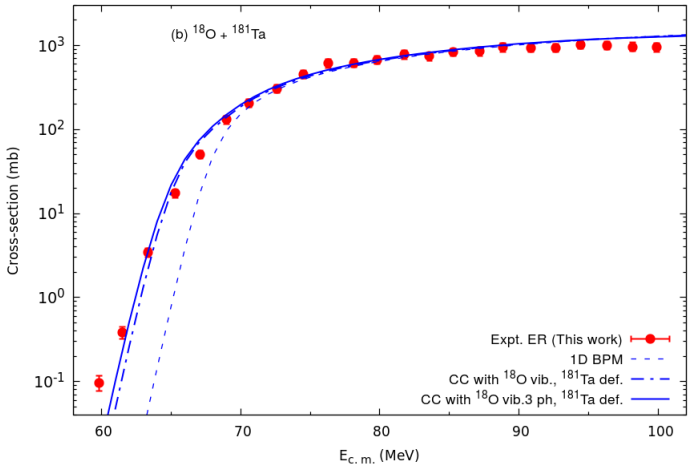

Figure 4.4: Measured ER excitation function as a function of $E_{c.m.}$, for the system $^{18}O+^{181}Ta$ along with CC calculations. Solid line represent CC calculations with coupling and dashed line represents the 1D-BPM (CC calculations without coupling).

4.6 Statistical model calculations

In the present work, we have used HIVAP [3, 10] code to explain the experimental cross-sections above the Coulomb barrier energy region. In HIVAP, barrier passing model incorporated with standard statistical model is used to investigate the nuclear reactions. In the statistical model analysis, ER excitation functions well above the fusion barrier energies are insensitive to the choice of nuclear potential [11]. Among the various input parameters of HIVAP code, the cross-sections calculations are most sensitive to the choice of standard statistical model (SSM) parameters such as, the depth of the fission barrier (B_f) and the ratio of the

level density parameter at the saddle point to that of equilibrium deformation. According to Reisdorf formula [3], the nuclear level density leads to a ratio 1, due to the different nuclear shapes at fission and particle emission state [10]. Shell correction energy which is associated with exponentially varying excitation energy, with a damping constant 18.5 [11] is taken into account while calculating level densities. At energies well above the fusion barrier, excitations functions from statistical model calculation depend mainly on k_f which relates to the fission barrier ($B_f(\ell)$) in agreement with the expression

$$B_f(\ell) = k_f B_f^{LD}(\ell) + \delta W_{gs} \tag{4.3}$$

Here $B_f^{LD}(\ell)$ is the rotating liquid drop model fission barrier [45] and δW_{gs} ground state shell correction, which is calculated as the difference between empirical [46] and liquid drop masses [9]. Same parameter set for potential and k_f with $P_{CN} = 1$ indicates the absence of fusion suppression for systems forming same CN.

For heavy systems, non-compound nuclear fission processes like pre-equilibrium and quasi-fission are possible. Among this, quasi-fission was reported for many heavy ion induced fission reactions especially in the actinide region [47]. Despite extensive reviews on NCNF in pre-actinide as well as actinide regions, it is not clearly understood whether NCNF is always associated with suppression of the formation of ER [48]. Also, there is no clarity regarding the exact experimental boundary between QF and compound nucleus formation. Among the present reactions, ^{16}O+^{181}Ta has α/α_{BG} >1 (absence of NCNF) and ^{18}O+^{181}Ta has $\alpha/\alpha_{BG} < 1$ (presence of NCNF). Therefore, contributions to ER cross-section values from both reactions are expected to be different. However, experimentally both reactions show almost same σ_{ER} values in the

above-barrier region. This indicates the absence of the direct signature of QF (that is the reduction in ER excitation function) in ^{18}O+^{181}Ta with respect to less asymmetric ^{16}O+^{181}Ta reaction.

4.6.1 Statistical model calculations for ^{16}O+^{181}Ta

Statistical model calculations using HIVAP are carried out to look for the presence of non-compound nuclear fission processes. Fig. 4.5 shows the HIVAP calculations and experimental ER cross-sections of ^{16}O+^{181}Ta reaction. In HIVAP calculations at higher energies, default values of parameters are kept as suggested by [3]. HIVAP calculations with P_{CN} and $k_f = 1$ agrees with the fission cross-sections of ^{16}O+^{181}Ta reaction [49, 50] at E_{lab} = 115 and 120 MeV ($E_{c.m.}$ = 105.65 and 110.25 MeV) energies. Calculations performed with k_f = 0.9–1.0 in HIVAP agrees with the experimental fission cross-sections of for ^{16}O+^{181}Ta reaction reported by Videbaek *et al.*[49] and Behera *et al.*[50, 51]. Also, corresponding ER cross-sections from HIVAP calculations reproduced the experimental ER excitation function of ^{16}O+^{181}Ta. The value of k_f in this range (0.9–1.0), which explains all the experimental fission cross-section is taken as the fission barrier scaling factor for ^{16}O+^{181}Ta reaction. Accordingly, we select k_f = 0.95 $\pm$ 0.05 for ^{16}O+^{181}Ta reaction. ER and fission excitation functions with k_f = 0.95 are represented by blue solid and dashed lines respectively in Fig. 4.5. Also, these functions in the said range of k_f (0.9–1.0) are shown as coloured bands. Behera *et al.* [50, 51] performed statistical model calculations with k_f =0.99 and a_f/a_n = 1.012 for ^{16}O+^{181}Ta reaction and reported the absence of quasi-fission in below and above barrier energy points. They could reproduce the fission excitation function and pre-scission neutron multiplicity data with k_f = 0.99, this is in agreement with our observation. ER excitation function of ^{16}O+^{181}Ta

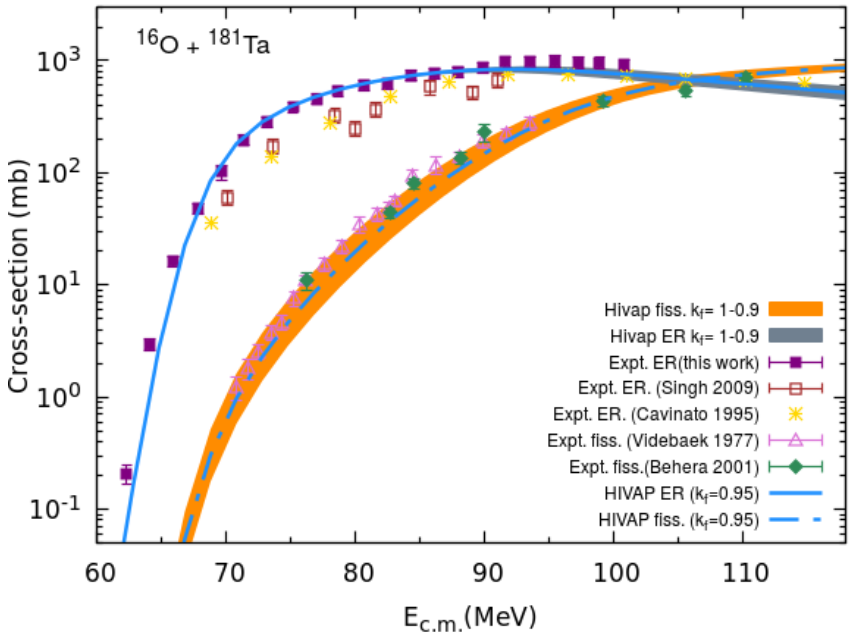

Figure 4.5: Experimental ER and fission excitation functions for ^{16}O+^{181}Ta reaction along with HIVAP calculations. Excitation functions for a range of k_f form 1-0.9 are represented by bands (see text for details).

measured by Singh *et al.* [52] are shown by open squares in Fig. 4.5 along with present data. It is evident that the measurements made by Singh *et al.* [52] show lower values of cross-sections compared to the present measurements. They have used gamma-ray activation technique for measurements of ER excitation functions and included only activities corresponding to 3n, 4n and 5n channels [52]. Cavinato *et al.*[53] also measured cross-sections of fusion without fission for same projectile-target combinations. They limited their measurements to $^{189–193}$Tl, $^{189–193}$Hg, ^{189,191}Pt and excluded ^{194}Tl. ^{194}Tl (3n) channel as per statistical model calculation contributes a major part in the below barrier fusion cross-section. Cavinato's data missed that channel and that may be the reason for deviation of the data from the present measurement.

4.6.2 Statistical model calculations for ^{18}O+^{181}Ta

To bring about the starting point of NCNF reaction in less fissile Tl, fission barrier is fixed by the most asymmetric reactions ^{16}O+^{181}Ta (where $\alpha > \alpha_{BG}$). ^{16}O+^{181}Ta reaction may be put under compound nucleus fission (CNF) type reactions based on the systematics of Banerjee *et al.* [27]. As the two reactions (^{16}O+^{181}Ta, ^{18}O+^{181}Ta) differ only by 2 neutron in the projectile channel we have used the reduction in fission barrier, that is 0.95 for ^{18}O+^{181}Ta with same set of HIVAP parameters. Experimental cross-sections of both reactions are in agreement with SSM calculations with k_f value 0.95±0.05 and $P_{CN} = 1$, which indicates the absence of quasi-fission in both reactions. Coloured bands in Fig. 4.6 shows the theoretical excitation functions of ^{18}O+^{181}Ta in the entire range of k_f.

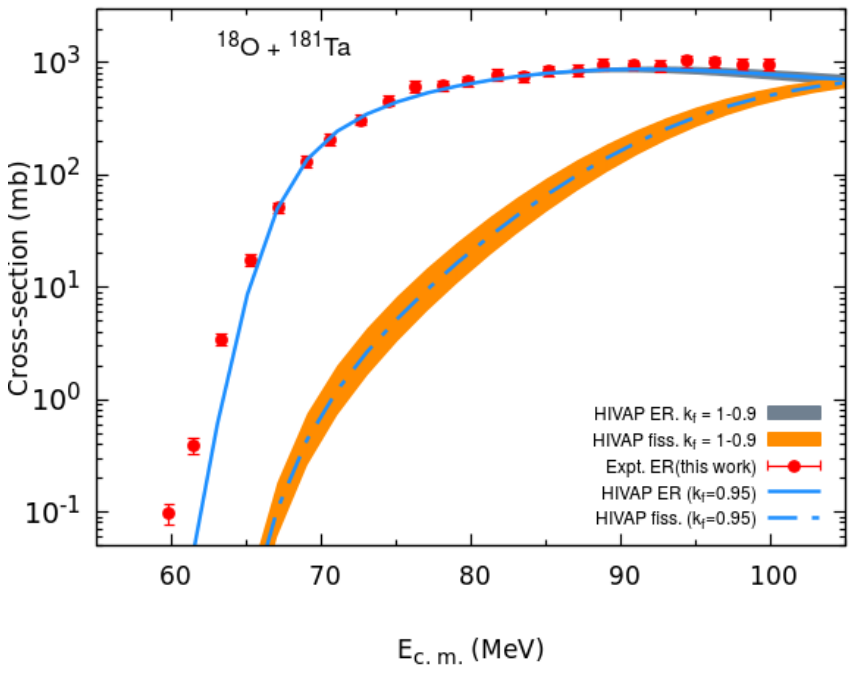

Figure 4.6: Experimental ER and fission excitation functions for ^{18}O+^{181}Ta reaction along with SSM calculations. Excitation functions for a range of k_f are represented by bands (see text for details).

4.6.3 Statistical model calculations for ^{19}F+^{180}Hf

To identify the presence of NCNF reactions in ^{19}F+^{180}Hf, first we tried to reproduce ER excitation function of the same, with the parameter set used to calculate ^{18}O+^{181}Ta reaction. ER excitation functions from HIVAP calculation with k_f from 0.9–1.0 ($P_{CN} = 1$) came within the errors of experimental ER excitation function of ^{19}F+^{180}Hf for all higher energy points as shown in Fig. 4.7. Scaling in P_{CN} is not required to have better agreement with the experimental cross-sections. Some experimental points at around the barrier show small but a considerable deviation from statistical model calculations, which needs further study. $P_{CN} = 1$ in all the three reactions mentioned in this discussion explains the ER excitation function well, irrespective of their entrance channel mass asymmetry. This points to the absence of NCNF reactions in those systems. Any further predictions with smaller k_f value for ^{19}F+^{180}Hf require fission data which unfortunately are not currently available. No fusion suppression effects are found for both reactions as far as P_{CN} values are concerned.

Banerjee *et al.* [27] have shown the variation of P_{CN} with entrance channel mass asymmetry α , charge product $Z_P Z_T$, and compound nucleus fissility χ_{CN}. They found a boundary for χ_{CN} (which is related with $Z_P Z_T$ and α) where P_{CN} starts to deviate from unity in $A \approx 200$ region. The systems ^{16,18}O+^{181}Ta, ^{19}F+^{180}Hf with $Z_P Z_T = 584$, 648 $\eta = 0.8376$, 0.8314, 0.8090 ($\eta = \frac{A_t - A_p}{A_t + A_p}$) and $\chi_{CN} = 0.6936$, 0.6905 respectively lie below this limit of χ_{CN}, indicating absence of NCNF in these reactions. In other words, the calculations using SSM and the systematics reported by Banerjee *et al.* [27] come to the same conclusion regarding the measured reactions.

Also, Singh *et al.* [54] compared the neutron multiplicity data of ^{16}O+^{181}Ta and ^{19}F+^{178}Hf reactions which form the same CN ^{197}Tl. Dissipation strength

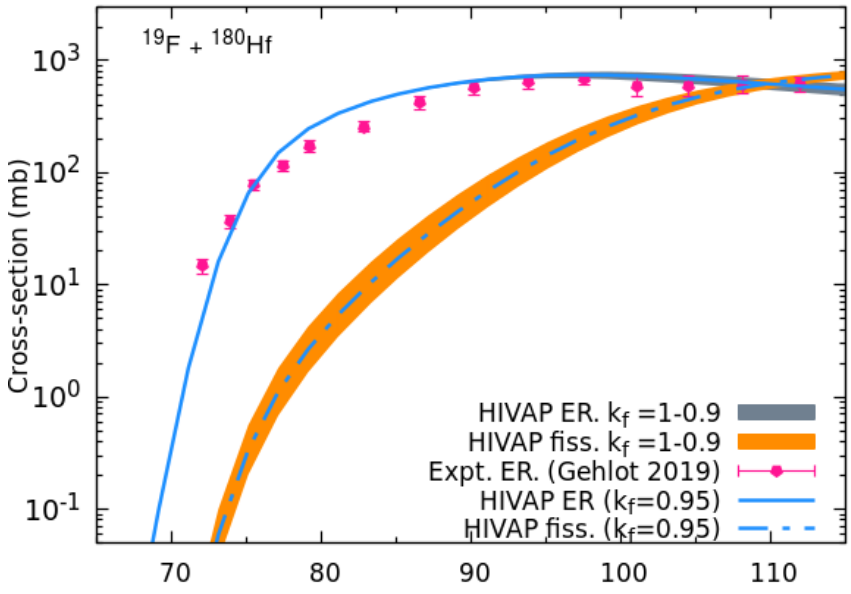

Figure 4.7: Experimental ER and fission excitation functions for ^{19}F+^{180}Hf reaction along with HIVAP calculations. Excitation functions for a range of fission barriers are represented by bands (see text for details).

shows an increase with excitation energy for both systems, but with a larger rate for ^{19}F+^{178}Hf [54]. This larger rate in dissipation strength of ^{19}F+^{178}Hf was attributed to the dependence of excitation functions on entrance channel asymmetry. However, clear association of entrance channel mass asymmetry with QF was not found by Singh *et al.* [54].

4.6.4 General remarks

In order to verify the effects of different projectiles on ^{181}Ta target, we compared the reduced cross-sections of ^{16,18}O+^{181}Ta reactions with that of different projectiles as shown in Fig. 4.8. Reduced cross-section will eliminate the effects of the barrier height and nuclear size.. Here $\tilde{\sigma}_{ER}= \frac{\sigma_{ER}}{\pi R_b^2}$, where R_b [68] the barrier radius. Additional systems which form CN near to Tl nuclei are considered for comparison with the present data, as shown in Fig. 4.8 and 4.9. Most of these

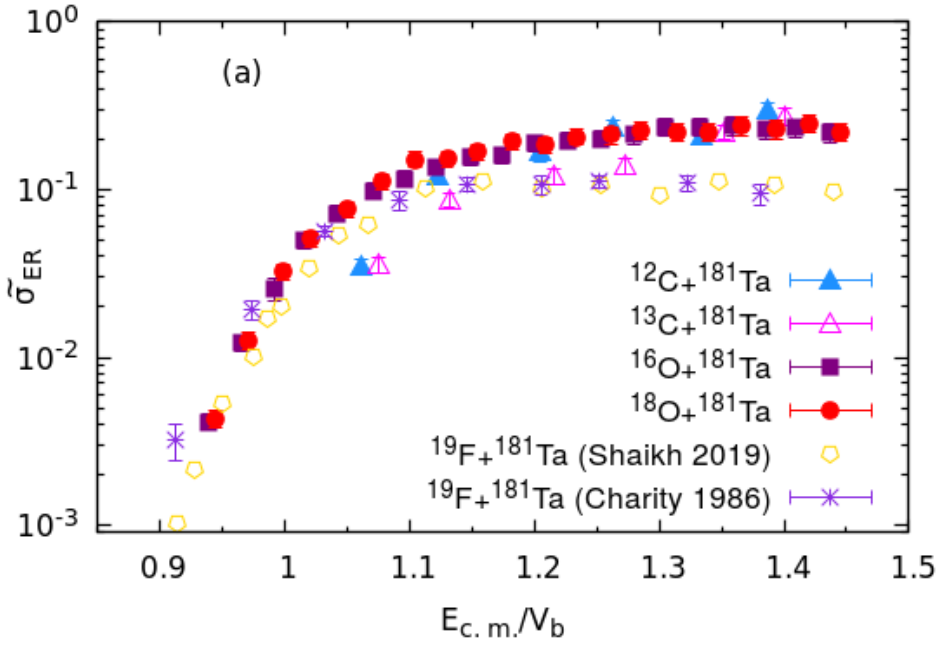

Figure 4.8: Reduced cross-sections as a function of $E_{c.m.}/V_b$ for reactions forming CN in A≈ 200 region. Here reduced cross-section is obtained by dividing absolute cross-section with πR_b^2, where R_b the barrier radius and V_b the Bass barrier. The ER cross-sections of $^{12,13}C+^{181}Ta$ [55], $^{19}F+^{181}Ta$ [39, 56] are obtained from literature.

systems form CN in the pre-actinide ($A \approx 200$) region. Cross-sections of all selected reactions fall almost in the same cross-section region. A small increase is observed in ^{12}C induced reactions, which may be due to the cluster structure properties of ^{12}C [55]. No fusion suppression effect is found in any of the systems except $^{19}F+^{181}Ta$. Small reduction in cross-section of $^{19}F+^{181}Ta$ might be attributed to the presence of non-compound nuclear fission reactions [32].

Further comparison of reduced cross-sections of ^{16}O on various targets is shown in Fig. 4.9. In the selected energy range, all reactions fall in the same energy region of cross-section. From these comparisons, it is evident that the reactions involving less fissile CN do not show any direct entrance channel effect except for certain projectiles such as ^{19}F.

In Table 4.3, we list the systems considered by Sagaidak et al. [6, 11, 19, 31] along with present systems. Also, for reactions forming same CN, fission barrier

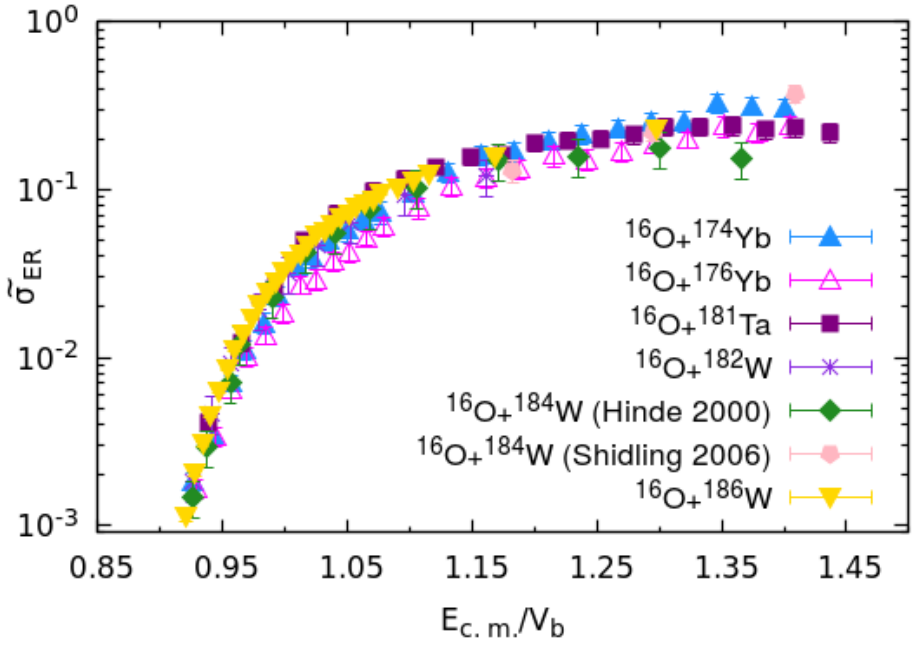

Figure 4.9: Reduced cross-sections as a function of $E_{c.m.}/V_b$ for reactions forming CN in A≈ 200 region. Here reduced cross-section is obtained by dividing absolute cross-section with πR_b^2, where R_b the barrier radius and V_b the Bass barrier. The ER cross-sections of $^{16}O+^{174,176}Yb$ [57], $^{16}O+^{182}W$ [58], $^{16}O+^{184}W$ [58, 59] and $^{16}O+^{186}W$ [60] are obtained from literature.

values are different. P_{CN} of such reactions indicates that this difference in k_f is a specific signature of NCNF reaction. $\frac{\alpha}{\alpha_{BG}}$ value less than one in Table 4.3 predicts the presence of quasi-fission however, their $P_{CN} = 1$ shows the absence of NCNF. Thus α and α_{BG} values can not be used to accurately predict the presence of NCNF in many experimental cases involving less fissile systems.Also, mass asymmetry values do not play much role in fusion suppression in this region.

Reaction	N_{CN}	$Z_P Z_T$	$\frac{\alpha}{\alpha_{BG}}$	k_f	P_{CN}	Ref.
$^{12}C+^{208}Pb\rightarrow^{220}Ra$	132	492	1.0334	0.85 [19]	1	[19]
$^{12}C+^{206}Pb\rightarrow^{218}Ra$	130	492	1.0307	0.82 [19]	1	[19]
$^{19}F+^{197}Au\rightarrow^{216}Ra$	128	711	0.9528	[0.78,0.82] [19]	[1,0.65]	[61]
$^{12}C+^{204}Pb\rightarrow^{216}Ra$	128	492	1.0277	0.82 [19]	1	[19]
$^{19}F+^{198}Pt\rightarrow^{217}Fr$	130	702	0.9613	[0.78,0.85] [21]	[1,0.73]	[62]
$^{18}O+^{197}Au\rightarrow^{215}Fr$	128	632	0.9687	0.85 [6]	1	[6]
$^{19}F+^{194}Pt\rightarrow^{213}Fr$	126	702	0.9542	[0.78,0.82] [21]	[1,0.75]	[62]
$^{16}O+^{197}Au\rightarrow^{213}Fr$	126	632	0.9870	0.82 [6]	1	[63]
$^{18}O+^{192}Os\rightarrow^{210}Po$	126	608	0.9820	0.92 [11]	1	[64]
$^{16}O+^{192}Os\rightarrow^{208}Po$	124	608	1.0009	0.88 [11]	1	[65]
$^{18}O+^{188}Os\rightarrow^{206}Po$	122	608	0.9742	0.82 [11]	1	[65]
$^{16}O+^{188}Os\rightarrow^{204}Po$	120	608	0.9934	0.77 [11]	1	[65]
$^{16}O+^{186}W\rightarrow^{202}Pb$	120	592	1.0065	0.85 [31]	1	[66]
$^{19}F+^{181}Ta\rightarrow^{200}Pb$	118	657	0.9666	0.85 [31]	1	[56]
$^{16}O+^{184}W\rightarrow^{200}Pb$	118	592	1.0024	0.85 [31]	1	[67]
$^{19}F+^{180}Hf\rightarrow^{199}Tl$	118	648	0.9731	0.95[This work]	1	[33]
$^{18}O+^{181}Ta\rightarrow^{199}Tl$	118	584	0.9852	0.95	1	[This work]
$^{16}O+^{181}Ta\rightarrow^{197}Tl$	116	584	1.0051	0.95	1	[This work]

Table 4.3: Lists of reactions considered in $A \approx 200$ region and their charge product $Z_P Z_T$, neutron number of compound nuclei N_{CN}, fission barrier scaling factor k_f, ratio of mass asymmetry values and its critical value at BG point $\frac{\alpha}{\alpha_{BG}}$ [28] and fusion probability P_{CN} are mentioned in table. Two k_f and P_{CN} corresponds to variations in those numbers with different fits.

Bibliography

[1] M. Dasgupta, D. J. Hinde, N. Rowley, and A. M. Stefanini, Annu. Rev. Nucl. Part. Sci. **48**, 401 (1998).

[2] M. Dasgupta, D. J. Hinde, A. Diaz-Torres, B. Bouriquet, C. I. Low, G. J. Milburn, and J. O. Newton, Phys. Rev. Lett. **99**, 192701 (2007).

[3] W. Reisdorf and M. Schädel, Z. Phy. A. **343**, 47 (1992).

[4] R. du Rietz, D. J. Hinde, M. Dasgupta, R. G. Thomas, L. R. Gasques, M. Evers, N. Lobanov, and A. Wakhle, Phys. Rev. Lett. **106**, 052701 (2011).

[5] Hinde, D. J., du Rietz, R, and Dasgupta, M., EPJ Web of Conferences **17**, 04001 (2011).

[6] L. Corradi, B. R. Behera, E. Fioretto, A. Gadea, A. Latina, A. M. Stefanini,

S. Szilner, M. Trotta, Y. Wu, S. Beghini, G. Montagnoli, F. Scarlassara, R. N. Sagaidak, S. N. Atutov, B. Mai, G. Stancari, L. Tomassetti, E. Mariotti, A. Khanbekyan, and S. Veronesi, Phys. Rev. C **71**, 014609 (2005).

[7] J. Gehlot, A. M. Vinodkumar, N. Madhavan, S. Nath, A. Jhingan, T. Varughese, T. Banerjee, A. Shamlath, P. V. Laveen, M. Shareef, P. Jisha, P. S. Devi, G. N. Jyothi, M. M. Hosamani, I. Mazumdar, V. I. Chepigin, M. L. Chelnokov, A. V. Yeremin, A. K. Sinha, and B. R. S. Babu, Phys. Rev. C **99**, 034615 (2019).

[8] S. Cohen, F. Plasil, and W. J. Swiatecki, Ann. Phys. (NY) **82**, 557 (1974).

[9] W. D. Myers and W. J. Swiatecki, Ark. Fys. **36**, 343 (1967).

[10] W. Reisdorf, Z. Phys. A. **300**, 227 (1981).

[11] R. N. Sagaidak, , and A. N. Andreyev, Phys. Rev. C **79**, 054613 (2009).

[12] K. Banerjee, D. J. Hinde, M. Dasgupta, E. C. Simpson, D. Y. Jeung, C. Simenel, B. M. A. Swinton-Bland, E. Williams, I. P. Carter, K. J. Cook, H. M. David, C. E. Düllmann, J. Khuyagbaatar, B. Kindler, B. Lommel, E. Prasad, C. Sengupta, J. F. Smith, K. Vo-Phuoc, J. Walshe, and A. Yakushev, Phys. Rev. Lett. **122**, 232503 (2019).

[13] R. S. Naik, W. Loveland, P. H. Sprunger, A. M. Vinodkumar, D. Peterson, C. L. Jiang, S. Zhu, X. Tang, E. F. Moore, and P. Chowdhury, Phys. Rev. C **76**, 054604 (2007).

[14] V. Zagrebaev and W. Greiner, Phys. Rev. C **78**, 034610 (2008).

[15] W. Loveland, Journal of Physics: Conference Series **420**, 012004 (2013).

[16] K. Hagino, Phys. Rev. C **98**, 014607 (2018).

[17] A. C. Berriman, D. J. Hinde, M. Dasgupta, C. R. Morton, R. D. Butt, and J. O. Newton, Nature **413** (2001).

[18] D. J. Hinde, A. C. Berriman, R. D. Butt, M. Dasgupta, I. I. Gontchar, C. R. Morton, A. Mukherjee, and J. O. Newton, J. Nucl. Radiochem. Sci **3**, 31 (2002).

[19] R. N. Sagaidak, G. N. Kniajeva, I. M. Itkis, M. G. Itkis, N. A. Kondratiev, E. M. Kozulin, I. V. Pokrovsky, A. I. Svirikhin, V. M. Voskressensky, A. V. Yeremin, L. Corradi, A. Gadea, A. Latina, A. M. Stefanini, S. Szilner, M. Trotta, A. M. Vinodkumar, S. Beghini, G. Montagnoli, F. Scarlassara, D. Ackermann, F. Hanappe, N. Rowley, and L. Stuttg, Phys. Rev. C **68**, 014603 (2003).

[20] D. J. Hinde, M. Dasgupta, and A. Mukherjee, Phys. Rev. Lett. **89**, 282701 (2002).

[21] R. N. Sagaidak, A. Y. Chizhov, I. M. Itkis, M. G. Itkis, G. N. Kniajeva, N. A. Kondratiev, E. M. Kozulin, I. V. Pokrovsky, L. Corradi, E. Fioretto, A. Gadea, A. Latina, A. M. Stefanini, S. Beghini, G. Montagnoli, F. Scarlassara, M. Trotta, and S. Szilner, AIP Conf. Proc. **853**, 114 (2006).

[22] A. Shamlath, M. Shareef, E. Prasad, P. Sugathan, R. G. Thomas, A. Jhingan, S. Appannababu, A. K. Nasirov, A. M. Vinodkumar, K. M. Varier, C. Yadav, B. R. S. Babu, S. Nath, G. Mohanto, I. Mukul, D. Singh, and S. Kailas, Nucl. Phys. A **945**, 67 (2016).

[23] A. Shamlath, E. Prasad, N. Madhavan, P. V. Laveen, J. Gehlot, A. K. Nasirov, G. Giardina, G. Mandaglio, S. Nath, T. Banerjee, A. M. Vinodkumar, M. Shareef, A. Jhingan, T. Varughese, D. Kumar, P. S. Devi,

Khushboo, P. Jisha, N. Kumar, M. M. Hosamani, and S. Kailas, Phys. Rev. C **95**, 034610 (2017).

[24] R. Rafiei, R. G. Thomas, D. J. Hinde, M. Dasgupta, C. R. Morton, L. R. Gasques, M. L. Brown, and M. D. Rodriguez, Phys. Rev. C **77**, 024606 (2008).

[25] G. N. Knyazheva, E. M. Kozulin, R. N. Sagaidak, A. Y. Chizhov, M. G. Itkis, N. A. Kondratiev, V. M. Voskressensky, A. M. Stefanini, B. R. Behera, L. Corradi, E. Fioretto, A. Gadea, A. Latina, S. Szilner, M. Trotta, S. Beghini, G. Montagnoli, F. Scarlassara, F. Haas, N. Rowley, P. R. S. Gomes, and A. S. d. Toledo, Phys. Rev. C **75**, 064602 (2007).

[26] C. Schmitt, K. Mazurek, and P. N. Nadtochy, Phys. Rev. C **100**, 064606 (2019).

[27] T. Banerjee, S. Nath, and S. Pal, Phys. Rev. C **91**, 034619 (2015).

[28] U. L. Businaro and S. Gallone, Nuovo Cimento **5**, 315 (1957).

[29] P. Sharma, B. R. Behera, R. Mahajan, M. Thakur, G. Kaur, K. Kapoor, K. Rani, N. Madhavan, S. Nath, J. Gehlot, R. Dubey, I. Mazumdar, S. M. Patel, M. Dhibar, M. M. Hosamani, Khushboo, N. Kumar, A. Shamlath, G. Mohanto, and S. Pal, Phys. Rev. C **96**, 034613 (2017).

[30] V. Singh, B. R. Behera, M. Kaur, A. Kumar, K. P. Singh, N. Madhavan, S. Nath, J. Gehlot, G. Mohanto, A. Jhingan, I. Mukul, T. Varughese, J. Sadhukhan, S. Pal, S. Goyal, A. Saxena, S. Santra, and S. Kailas, Phys. Rev. C **89**, 024609 (2014).

[31] R. Sagaidak, G. Kniajeva, I. Itkis, M. G. Itkis, N. A. Kondratiev, E. M. Kozulin, I. V. Pokrovsky, V. M. Voskressensky, A. Yeremin, L. Corradi,

A. Gadea, A. Latina, A. Stefanini, S. Szilner, M. Trotta, A. M. Vinodkumar, S. Beghini, G. Montagnoli, F. Scarlassara, and N. Rowley, JINR-Reports (2003).

[32] A. Nasirov, G. Mandaglio, M. Manganaro, A. Muminov, G. Fazio, and G. Giardina, Phys. Lett. B **686**, 72 (2010).

[33] J. Gehlot, S. Nath, T. Banerjee, I. Mukul, R. Dubey, A. Shamlath, P. V. Laveen, M. Shareef, M. M. Shaikh, A. Jhingan, N. Madhavan, T. Rajbongshi, P. Jisha, and S. Pal, Phys. Rev. C **99**, 061601 (2019).

[34] A. Sinha, N. Madhavan, J. Das, P. Sugathan, D. Kataria, A. Patro, and G. Mehta, Nucl. Instrum. Methods Phys. Res. A **339**, 543 (1994).

[35] V. I. Zagrebaev, A. S. Denikin, A. V. Karpov, A. P. Alekseev, M. A. Naumenko, V. A. Rachkov, V. V. Samarin, and V. V. Saiko, NRV web knowledge base on low-energy nuclear physics, `http://nrv.jinr.ru/` (1999).

[36] K. Hagino and N. Takigawa, Prog. Theor. Phys. **128**, 1061 (2012).

[37] K. Hagino, N. Rowley, and A. Kruppa, Comput. Phys. Commun. **123**, 143 (1999).

[38] S. Ramen, C. W. Nestor, and P. Tikkanen, At. Data Nucl. Data Tables **78**, 1 (2001).

[39] M. M. Shaikh, S. Nath, J. Gehlot, T. Banerjee, I. Mukul, R. Dubey, A. Shamlath, P. V. Laveen, M. Shareef, A. Jhingan, N. Madhavan, T. Rajbongshi, P. Jisha, G. N. Jyothi, A. Tejaswi, R. N. Sahoo, and A. Rani, J. Phys. G: Nucl. Part. Phys. **45**, 095103 (2018).

[40] P. Möller, A. J. Sierk, T. Ichikawa, and H. Sagawa, At. Data Nucl. Data Tables **109-110**, 1 (2016).

[41] T. Kibedi and R. Spear, At. Data Nucl. Data Tables **80**, 35 (2002).

[42] M. Firihu, K. Hagino, and N. Takigawa, AIP Conf. Proc. **853** (2006).

[43] K. E. Zyromski, W. Loveland, G. A. Souliotis, D. J. Morrissey, C. F. Powell, O. Batenkov, K. Aleklett, R. Yanez, and I. Forsberg, Phys. Rev. C **63**, 024615 (2001).

[44] K. Hagino, N. Takigawa, M. Dasgupta, D. J. Hinde, and J. R. Leigh, Phys. Rev. Lett. **79**, 2014 (1997).

[45] A. J. Sierk, Phys. Rev. Lett. **55**, 582 (1985).

[46] G. Audi and A. H. Wapstra, Nucl. Phys. A **595**, 409 (1995).

[47] S. Kailas, J. Phys. G: Nucl. Part. Phys. **23**, 1227 (1997).

[48] R. Tripathi, S. Sodaye, and K. Sudarshan, Pramana **85**, 315 (2015).

[49] F. Videbæk, R. B. Goldstein, L. Grodzins, S. G. Steadman, T. A. Belote, and J. D. Garrett, Phys. Rev. C **15**, 954 (1977).

[50] B. R. Behera, S. Roy, P. Basu, M. K. Sharan, S. Jena, M. Satpathy, M. L. Chatter Jee, and S. K. Datta, Pramana **57**, 199 (2001).

[51] B. R. Behera, S. Jena, M. Satpathy, S. Roy, P. Basu, M. K. Sharan, M. L. Chatterjee, S. Kailas, K. Mahata, and Datta, Phys. Rev. C **66**, 047602 (2002).

[52] D. P. Singh, Unnati, P. P. Singh, A. Yadav, M. K. Sharma, B. P. Singh, K. S. Golda, R. Kumar, A. K. Sinha, and R. Prasad, Phys. Rev. C **80**, 014601 (2009).

[53] M. Cavinato, E. Fabrici, E. Gadioli, E. Gadioli Erba, P. Vergani, M. Crippa, G. Colombo, I. Redaelli, and M. Ripamonti, Phys. Rev. C **52**, 2577 (1995).

[54] H. Singh, A. Kumar, B. R. Behera, I. M. Govil, K. S. Golda, P. Kumar, A. Jhingan, R. P. Singh, P. Sugathan, M. B. Chatterjee, S. K. Datta, Ranjeet, S. Pal, and G. Viesti, Phys. Rev. C **76**, 044610 (2007).

[55] K. S. Babu, R. Tripathi, K. Sudarshan, B. D. Shrivastava, A. Goswami, and B. S. Tomar, J. Phys. G: Nucl. Part. Phys. **29**, 1011 (2003).

[56] R. J. Charity, J. R. Leigh, J. J. M. Bokhorst, A. Chatterjee, G. S. Foote, D. J. Hinde, J. O. Newton, S. Ogaza, and D. Ward, Nucl. Phys. A **457**, 441 (1986).

[57] T. Rajbongshi, K. Kalita, S. Nath, J. Gehlot, T. Banerjee, I. Mukul, R. Dubey, N. Madhavan, C. J. Lin, A. Shamlath, P. V. Laveen, M. Shareef, N. Kumar, P. Jisha, and P. Sharma, Phys. Rev. C **93**, 054622 (2016).

[58] D. J. Hinde, W. Pan, A. C. Berriman, R. D. Butt, M. Dasgupta, C. R. Morton, and J. O. Newton, Phys. Rev. C **62**, 024615 (2000).

[59] P. D. Shidling, N. M. Badiger, S. Nath, R. Kumar, A. Jhingan, R. P. Singh, P. Sugathan, S. Muralithar, N. Madhavan, A. K. Sinha, S. Pal, S. Kailas, S. Verma, K. Kalita, S. Mandal, R. Singh, B. R. Behera, K. M. Varier, and M. C. Radhakrishna, Phys. Rev. C **74**, 064603 (2006).

[60] M. Trotta, A. Stefanini, and S. B. et. al., Eur. J. Phys., A 25,615 (2005).

[61] R. Tripathi, K. Sudarshan, S. Sodaye, A. V. R. Reddy, K. Mahata, and A. Goswami, Phys. Rev. C **71**, 044616 (2005).

[62] K. Mahata, S. Kailas, A. Shrivastava, A. Chatterjee, P. Singh, S. Santra, and B. S. Tomar, Phys. Rev. C **65**, 034613 (2002).

[63] D. J. Hinde, R. J. Charity, G. S. Foote, J. R. Leigh, J. O. Newton, S. Ogaza, and A. Chattejee, Nucl. Phys. A **452**, 550 (1986).

[64] D. J. Hinde, R. J. Charity, G. S. Foote, J. R. Leigh, J. O. Newton, S. Ogaza, and A. Chattejee, Nucl. Phys. A **452**, 550 (1986).

[65] J. van der Plicht, H. C. Britt, M. M. Fowler, Z. Fraenkel, A. Gavron, J. B. Wilhelmy, F. Plasil, T. C. Awes, and G. R. Young, Phys. Rev. C **28**, 2022 (1983).

[66] R. C. Lemmon, J. R. Leigh, J. X. Wei, C. R. Morton, D. J. Hinde, J. O. Newton, J. C. Mein, M. Dasgupta, and N. Rowley, Phys. Lett. B **316**, 32 (1993).

[67] J. R. Leigh, J. J. M. Bokhorst, D. J. Hinde, and J. O. Newton, J. Phys. G: Nucl. Part. Phys. **14**, L55 (1988).

[68] NRV nuclear transfer and inelastic reactions: Grazing code, `http://nrv.jinr.ru/nrv/webnrv/grazing/` (2005).

Chapter 5

ER measurements, analysis and results for ^{18}O+^{182,184,186}W reactions

5.1 Introduction

In heavy-ion fusion, a significant amount of enhancement was observed in the below-barrier fusion cross-sections in comparison with 1D-BPM [1–5]. Fusion enhancement is affected by the structure of colliding nuclei [6–11] and inclusion of neutron transfer channels [12–18] in the coupled channel (CC) calculations. Incorporating the above mentioned aspects in couplings calculations, reduces the fusion barrier and leads to enhanced sub-barrier fusion cross-sections [19]. Existing theoretical models [20–22] have already identified the role of nuclear deformation and vibration in the enhancement of experimental sub-barrier fusion cross-sections. However, further understanding of the role of neutron transfer channels in fusion enhancement is required.

The effect of the positive Q-value of neutron transfer (PQNT) on the sub-barrier fusion enhancement was first observed by Beckerman *et al.* [23] in

^{58}Ni+^{64}Ni system. Broglia *et al.*[17, 24] further explained such enhancement with positive Q-value transfer channels. Studies on ^{40}Ca + ^{44,48}Ca added evidences for the fusion enhancement in below-barrier fusion cross-sections due to PQNT[25]. Several experimental studies attributed the enhancement in fusion cross-sections to the PQNT channel [13, 15, 16]. Experimental studies on systems like ^{32}Si+^{100}Mo [26], ^{40}Ca+^{90,96}Zr [27, 28], ^{32}Si+^{110}Pd [29], ^{40}Ca+^{124,132}Sn [15], ^{40}Ca+^{70}Zn [30] etc. confirmed the PQNT channel effects. However, many measurements like ^{18}O+^{118}Sn [31], ^{17}O+^{144}Sm [6], ^{58,64}Ni+^{130}Te [32], ^{58,64}Ni+^{132}Sn [32], ^{60,64}Ni+^{100}Mo [33], ^{16,18}O+^{76,74}Ge [34], etc. do not show a significant fusion enhancement in the below-barrier energy region even with a PQNT channel.

The inclusion of PQNT in CC calculations explained the fusion enhancement in many cases; however, its presence alone is not sufficient to explain the enhanced cross-sections [32–34]. The goal of many of the systematics and theoretical studies was to figure out what was causing the fusion enhancement. To find the influence of neutron transfer on fusion excitation function Jiang *et al.* [35] carried out a systematic study, and their results show that significant enhancement was possible in systems with neutron-poor projectiles and neutron-rich targets. [36] pointed out that the PQNT channel significantly influences sub-barrier fusion when the system has large positive Q-values for neutron transfer and the coupling to the collective states is weak at sub-barrier energy. Further, the systematic investigations of Zhang *et al.* [37] on systems with PQNT observed that after neutron transfer, fusion enhancement occurs when the deformation of interacting nuclei increases and the mass asymmetry of systems decreases.The deformation of nuclei having a similar effect on transfer coupling can be seen elsewhere [38–40].

The relevance of the neutron transfer with positive Q-values on nuclear fu-

sion lies in the insensitive nature of the Coulomb barrier to the neutrons. For radioactive and weakly bound nuclei, couplings to neutron transfer play a significant role in enhancing fusion at below-barrier energies. Such a large influence of neutron transfer is most likely due to the extended wave-functions of the loosely bound neutrons [14, 41]. Studies on weakly bound nuclei showed that the coupling to breakup channels enhances cross sections for the complete fusion at energies below the Coulomb barrier, while it reduces them at energies above [42, 43]. However, determining the involvement of weakly bound nucleons in sub-barrier fusion is difficult due to the difficulty of simultaneously considering decay channels as well as nucleon transfer in complete fusion [41, 44].

Even with several theoretical works [20, 21, 45–47] in the area of transfer and fusion, a detailed understanding of PQNT on sub-barrier fusion is missing [48]. This lack of a comprehensive idea on transfer is due to the difficulties in integrating these channels into theoretical models. There is not sufficient experimental data to get a clear understanding of this aspect.

In the present work, for evaporation residue measurements we have selected ^{18}O+^{182,184,186}W reactions, which have a positive Q-value for 2n-transfer. The goal of this study is to compare the fusion cross-sections of these reactions to those of ^{16}O+^{182,184,186}W reactions [49–51] which have negative Q-value for 2n-transfer. Even though the compound nucleus (CN) formed in ^{18}O+^{182,184,186}W reactions are fissile, the fission cross-section in the below-barrier energy region is negligible. Thus, there will be no undesired bias when comparing the fusion cross-sections of ^{16}O+^{182,184,186}W with evaporation residue (ER) excitation functions of ^{18}O+^{182,184,186}W in the below-barrier energy regions. In the case of ^{18}O induced reactions after 2n-transfer, the target-like nuclei show a change in deformation. Also, different observations by Rachkov *et al.* [36] showed that for colliding nuclei with a magic proton or neutron number, neutron rearrangement would

play a significant role in fusion enhancement.

Even with a high positive transfer Q-value, fusion excitation functions of ^{18}O on different isotopes of Sn do not show enhancement in the sub-barrier energy range [39, 40, 52]. However, recent work of Deb *et al.* [53] shows an increase in the below-barrier fusion cross-sections for ^{18}O+ ^{116}Sn due to the PQNT effects. Like Sn isotopes, ^{182,184,186}W, which exhibit a more significant deformation, will be an ideal selection to study the role of the PQNT channel on fusion enhancement in the heavy mass region. The majority of ^{18}O induced reactions have negative Q_{1n} transfer and positive Q_{2n} transfer, which prevents a sequential transfer and favors a pair transfer. Esbensen *et al.*[25] attributed a strong pair-transfer channel with a positive Q-value to fusion enhancement in below-barrier cross-sections. Due to the rarity of ^{18}O-induced reactions in heavy-ion fusion, ^{18}O+^{182,184,186}W will be a good candidate for studying the neutron transfer effect in heavy-ion fusion enhancement in the below the barrier energy regions.

5.2 Experimental details

As given in chapter 4, this experiment was also performed using the 15 UD Pelletron accelerator and HIRA [54] facility of the Inter-University Accelerator Centre (IUAC), New Delhi, which was kept at zero degrees to the beam direction with a 10 mSr entrance aperture. A pulsed beam of ^{18}O with 4 μs pulse separation bombarded the isotopically enriched targets of ^{182}W (91.6%), ^{184}W (95.2%) and ^{186}W (94%) with an approximate thickness of 70 μg/cm^2, 300 μg/cm^2, and 100 μg/cm^2 respectively. ER excitation functions were measured at laboratory beam energies 68 MeV to 104 MeV (10% below to 35% above the fusion barrier) in 2-4 MeV energy steps.

Two silicon surface barrier detectors (SSBD) of active area 50 mm^2 each with a collimator diameter of 1 mm were placed at a distance of 90 mm from the target

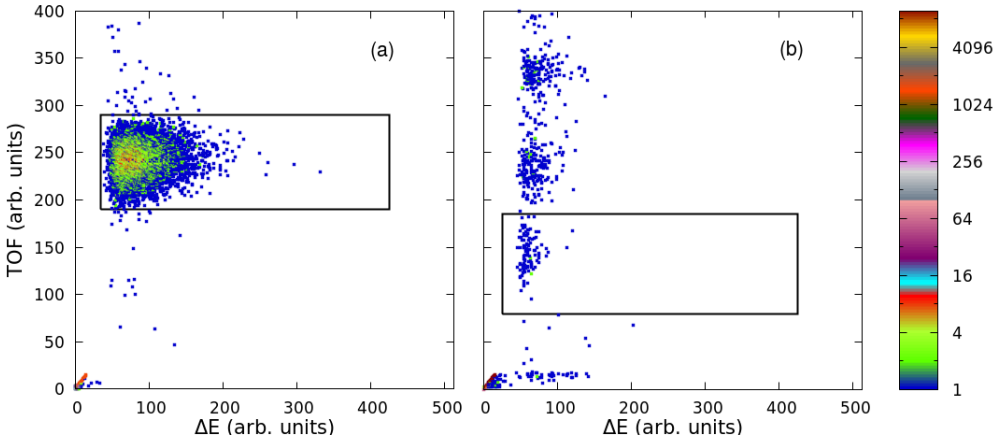

Figure 5.1: Scatter plot between ΔE and TOF of the events recorded at the focal plane of HIRA for ^{18}O+ ^{182}W reaction at energies 100.0 and 70.0 MeV E_{lab} are shown in panel (a) and (b) respectively.

in the target chamber. SSBD was placed at an angle of $\pm$ 15° to beam direction for normalization of ER cross-sections. A carbon foil with a thickness of 40 μg/cm^2 was placed 10 cm downstream from the target for equilibration of the charge states of ERs. A multi-wire proportional counter (MWPC) of active area 150×50 mm^2 was placed at the focal plane (FP) of HIRA to detect the ERs. A time of flight (TOF) was set up between the anode signal of MWPC and the RF signal to separate the scattered beam-like particles from ERs. Data acquisition was carried out using a CAMAC-based system, and analysis was performed with the software CANDLE [55]. Scatter plots for the reactions ^{18}O+^{182,184,186}W at E_{lab} = 100 MeV and 70 MeV for each targets are shown in Fig. 5.1, 5.2, 5.3 respectively.

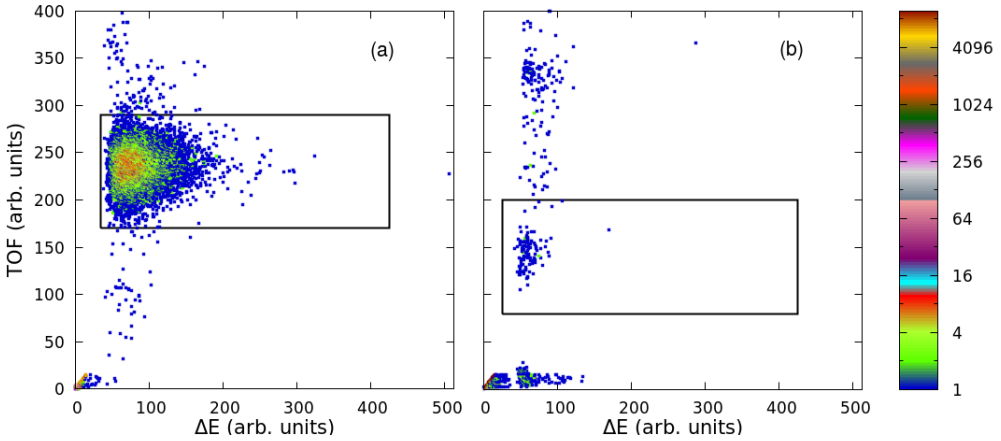

Figure 5.2: Scatter plot between ΔE and TOF of the events recorded at the focal plane of HIRA for ^{18}O+ ^{184}W reaction at energies 100.0 and 70.0 MeV E_{lab} are shown in panel (a) and (b) respectively.

5.3 Data analysis

The total ER cross-section were obtained using

$$\sigma_{ER} = \frac{Y_{ER}}{Y_{norm}} \left(\frac{d\sigma}{d\Omega}\right)_{Ruth} \Omega_{norm} \left(\frac{1}{\bar{\epsilon}_{HIRA}}\right) \tag{5.1}$$

where Y_{ER} is the number of ERs detected at the FP of the HIRA, Y_{norm} is the number of elastically scattered projectile like particles detected by the normalization detectors, $(\frac{d\sigma}{d\Omega})_{Ruth}$ is the differential Rutherford-scattering cross-section in the laboratory system, Ω_{norm} is the solid angle subtended by the normalization detectors, and $\bar{\epsilon}_{HIRA}$ is the average ER transmission efficiency of HIRA. The significant challenges experienced while extracting σ_{ER} for the first set of experiments were relent for this set of experiment also. Discussions on the determination of efficiency factor of HIRA is given in Section 4.3

Unambiguous identification of ER at the FP detector was achieved by simultaneously measuring energy loss, ΔE (measured at the cathode of MWPC), and TOF of the ERs. The data acquisition steps are similar in both sets of experiments. TOF provides a clear separation of ERs from projectile-like back-

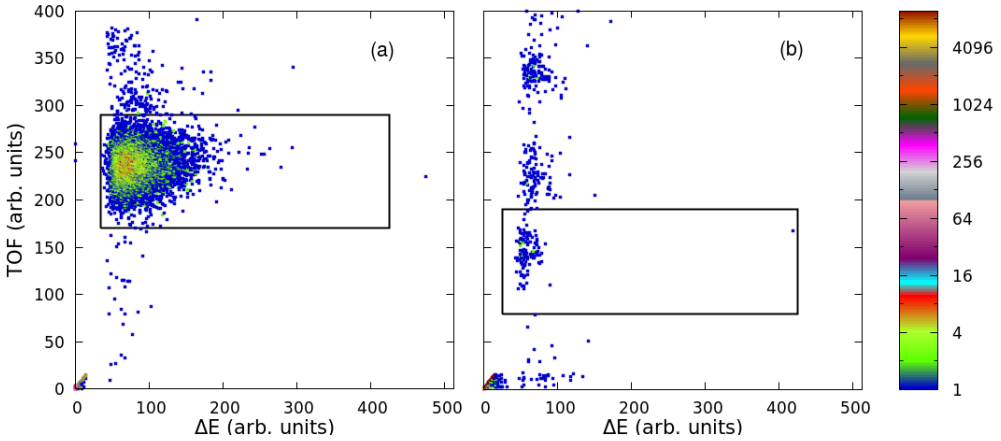

Figure 5.3: Scatter plot between ΔE and TOF of the events recorded at the focal plane of HIRA for ^{18}O+ ^{186}W reaction at energies 100.0 and 70.0 MeV E_{lab} are shown in panel (a) and (b) respectively.

ground events. The scatter plots of ΔE versus TOF at E_{lab} = 100.0 MeV and 70 MeV for the reaction ^{18}O+^{182,184,186}W are shown in Fig. 5.1, 5.1 and 5.1. The relative strength of background events on the HIRA FP detector, although negligible in most cases, was observed to increase gradually with a decrease in E_{lab} in below-barrier energies [56]. In the present investigations, we obtained adequate distinction between ERs and background events across the entire range of E_{lab}. The measured ER cross-sections of ^{18}O+^{182,184,186}W reactions as a function of projectile energies in the center of mass frame ($E_{c.m.}$) and laboratory frames (E_{lab}) are listed in Table 5.1, 5.2, 5.3. The sum of statistical and systematic errors is quoted as the total error in the measurement. The overall error was estimated to be $\leq$20 % below the barrier energies. In the total error, the major part is from ϵ_{HIRA} ($\approx$ 10 %). Statistical model calculations [57] of ^{18}O+^{182,184,186}W revealed that the calculated fission cross-sections are negligibly small in the measured energy range. For ^{18}O+^{182,184,186}W reactions, the estimated fission cross-sections using PACE4 was found to be 5%, 3% and 2% respectively at the highest energies where measurements were carried out. Hence, ER cross-sections in the energy range of measurements were considered as σ_{fus} in the present study.

E_{lab} (MeV)	$E_{c.m.}$ (MeV)	E^* (MeV)	ϵ_{HIRA} (%)	σ_{ER} (mb)
104.0	94.52	71.74	1.11	1081.14±152.4
100.0	90.87	68.09	1.57	1094.24±151.13
96.0	87.23	64.45	1.66	786.35 ±285.05
92.0	83.58	60.8	1.94	778.96±130.35
88.0	79.94	57.16	1.59	590.68±81.84
84.0	76.30	53.52	1.22	368.25±59.64
80.0	72.65	49.87	1.6	194.01±35.37
78.0	70.83	48.05	1.87	120.48 ±24.04
76.0	69.01	46.23	2.1	55.38±7.89
74.0	67.19	44.41	2.01	26.25±3.81
72.0	65.37	42.59	2.04	9.03±1.4
70.0	63.55	40.77	1.92	1.53±0.27
68.0	61.73	38.95	1.75	0.23±0.08

Table 5.1: Measured evaporation residue cross-sections (σ_{ER}) for $^{18}O+^{182}W$ reaction. Here the sum of statistical and systematic errors are quoted as the total error in the measurement.

E_{lab} (MeV)	$E_{c.m.}$ (MeV)	E^* (MeV)	$\bar{\epsilon}_{HIRA}$ (%)	σ_{ER} (mb)
104.0	94.43	73.88	0.6945	766.53 ±134.34
100.0	90.78	70.23	0.6091	887.32 ±171.04
96.0	87.12	66.57	0.8072	932.69± 195.39
92.0	83.48	62.93	0.5772	815.86± 168.28
88.0	79.83	59.28	0.458	705.53± 129.93
84.0	76.17	55.62	0.5152	369.82± 69.93
80.0	72.52	51.97	0.6564	182.25± 30.46
78.0	70.69	50.14	0.6258	129.88± 22.75
76.0	68.87	48.32	0.5955	68.45± 11.23
74.0	67.04	46.49	0.572	32.26 ±3.92
72.0	65.22	44.67	0.5703	7.17± 1.45
70.0	63.38	42.83	0.6214	2.55± 0.53

Table 5.2: Measured evaporation residue cross-sections (σ_{ER}) for $^{18}O+^{184}W$ reaction. Tabulated energies are in center of mass systems. Here the sum of statistical and systematic errors are quoted as the total error in the measurement.

E_{lab} (MeV)	$E_{c.m.}$ (MeV)	E^* (MeV)	$\overline{\epsilon}_{HIRA}$ (%)	σ_{ER} (mb)
104	94.67	76.49	1.2191	767.16±91.21
100	91.02	72.84	1.1485	673.16±78.51
96	87.37	69.18	1.0832	723.34±87.62
92	83.72	65.53	1.1243	656.08±77.8
88	80.07	61.88	1.0591	606.68±71.25
84	76.41	58.23	0.9174	484.16±54.34
80	72.76	54.58	1.4005	215.57±25.2
78	70.93	52.75	1.4157	164.42±18.77
76	69.11	50.93	1.4311	73.43±8.7
74	67.28	49.1	1.4941	24.52±2.98
72	65.46	47.27	1.3105	8.61±1.25
70	63.63	45.44	1.2372	1.11±0.22
68	61.8	43.62	1.2052	0.26±0.07

Table 5.3: Measured evaporation residue cross-sections (σ_{ER}) for $^{18}O+^{186}W$ reaction. Tabulated energies are in center of mass systems. Here the sum of statistical and systematic errors are quoted as the total error in the measurement.

Coupled channels calculations [20, 21] explain the fusion cross-section rather well at lower excitation energies by precisely considering different degrees of freedom such as deformation of colliding nuclei, collective surface vibrations, and neutron transfer. In the present study, CC calculations were carried out to explore the effect of coupling of different states of the targets and projectile below the Coulomb barrier energy region.

5.4 Coupled channels calculations

The fission cross-sections for ^{18}O+^{182,184,186}W reactions are negligibly small in the below-barrier energy regions [57]. Hence, we can directly compare the measurements against the coupled channel calculations. The measured fusion cross-sections for ^{18}O+^{182,184,186}W reactions are analyzed using coupled channel code CCFULL [20, 21, 58]. The cross-sections are first compared with the 1D-BPM calculations. Contributions of inelastic states of colliding nuclei are also included in the computations to study the channel coupling effects. Table 5.4 lists the projectile and target excitation energies and their corresponding deformations.

Nucleus	Energy of 1^{st} Ex. state (MeV)	β_2	β_4	Ref.
^{16}O(Sphe.)	—	—	—	
^{18}O(Vib.)	1.982	0.355	—	[59]
^{182}W(Rot.)	0.100	0.251	-0.066	[59, 60]
^{184}W(Rot.)	0.111	0.236	-0.093	[59, 60]
^{186}W(Rot.)	0.122	0.226	-0.045	[59, 61]

Table 5.4: Deformation parameters and first excitation energies of different nuclei used in the CC calculations.

5.4.1 Coupled channel calculations for ^{16}O+^{182,184,186}W reactions

Akyuz-Winther (AW) parametrization of nuclear potential is used to obtain Woods-Saxon potential parameters in CC calculations. For CC calculations, parameters such as depth of potential (V_0), radius (r_0), and diffuseness (a) are taken from the closest system ^{16,18}O+^{181}Ta [63]. The parameters V_0, r_0 and a are selected as 98.76 MeV, 1.15 fm, and 0.73 fm for cc calculations, which reproduces the experimental fusion barriers for ^{16}O+^{182,184,186}W reactions. The cross-sections from CCFULL calculations with these potential parameters without including any coupling are termed as 1D-BPM excitation function. For

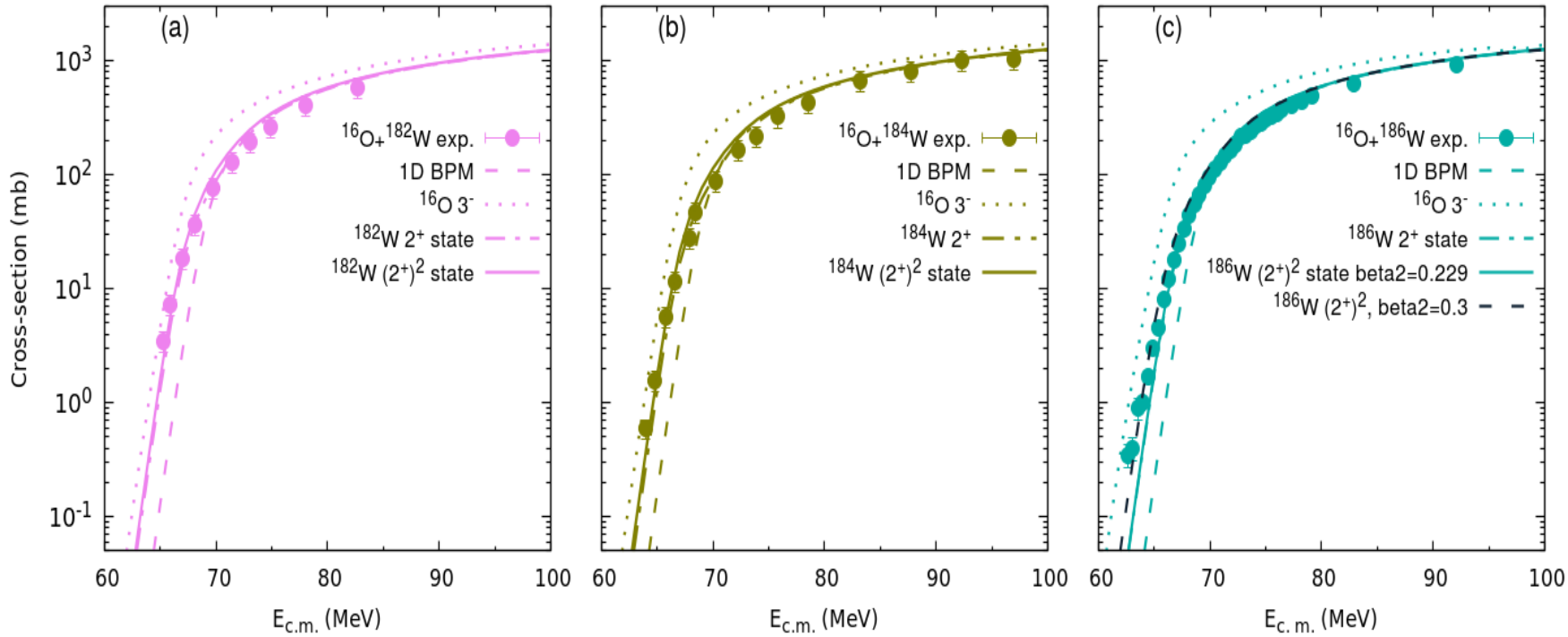

Figure 5.4: Fusion excitation functions for the ^{16}O+ ^{182,184,186}W reactions. The violet, olive-green, cyan solid circles are experimental corss-sections of ^{16}O+ ^{182,184,186}W reactions from Refs. [50, 51, 61, 62] respectively. The dashed lines represent the CC calculations without any coupling (1D-BPM). The solid and dotted lines represents theoretical fusion cross-sections obtained after including the deformation of targets and vibrational state of projectile respectively in CC calculations. Black dashed lines in panel (c) represents CC calculations of ^{16}O+^{186}W after including the deformation of the target with a modified quadrupole deformation parameter β_2=0.3.

^{16}O+^{182,184,186}W reactions, 1D-BPM calculations explain the fusion cross-sections in the above barrier region.

In order to explain the below-barrier fusion cross-sections of ^{16}O+^{182,184,186}W reactions, first we include the lowest energy state (that is 3^- state) of ^{16}O having energy 6.130 MeV and octopole deformation $\beta_3 = 0.729$ [64] in the CC calculations. The inclusion of 3^- state of ^{16}O alone in CC calculations, shows higher values compared to the experimental fusion cross-section as shown by brown dotted lines in Fig. 5.4(a), 5.4(b) and 5.4(c). According to Hagino *et al.*[65], the energy of the 3^- state of ^{16}O is very high compared to the curvature ($\hbar\omega$) of the excitation function and its inclusion in the CC calculations will have a re-normalization effect on the static potential without significantly changing the shape of the barrier distribution. In the same way, inclusion of 3^- state in CC calculations of ^{16}O+^{182,184,186}W reactions gives higher theoretical values compared to the experimental fusion data. Accordingly, corresponding coupling was not included in our final CC calculations. We treat the ^{16}O as spherical for CC calculations of ^{16}O+^{182,184,186}W reactions. Also, we treat the tungsten isotopes as deformed. In CC calculations we included their 0.250, 0.234, 0.226 quadrupole and -0.066, -0.093 -0.045 hexadecapole deformations respectively for ^{182,184,186}W nuclei. Thus, coupling of quadrupole and hexadecapole deformation of the target with the relative motion of colliding nuclei explained the fusion cross-sections of ^{16}O+^{182,184,186}W as shown by the brown solid lines in Fig. 5.4(a), 5.4(b), and 5.4(c).

5.4.2 Coupled channel calculations for ^{18}O+^{182,184,186}W reactions

Same set of deformation parameters, used for the target nuclei in ^{16}O+^{182,184,186}W reactions are used for the CCFULL calculations of ^{18}O+^{182,184,186}W reactions also.

Eventually projectile excitations are added in the CC calculations. With the inclusion of 3^-, state of ^{18}O with energy 5.097 MeV [64] and octopole deformation 0.595 [66] along with the quadrupole and hexadecapole deformation of targets, CC calculations show higher cross-sections as compared to the experiment as shown by the brown dotted lines in Fig. 5.5(a), 5.5(b), and 5.5(c). Thus the 3^-, state of ^{18}O is not included in the final CC calculations. We observe that, the 2^+ vibrational state of ^{18}O with energy 1.982 MeV coupled with the quadrupole and hexadecapole deformations of ^{182,184,186}W, reproduce the experimental cross-sections of ^{18}O+^{182,184,186}W reasonably in the whole energy range. The calculated results, which reproduce the experimental cross-sections of ^{18}O+^{182,184,186}W reactions, are shown by brown solid lines, in Fig. 5.5(a), 5.5(b), and 5.5(c).

In the below-barrier energy regions, to explain the enhanced fusion cross-sections, Esbensen *et al.*[25] considered the presence of a strong pair-transfer channel with a positive Q-value. All ^{18}O induced reactions under this study possess a positive 2n-transfer channel. Thus, 2n-transfer channels are included in the coupling scheme of ^{18}O+^{182,184,186}W reactions to see the effect of PQNT channel on below-barrier fusion cross-sections. ^{18}O+^{182,184,186}W reactions have positive Q-values of 1.414, 0.757, 0.133 MeV respectively for the 2n-stripping channel. The CCFULL code [20, 21] is having an option to include one transfer channel in the calculations. It can be a proton or neutron channel. The calculations are done, including both the 2n-transfer channel and the inelastic excitations. The result is illustrated as green double-dotted dashed lines in Fig. 5.5(a), 5.5(b), and 5.5(c). The neutron transfer coupling has been included in the CCFULL code for the present system through the transfer coupling strength parameter for 2n-transfer.

The code CCFULL accounts for the transfer channel through the macroscopic transfer coupling form factor, F_{tr}(r). In principle, the form factor is estimated

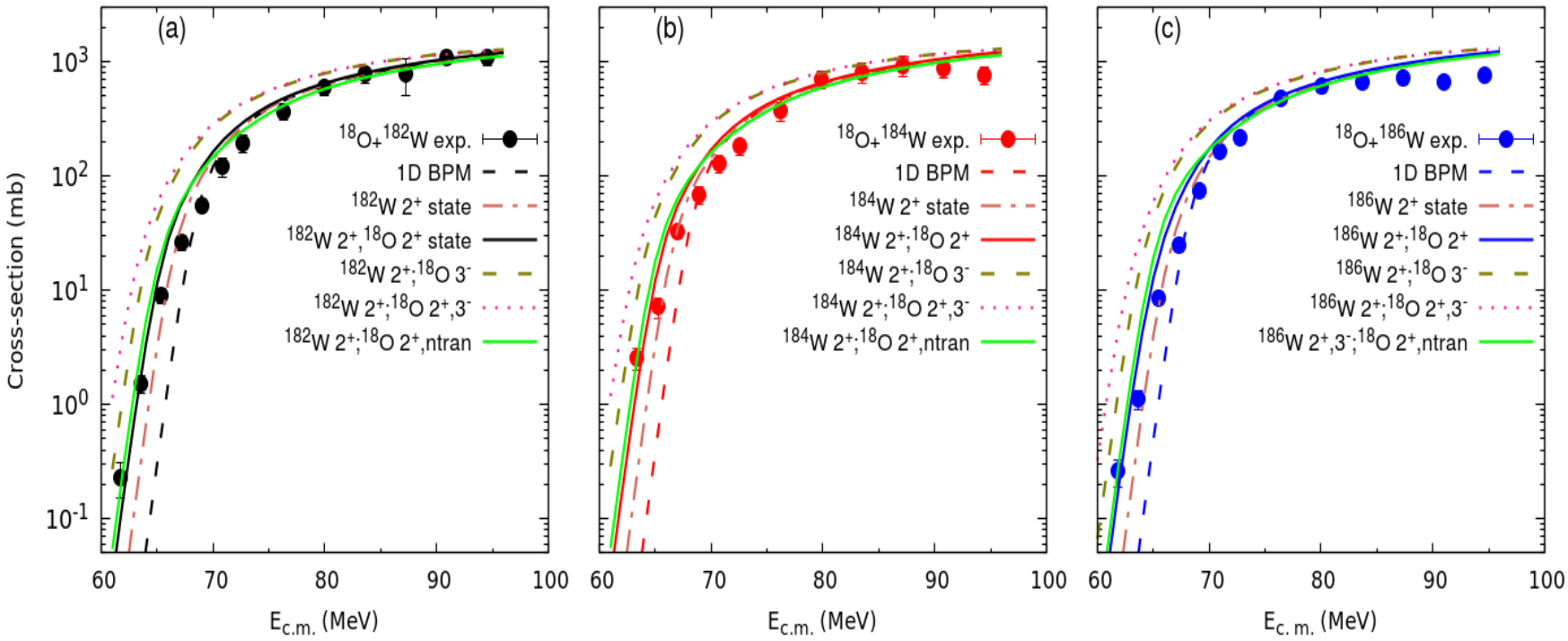

Figure 5.5: Fusion excitation functions for ^{18}O+ ^{182,184,186}W reactions. The black, red and blue solid circles are experimental results. The dashed lines represent the CC calculations without any coupling (1D-BPM). The solid lines represents CC calculations with 2^+ vibrational state of projectile and deformations of targets. Dotted lines represent CC calculations with 3^- vibrational state of projectile and deformation of targets. Green double-dotted dashed lines represents CC calculations after including neutron transfer.

from the differential and total transfer cross-sections [67, 68] as mentioned in the introduction. Since experimental transfer measurements do not exist for this system, the transfer form factor is unknown, and only a qualitative measure of the transfer strength is possible. The coupling strength is related to the form factor by the relation $F_{tr}(r) = F_{tr}\frac{dV_N}{dR}$. The coupling strength in the CCFULL calculations was varied until a fairly good agreement with experimental data was achieved as done by Deb *et al.* [53]. The green double-dotted dashed lines in Fig. 5.5(a), 5.5(b), and 5.5(c) shows results of CCFULL calculations after including transfer channel with a transfer strength 0.42 fm along with inelastic excitations. Beyond coupling strength of 0.5 fm, CC calculations started deviating from the experimental measurements. It is difficult to distinguish or separate theoretical excitation function with neutron transfer from that of without transfer channels. Thus without invoking the coupling of the transfer channel, which was one of the motivations for the measurement, CC calculations explained experimental data.

5.4.3 A self consistent method-Relative Change

We define the term relative change (R) to provide better predictions about the effects of neutron transfer channels on fusion reactions of ^{18}O+^{182,184,186}W. The positive or negative values of R, respectively quantify the increase or decrease in experimental cross-sections as compared to theoretical ones. R is defined as the ratio of the difference between the experimental (σ_{Exp}) and theoretical (σ_{theo}) fusion to the theoretical fusion cross-section, i.e. $R = (\sigma_{Exp}\text{-}\sigma_{theo})/\sigma_{theo}$. We quantify R by incorporating several possible inelastic excitations together with the relative motion in the CC calculations. After incorporating inelastic channels in CC calculations, R is expected to be zero for ^{16}O+^{182,184,186}W reactions, where the PQNT effect was not expected. Accordingly, these reactions are taken as the benchmark for comparing the enhancement due to PQNT in ^{18}O+^{182,184,186}W

reactions.

First, we calculate the values of R in ^{16}O and ^{18}O induced reactions using only 1D-BPM. All six reactions exhibit a value for R greater than zero at energies below the Coulomb barrier. Since R indicates the relative increase in experimental cross-sections with respect to the theory, any values of R greater than zero implies lower cross-sections values of the theory. Also increase in R indicates the absence of inelastic channels in the coupling. Accordingly, to account for the experimentally observed cross-sections, it is necessary to include inelastic channels in the coupling at below barrier energies. As shown by solid circles connected by brown dashed lines in Fig. 5.6 (a), 5.6 (b), and 5.6 (c), at below-barrier energies. R for ^{18}O induced reactions was larger values than that of ^{16}O induced one. The enhancement effect compared to 1D-BPM calculations is higher in ^{18}O+^{184,186}W reactions than ^{16}O induced ones. This may be an indication that more channels should be added in the coupling calculations of ^{18}O to reproduce the experimental values in compared to ^{16}O induced reactions. In the case of ^{16}O+^{182}W reaction, cross-sections for the lower energies are not available [49]. Due to this it will be difficult to make comparative statements regarding larger R values compared to 1D-BPM calculations in ^{18}O+^{182}W than that of ^{16}O+^{182}W reaction.

After including the quadrupole and hexadecapole deformation of the target, ^{18}O induced reactions show R greater than zero, which maximizes at sub-barrier energy regions as shown in Fig. 5.6(d), 5.6(e), and 5.6(f). Therefore it is necessary to include an additional coupling to explain below-barrier cross-sections. Here the additional coupling is the vibrational excitations of the ^{18}O projectile. For ^{16}O induced ones, R approaches zero for most of the below-barrier energy points while including deformation of targets in CC calculations. This zero R value indicates a good agreement between theory and the experiment. The the-

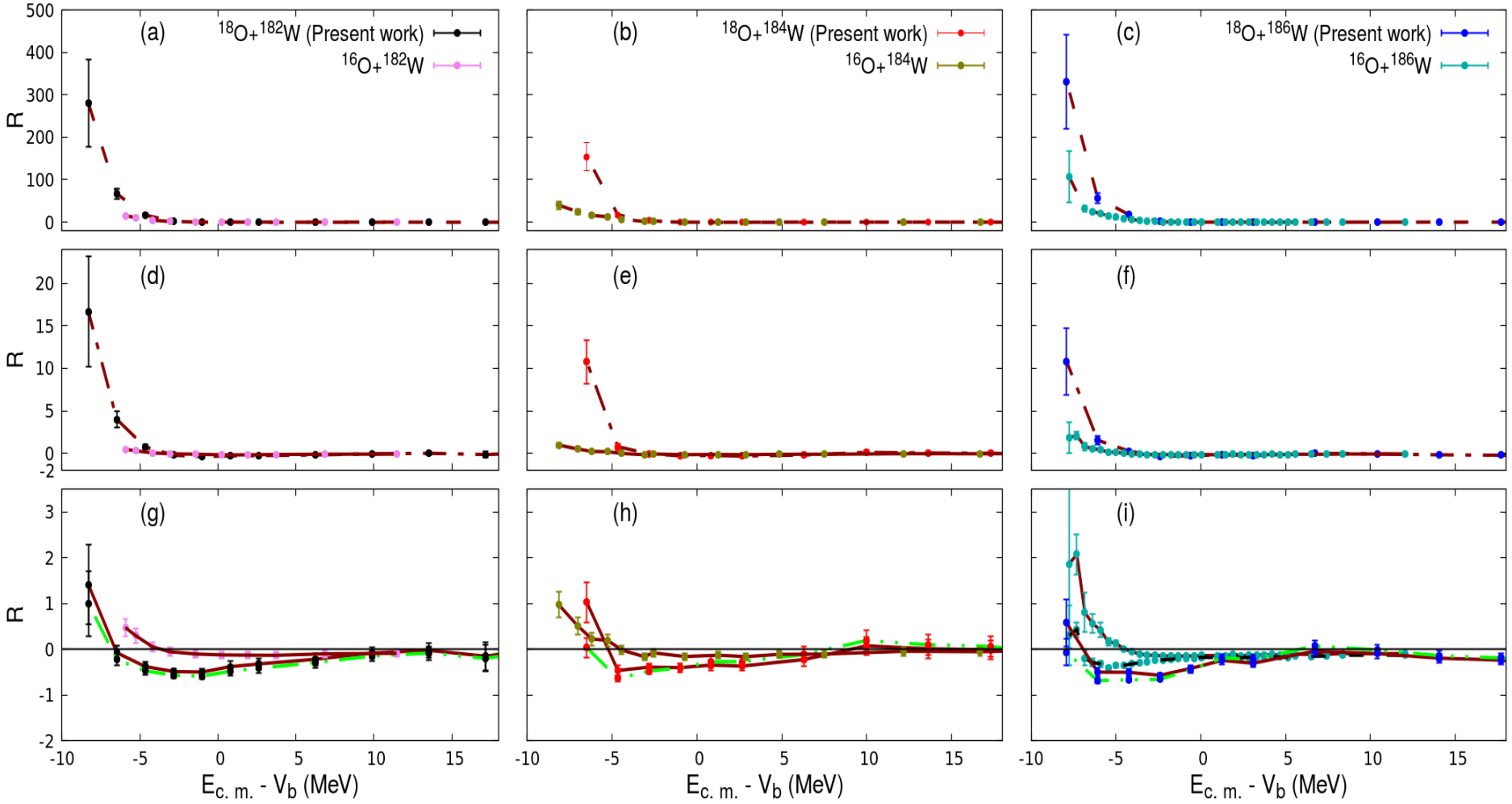

Figure 5.6: Relative enhancement as a function of $E_{c.m.}/V_B$ for ^{16,18}O+^{182,184,186}W. Panels (a), (b) and (c) represent an enhancement of experimental cross-sections from 1D-BPM. Panels (d), (e), and (f) represent the R from the calculated CC cross-section after including target excitations only. Figures in panel (g), (h), and (i) represent the R after including all order coupling in CC calculation. Black, red, and blue solid circle connected by green double-dotted dashed lines represents R after including neutron transfer in CC calculations. Cyan solid circle connected by black dashed lines in panel (g) represents R of ^{16}O+^{186}W with a modified deformation β_2=0.3.

oretical compliance is shown by solid circles connected by brown coloured solid lines in Fig. 5.6(d), 5.6(e), and 5.6(f). Among different possible coupling channels, we have considered only the deformation of the targets for ^{16}O induced reactions. After that, R approaches zero for all energy points and shows a slight deviation only at one energy point in the sub-barrier energy region. For ^{18}O induced reactions, we have to include the vibrational coupling of the projectile in addition to quadrupole and hexadecapole deformation of the targets to explain the deviation of R from zero. After including vibrational excitation of the projectile and deformation of the target in the coupling, theoretical excitation function agrees well with the experimental data for all ^{18}O induced reactions in below-barrier energy regions. It is shown as black, red, blue solid circle connected by the brown colored solid lines in Fig. 5.6 (g), 5.6 (h) and 5.6 (i).

To explore the effect of PQNT channels in fusion cross-sections, we have calculated R , including the neutron transfer channel in ^{18}O+ ^{182,184,186}W reactions. Even the addition of a neutron transfer channel in coupling does not improve the agreement between the experiment and theory. This indicates that, contrary to expectations, coupling of the neutron transfer channel in CC calculations does not provide any robust increase to the theoretical cross-sections of ^{18}O+ $^{182+,184,186}$W. Solid circle connected by green double-dot dashed lines in Fig. 5.6 (g), 5.6 (h) and 5.6 (i) show R obtained for ^{18}O+ ^{182,184,186}W reactions after including neutron transfer channels. As seen in Fig. 5.6 (g), 5.6 (h) and 5.6 (i) R with neutron channel does not deviate significantly from that without neutron transfer channel inclusion. The 2n-transfer Q-values of (^{18}O +^{182}W) > (^{18}O +^{184}W) > (^{18}O +^{186}W). However, increase in cross-sections with the increase in 2n-transfer Q-value is not observed at the below-barrier energy levels of these reactions.

At below barrier energies, CC calculations of ^{16}O+^{186}W show lower values

compared to the experimental cross-sections. R shows a bit higher value, beyond $E_{c.m.}-V_b$= -7 MeV. For ^{16}O+^{186}W reaction, many works [49, 50, 61, 69] explained the enhanced below-barrier cross-sections. Among this ANU group [49, 50, 61] used potential parameters, and diffuseness deduced from elastic scattering data for CC calculations. The associated deformation parameters of ^{186}W were β_2 ≈0.24 and β_4 ≈-0.09. They also tried to fit the fusion data of ^{16}O+ ^{186}W by varying potential parameters and deformation. They obtained an optimum fit with a diffuseness a= 1.27 fm and with an average barrier of 68.9 MeV and also obtained best-fit deformation parameters β_2 ≈0.3 and β_4 ≈-0.045. This β_2 value is larger than that obtained from elastic scattering data, and β_4 was smaller than that of non-fusion data observed by Lemmon *et al*. [61]. The possible explanation for this lies in the change in the shape of the barrier distribution. Generally, any additional coupling effects will result in the smoothing of the barrier. However, the effect of coupling will have a higher impact when the barrier distribution has sharp changes. Effect of deformations will be predominant in such systems [61]. Barrier distribution of ^{16}O+^{186}W reaction shows a sharp change before adding the coupling [61]. We have carried out the CC calculations for ^{16}O+ ^{186}W reaction with deformation parameters β_2 ≈ 0.3 and β_4 ≈ -0.045 which were used by Lemmon *et al*. [61] to explain the fusion data. The corresponding results are shown as black dashed line in Fig. 5.4(c). Calculations with deformation values extracted from elastic scattering data are also shown in Fig. 5.4(c) as brown solid lines. R calculated with this modified deformation value is shown as solid circle connected by black dashed lines in Fig. 5.6(i). The Fig. 5.6(i) shows that the deviations of R from zero vanishes at below-barrier energy points with this modified deformation value and shows good agreement between the theory and the experiment.

Excitation functions of ^{16}O+^{182,184,186}W systems, which all have negative

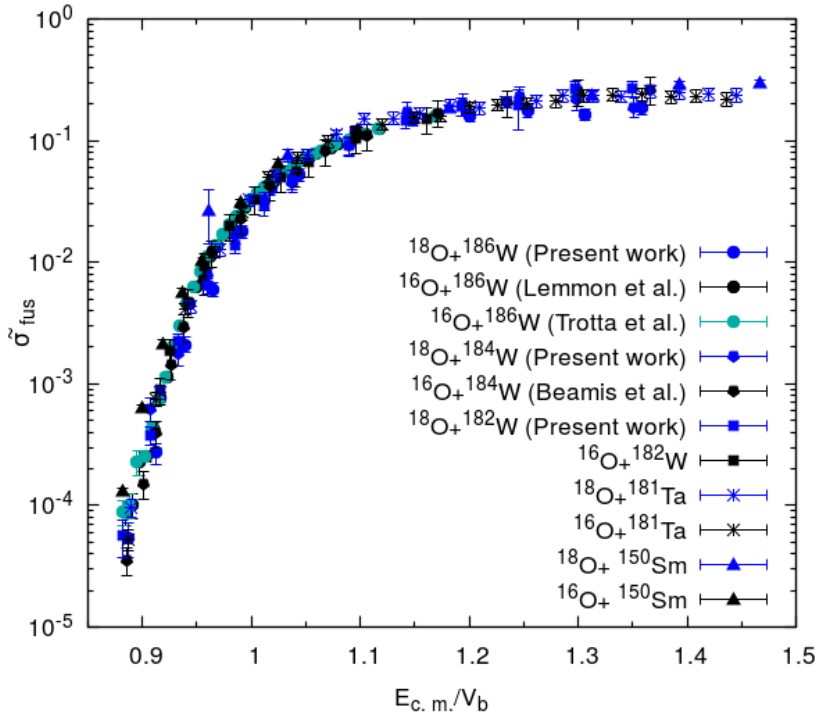

Figure 5.7: Reduced fusion cross-sections as a function of $E_{c.m.}/V_b$ for reactions induced by ^{16,18}O. Here, reduced cross-section is obtained by dividing absolute cross-section with πR_b^2, where V_b and R_b are the Bass barrier and Bass radius [66]. The fusion cross-sections of ^{16,18}O+^{150}Sm [70], ^{16,18}O+^{181}Ta [63], ^{16}O+^{182}W [51], ^{16}O+^{184}W [62] and ^{16}O+^{186}W [50, 61] are obtained from literature.

transfer Q-value for neutron transfer, are explored using coupled channel calculations. The coupling of relative motion of colliding partners with inelastic excitations of target was enough to explain the experimental cross-sections above and below the Coulomb barrier energy regions as shown in Fig. 5.4 and Fig. 5.6. In the measured energy range, the 2^+ vibrational state of ^{18}O coupled with the quadrupole and hexadecapole state of ^{182,184,186}W show a relatively good agreement between the calculated and experimental results. An additional coupling of neutron transfer channel in ^{18}O+^{182,184,186}W reactions do not show a different R value from calculations without neutron transfer. Plots in Fig. 5.6(g), 5.6(h) and 5.6(i) with solid circles joined by green double dotted dashed lines shows R with neutron transfer channel.

The Q-values for the 2n-transfer processes are positive for all reactions with ^{18}O. Thus, the neutron transfer can be important for the reactions with the ^{18}O beam. However, our results show that cross-sections for reactions with ^{16}O and ^{18}O induced reactions are very similar. A small decrease in deformation of the target after 2n-neutron transfer may explain this results. Coulomb barriers of the systems before and after 2n-transfer are almost the same, and, correspondingly, their fusion cross-sections are similar [39, 40]. Such results are observed in many system like ^{16,18}O+^{76,74}Ge [71–73], ^{16,18}O+^{112,118,124}Sn [31] etc.

5.4.4 Systematics of ^{18}O induced reactions

A positive 2n-transfer Q-value characterizes the majority of ^{18}O induced reactions. Several experiments in low, medium and heavy mass regions have been carried out to investigate the effect of the 2n-transfer Q-value in fusion cross-sections induced by ^{18}O [34, 52, 53, 63]. Compared to other transfer channels, 2n-transfer has a significant effect on sub-barrier fusion enhancement [30].Montagnoli and Stefanini [5] suggested that, when heavier systems are compared, multi-phonon excitations have a more significant impact on sub-barrier fusion. Also, if multi-phonon excitations are dominant, then the effect of PQNT will be weaker in the case of heavier systems [5]. Thus, the effect of PQNT channels can only be seen at extremely low energies. For making conclusive remarks on the effect of PQNT on heavier systems, a systematic study in the same mass regions is needed.

For a systematic study in the heavy mass region, we compared the reduced fusion cross-sections of several ^{18}O induced reactions with that of ^{16}O induced ones (having negative neutron transfer Q-value). Reduced cross-section will eliminate the effects of the barrier height and nuclear size [43]. We eliminated the effects of geometrical aspects by using traditional reduction methods ($\tilde{\sigma}_{fus} = \frac{\sigma_{fus}}{\pi R_b^2}$, where R_b the barrier radius). When compared to ^{16}O induced reactions in the heavy

Reaction	2n-stripping Q-value	Neutron No: of target After 2n-transfer	Deformation of Target Before 2n-transfer	Deformation of Target After 2n-transfer	Exp. evidence for PQNT	Ref.
$^{18}O+^{58}Ni\rightarrow^{76}Kr$	8.199	32	0.179	0.2050[74]	Yes	[75]
$^{18}O+^{63}Cu\rightarrow^{81}Rb$	5.638	36	0.151	-0.125[60]	No	[76]
$^{18}O+^{65}Cu\rightarrow^{83}Rb$	5.638	38	-0.125	-0.085[60]	No	[76]
$^{18}O+^{74}Ge\rightarrow^{92}Zr$	3.745	44	0.283	0.2623[59]	No	[71]
$^{18}O+^{92}Mo\rightarrow^{110}Sn$	5.559	52	0.1058	0.1509[59]	Yes	[77, 78]
$^{18}O+^{112}Sn\rightarrow^{130}Ce$	5.856	64	0.1207	0.1147[66]	No	[31]
$^{18}O+^{116}Sn\rightarrow^{134}Ce$	4.081	68	0.1117	0.1100[66]	Yes	[53]
$^{18}O+^{118}Sn\rightarrow^{136}Ce$	3.4	70	0.1100	0.1063[66]	No	[31]
$^{18}O+^{124}Sn\rightarrow^{142}Ce$	1.735	76	0.0942	0.0825[66]	No	[31]
$^{18}O+^{150}Sm\rightarrow^{168}Yb$	1.666	90	0.1931	0.3065[59]	Yes	[70]
$^{18}O+^{181}Ta\rightarrow^{199}Tl$	0.809	110	0.255	0.244[66]	No	[63]
$^{18}O+^{182}W\rightarrow^{200}Pb$	1.414	110	0.251	0.236[59]	No	this work
$^{18}O+^{184}W\rightarrow^{202}Pb$	0.757	112	0.236	0.226[59]	No	this work
$^{18}O+^{186}W\rightarrow^{204}Pb$	0.113	114	0.226[59]	0.197[74]	No	this work

Table 5.5: Lists of ^{18}O induced reactions with their 2n-stripping Q-values, neutron number of target after 2n-transfer and target deformations before and after 2n-stripping.

mass region as seen in Fig.5.7, ^{18}O induced reactions do not exhibit a significant increase. In the majority of the systems under investigation, there is no discernible enhancement in below-barrier fusion cross-sections. The ^{18}O+^{150}Sm system is the only one that shows enhancement in the below-barrier region when compared to the ^{16}O induced reference system. The reduced cross-section of ^{18}O+^{181}Ta does not exhibit fusion enhancement in the below barrier region, compared to the reference system ^{16}O+^{181}Ta as seen in Fig. 5.7. When compared to reference systems, there is no noticeable enhancement in ^{18}O+^{182,184,186}W reactions as seen in Fig. 5.7. Our CC calculations on the same, discussed in Sec. 5.4, also conclude the same. The deviating behavior of ^{18}O+^{150}Sm may be attributed to the change in the deformation of the target nuclei after 2n-transfer. All other reactions that we considered in our study show a decrease in deformation of the target nuclei after 2n-transfer, whereas ^{18}O+^{150}Sm shows an increase. Examining of the deformation values of the target nuclei in ^{18}O+^{150}Sm reactions revealed a relatively higher change in deformation after neutron transfer when compared to that of other systems. The present measurements, as shown in Fig. 5.7, exhibit a spread in excitation function in the above-barrier energy regions. It could be attributed to the presence of other channels such as non-compound nuclear fission or break-up channels, etc. [1].

To check whether the reason for enhancement in ^{18}O+^{150}Sm is extendable to low and medium mass regions, we have carried out a systematic study on all ^{18}O induced reactions available in the literature. Table 5.5 lists the reactions used in the systematic study as well as their transfer Q-values. In comparison to its reference system, the ^{16}O+^{60}Ni, fusion enhancement is expected in ^{18}O+^{58}Ni system due to the presence of PQNT. Examination of fusion and elastic scattering data of ^{18}O+^{58}Ni by Silva *et al.* [75] confirmed the enhancement. Fusion calculations of ^{18}O+^{63,65}Cu reactions by Chamon *et al.* [76] do not find any

projectile dependence on fusion cross-sections. Due to the PQNT channel, it is expected that there would be an enhancement for ^{18}O+^{74}Ge in the below-barrier energy region. Their theoretical predictions of fusion data with CC calculation and their barrier distributions show no such effect [71–73]. For ^{18}O+^{92}Mo Monteiro *et al.* [78] suggested a need for coupling with transfer channels to explain quasi-elastic barrier distributions. A comprehensive study on ^{16,18}O+$^{112-124}$Sn by Jacobs *et al.* [31] does not find any enhancement due to the PQNT channel on sub-barrier fusion cross-section. Inclusion of PQNT in CC calculations, showed an enhancement in ^{18}O+^{116}Sn [53].

In order to conclude the effect of PQNT channels on fusion enhancement of ^{18}O induced reactions, we looked at the ^{18}O induced reactions that were available in the literature. Compared to the reference systems, cross-sections of most of the reactions given in the Table 5.5 do not exhibit an enhancement due to the effect of PQNT channel [31, 63, 71, 76]. ^{18}O+^{58}Ni, ^{18}O+^{92}Mo and ^{18}O+^{150}Sm reactions show an enhancement due to the presence of PQNT channel [70, 75, 78]. In these three reactions, after 2n-transfer, the target deformation increased. As the deformation increases, the barrier height decreases, increasing the below-barrier fusion cross-sections. All of this points to the conclusion that in systems with a PQNT channel if the system's deformation increases after neutron transfer, it leads to fusion enhancement. Because Z_pZ_t values stay the same after 2n-transfer, the increase in deformation may lead to the decrease in barrier height and resulting in fusion enhancement. The highlighted systems in Table 5.5 which shows an enhancement due to PQNT [70, 75, 78] reveals that, the enhancement occurs only when the deformation of target increases after 2n-transfer. Furthermore, a higher 2n-transfer Q-value does not guarantee a more considerable enhancement. Also none of the highlighted systems in Table 5.5 approach neutron shell closure values for target after 2n-transfer.

Bibliography

[1] B. B. Back, H. Esbensen, C. L. Jiang, and K. E. Rehm, Rev. Mod. Phys. **86**, 317 (2014).

[2] A. B. Balantekin and N. Takigawa, Rev. Mod. Phys. **70**, 77 (1998).

[3] M. Dasgupta, D. J. Hinde, N. Rowley, and A. M. Stefanini, Annu. Rev. Nucl. Part. Sci. **48**, 401 (1998).

[4] C. Y. Wu, W. V. Oertzen, D. Cline, and M. W. Guidry, Annu. Rev. Nucl. Part. Sci. **40**, 285 (1990).

[5] G. Montagnoli and A. M. Stefanini, Eur. Phys. J. A **53**, 169 (2017), 1707.07583.

[6] J. R. Leigh, M. Dasgupta, D. J. Hinde, J. C. Mein, C. R. Morton, R. C. Lemmon, J. P. Lestone, J. O. Newton, H. Timmers, J. X. Wei, and N. Rowley, Phys. Rev. C **52**, 3151 (1995).

[7] J. D. Bierman, P. Chan, J. F. Liang, M. P. Kelly, A. A. Sonzogni, and R. Vandenbosch, Phys. Rev. Lett. **76**, 1587 (1996).

[8] A. M. Stefanini, D. Ackermann, L. Corradi, J. H. He, G. Montagnoli, S. Beghini, F. Scarlassara, and G. F. Segato, Phys. Rev. C **52**, R1727 (1995).

[9] V. Tripathi, L. T. Baby, J. J. Das, P. Sugathan, N. Madhavan, A. K. Sinha, P. V. Madhusudhana Rao, S. K. Hui, R. Singh, and K. Hagino, Phys. Rev. C **65**, 014614 (2001).

[10] A. M. Stefanini, D. Ackermann, L. Corradi, D. R. Napoli, C. Petrache, P. Spolaore, P. Bednarczyk, H. Q. Zhang, S. Beghini, G. Montagnoli, L. Mueller, F. Scarlassara, G. F. Segato, F. Soramel, and N. Rowley, Phys. Rev. Lett. **74**, 864 (1995).

[11] A. M. Stefanini, L. Corradi, A. M. Vinodkumar, Y. Feng, F. Scarlassara, G. Montagnoli, S. Beghini, and M. Bisogno, Phys. Rev. C **62**, 014601 (2000).

[12] V. Denisov, Eur. Phys. J. **7**, 34 (2000).

[13] J. M. B. Shorto, P. R. S. Gomes, J. Lubian, L. F. Canto, and P. Lotti, Phys. Rev. C **81**, 044601 (2010).

[14] V. I. Zagrebaev, Phys. Rev. C **67**, 061601 (2003).

[15] J. J. Kolata, A. Roberts, A. M. Howard, D. Shapira, J. F. Liang, C. J. Gross, R. L. Varner, Z. Kohley, A. N. Villano, H. Amro, W. Loveland, and E. Chavez, Phys. Rev. C **85**, 054603 (2012).

[16] M. Trotta, A. M. Stefanini, L. Corradi, A. Gadea, F. Scarlassara, S. Beghini, and G. Montagnoli, Phys. Rev. C **65**, 011601 (2001).

[17] R. Broglia, C. Dasso, S. Landowne, and G. Pollarolo, Phys. Lett. B **133**, 34 (1983).

[18] S. Kalkal, S. Mandal, N. Madhavan, A. Jhingan, E. Prasad, R. Sandal, S. Nath, J. Gehlot, R. Garg, G. Mohanto, M. Saxena, S. Goyal, S. Verma, B. R. Behera, S. Kumar, U. D. Pramanik, A. K. Sinha, and R. Singh, Phys. Rev. C **83**, 054607 (2011).

[19] C. S. Palshetkar, S. Thakur, V. Nanal, A. Shrivastava, N. Dokania, V. Singh, V. V. Parkar, P. C. Rout, R. Palit, R. G. Pillay, S. Bhattacharyya, A. Chatterjee, S. Santra, K. Ramachandran, and N. L. Singh, Phys. Rev. C **89**, 024607 (2014).

[20] K. Hagino, N. Rowley, and A. Kruppa, Comput. Phys. Commun. **123**, 143 (1999).

[21] K. Hagino and N. Takigawa, Prog. Theor. Phys. **128**, 1061 (2012).

[22] C. Dasso and S. Landowne, Comput. Phys. Commun. **46**, 187 (1987).

[23] M. Beckerman, M. Salomaa, A. Sperduto, H. Enge, J. Ball, A. DiRienzo, S. Gazes, Y. Chen, J. D. Molitoris, and M. Nai-feng, Phys. Rev. Lett. **45**, 1472 (1980).

[24] R. A. Broglia, C. H. Dasso, S. Landowne, and A. Winther, Phys. Rev. C **27**, 2433 (1983).

[25] H. Esbensen, S. H. Fricke, and S. Landowne, Phys. Rev. C **40**, 2046 (1989).

[26] H.-J. Hennrich, G. Breitbach, W. Khn, V. Metag, R. Novotny, D. Habs, and D. Schwalm, Phys. Lett. B **258**, 275 (1991).

[27] H. Timmers, D. Ackermann, S. Beghini, L. Corradi, J. He, G. Montagnoli, F. Scarlassara, A. Stefanini, and N. Rowley, Nuclear Physics A **633**, 421 (1998).

[28] A. M. Stefanini, F. Scarlassara, S. Beghini, G. Montagnoli, R. Silvestri, M. Trotta, B. R. Behera, L. Corradi, E. Fioretto, A. Gadea, Y. W. Wu, S. Szilner, H. Q. Zhang, Z. H. Liu, M. Ruan, F. Yang, and N. Rowley, Phys. Rev. C **73**, 034606 (2006).

[29] H. Q. Zhang, C. J. Lin, F. Yang, H. M. Jia, X. X. Xu, Z. D. Wu, F. Jia, S. T. Zhang, Z. H. Liu, A. Richard, and C. Beck, Phys. Rev. C **82**, 054609 (2010).

[30] Khushboo, N. Madhavan, S. Nath, A. Jhingan, J. Gehlot, B. Behera, S. Verma, S. Kalkal, and S. Mandal, Phys. Rev. C **100**, 064612 (2019).

[31] P. Jacobs, Z. Fraenkel, G. Mamane, and I. Tserruya, Phys. Lett. B **175**, 271 (1986).

[32] Z. Kohley, J. F. Liang, D. Shapira, R. L. Varner, C. J. Gross, J. M. Allmond, A. L. Caraley, E. A. Coello, F. Favela, K. Lagergren, and P. E. Mueller, Phys. Rev. Lett. **107**, 202701 (2011).

[33] A. M. Stefanini, G. Montagnoli, F. Scarlassara, C. L. Jiang, H. Esbensen, E. Fioretto, L. Corradi, B. B. Back, C. M. Deibel, B. Di Giovine, J. P. Greene, H. D. Henderson, S. T. Marley, M. Notani, N. Patel, K. E. Rehm, D. Sewerinyak, X. D. Tang, C. Ugalde, and S. Zhu, Eur. Phys. J. A **49**, 034606 (2013).

[34] Lin, C. J., Jia, H. M., Zhang, H. Q., Xu, X. X., Yang, F., Yang, L., Bao, P. F., Sun, L. J., and Liu, Z. H., EPJ Web of Conferences **66**, 03055 (2014).

[35] C. L. Jiang, K. E. Rehm, B. B. Back, H. Esbensen, R. V. F. Janssens, A. M. Stefanini, and G. Montagnoli, Phys. Rev. C **89**, 051603 (2014).

[36] V. A. Rachkov, A. V. Karpov, A. S. Denikin, and V. I. Zagrebaev, Phys. Rev. C **90**, 014614 (2014).

[37] G. L. Zhang, X. X. Liu, and C. J. Lin, Phys. Rev. C **89**, 054602 (2014).

[38] A. A. Ogloblin, H. Q. Zhang, C. J. Lin, H. M. Jia, S. V. Khlebnikov, W. H. Kuzmin, E. A. Trzaska, X. X. Xu, F. Yan, V. V. Sargsyan, G. G. Adamian, N. V. Antonenko, and W. Scheid, Eur. Phys. J. A **50** (2014).

[39] V. V. Sargsyan, G. G. Adamian, N. V. Antonenko, W. Scheid, and H. Q. Zhang, Phys. Rev. C **84**, 064614 (2011).

[40] V. V. Sargsyan, G. G. Adamian, N. V. Antonenko, W. Scheid, and H. Q. Zhang, Phys. Rev. C **85**, 024616 (2012).

[41] M. Dasgupta, P. R. S. Gomes, D. J. Hinde, S. B. Moraes, R. M. Anjos, A. C.

Berriman, R. D. Butt, N. Carlin, J. Lubian, C. R. Morton, J. O. Newton, and A. Szanto de Toledo, Phys. Rev. C **70**, 024606 (2004).

[42] K. Hagino, A. Vitturi, C. H. Dasso, and S. M. Lenzi, Phys. Rev. C **61**, 037602 (2000).

[43] L. Canto, P. Gomes, J. Lubian, L. Chamon, and E. Crema, Nuclear Physics A **821**, 51 (2009).

[44] V. A. Rachkov, A. Adel, A. V. Karpov, A. S. Denikin, V. I. Zagrebaev, P. A. DeYoung, G. F. Peaslee, B. Hughey, B. Atalla, M. Kern, P. L. Jolivette, J. A. Zimmerman, M. Y. Lee, F. D. Becchetti, E. F. Aguilera, E. Martinez-Quiroz, and J. D. Hinnefeld, Bull. Russ. Acad. Sci.: Phys **77**, 411 (2013).

[45] V. I. Zagrebaev, V. V. Samarin, and W. Greiner, Phys. Rev. C **75**, 035809 (2007).

[46] N. Rowley, I. Thompson, and M. Nagarajan, Phys. Lett. B **282**, 276 (1992).

[47] P. Stelson, Phys. Lett. B **205**, 190 (1988).

[48] Bertulani, Carlos A., EPJ Web of Conferences **17**, 15001 (2011).

[49] J. R. Leigh, J. J. M. Bokhorst, D. J. Hinde, and J. O. Newton, J Phys G Nucl Part Phys **14**, L55 (1988).

[50] Trotta, M., Stefanini, A. M., Beghini, S., Behera, B. R., Chizhov, A. Yu., Corradi, L., Courtin, S., Fioretto, E., Gadea, A., Gomes, P. R. S., Haas, F., Itkis, I. M., Itkis, M. G., Kniajeva, G. N., Kondratiev, N. A., Kozulin, E. M., Latina, A., Montagnoli, G., Pokrovsky, I. V., Rowley, N., Sagaidak, R. N., Scarlassara, F., Szanto de Toledo, A., Szilner, S., Voskressensky, V. M., and Wu, Y. W., Eur. Phys. J. A **25**, 615 (2005).

[51] D. J. Hinde, W. Pan, A. C. Berriman, R. D. Butt, M. Dasgupta, C. R. Morton, and J. O. Newton, Phys. Rev. C **62**, 024615 (2000).

[52] V. V. Sargsyan, G. G. Adamian, N. V. Antonenko, W. Scheid, and H. Q. Zhang, Phys. Rev. C **86**, 014602 (2012).

[53] N. K. Deb, K. Kalita, H. A. Rashid, S. Nath, J. Gehlot, N. Madhavan, R. Biswas, R. N. Sahoo, P. K. Giri, A. Das, T. Rajbongshi, A. Parihari, N. K. Rai, S. Biswas, Khushboo, A. Mahato, B. J. Roy, A. Vinayak, and A. Rani, Phys. Rev. C **102**, 034603 (2020).

[54] A. Sinha, N. Madhavan, J. Das, P. Sugathan, D. Kataria, A. Patro, and G. Mehta, Nucl. Instrum. Methods Phys. Res. A **339**, 543 (1994).

[55] E. T. Subramaniam, B. P. A. Kumar, and R. K. Bhowmik, Candle collection and analysis of nuclear data using linux network, (unpublished).

[56] J. Gehlot, S. Nath, T. Banerjee, I. Mukul, R. Dubey, A. Shamlath, P. V. Laveen, M. Shareef, M. M. Shaikh, A. Jhingan, N. Madhavan, T. Rajbongshi, P. Jisha, and S. Pal, Phys. Rev. C **99**, 061601 (2019).

[57] A. Gavron, Phys. Rev. C **21**, 230 (1980).

[58] CCFULL (a version with two different modes of excitation both in the proj. and in the targ.), `http://www2.yukawa.kyoto-u.ac.jp/ kouichi.hagino/ccfull.html`, accessed: 01-06-2021.

[59] S. Ramen, C. W. Nestor, and P. Tikkanen, At. Data Nucl. Data Tables **78**, 1 (2001).

[60] P. Möller, A. J. Sierk, T. Ichikawa, and H. Sagawa, At. Data Nucl. Data Tables **109-110**, 1 (2016).

[61] R. Lemmon, J. Leigh, J. Wei, C. Morton, D. Hinde, J. Newton, J. Mein, M. Dasgupta, and N. Rowley, Phys. Lett. B **316**, 32 (1993).

[62] C. E. Bemis Jr., T. C. Awes, J. R. Beene, R. L. Ferguson, H. Kim, F. K. McGowan, F. Obenshain, F. E.and Plasil, Z. Jacobs, P.and Frankel, U. Smilansky, and I. Tserruya, Ornl progressreport, unpublished (1986).

[63] P. Jisha, A. M. Vinodkumar, B. R. S. Babu, S. Nath, N. Madhavan, J. Gehlot, A. Jhingan, T. Banerjee, I. Mukul, R. Dubey, N. Saneesh, K. M. Varier, E. Prasad, A. Shamlath, P. V. Laveen, and M. Shareef, Phys. Rev. C **101**, 024611 (2020).

[64] T. Kibedi and R. Spear, At. Data Nucl. Data Tables **80**, 35 (2002).

[65] K. Hagino, N. Takigawa, M. Dasgupta, D. J. Hinde, and J. R. Leigh, Phys. Rev. Lett. **79**, 2014 (1997).

[66] V. I. Zagrebaev, A. S. Denikin, A. V. Karpov, A. P. Alekseev, M. A. Naumenko, V. A. Rachkov, V. V. Samarin, and V. V. Saiko, NRV web knowledge base on low-energy nuclear physics, `http://nrv.jinr.ru/` (1999).

[67] S. Saha, Y. K. Agarwal, and C. V. K. Baba, Phys. Rev. C **49**, 2578 (1994).

[68] C. Dasso and G. Pollarolo, Phys. Lett. B **155**, 223 (1985).

[69] M. Firihu, K. Hagino, and N. Takigawa, AIP Conf. Proc. **853** (2006).

[70] R. Charity, J. Leigh, J. Bokhorst, A. Chatterjee, G. Foote, D. Hinde, J. Newton, S. Ogaza, and D. Ward, Nucl. Phys. A **457**, 441 (1986).

[71] H. M. Jia, C. J. Lin, F. Yang, X. X. Xu, H. Q. Zhang, Z. H. Liu, L. Yang, S. T. Zhang, P. F. Bao, and L. J. Sun, Phys. Rev. C **86**, 044621 (2012).

[72] H. Jia, C. Lin, F. Yang, X. xu, H. Zhang, Z. Liu, L. Yang, S. Zhang, P. Bao, and L.-J. Sun, J. Phys. Conf. Ser. **420**, 2124 (2013).

[73] Lin, C. J., Jia, H. M., Zhang, H. Q., Xu, X. X., Yang, X. F., Yang, X. L., Bao, P. F., Sun, L. J., and Liu, Z. H., EPJ Web of Conferences **63**, 02007 (2013).

[74] B. N. L. National Nuclear Data Center, Nudat (nuclear structure and decay data) (2008).

[75] C. P. Silva, D. Pereira, L. C. Chamon, E. S. Rossi, G. Ramirez, A. M. Borges, and C. E. Aguiar, Phys. Rev. C **55**, 3155 (1997).

[76] L. Chamon, D. Pereira, E. Rossi, C. Silva, G. Razeto, A. Borges, L. Gomes, and O. Sala, Phys. Lett. B **275**, 29 (1992).

[77] M. Benjelloun, W. Galster, and J. Vervier, Nucl. Phys. A **560**, 715 (1993).

[78] D. Monteiro, R. Simes, J. Shorto, A. Jacob, L. Ono, L. Paulucci, N. Added, and E. Crema, Nucl. Phys. A **725**, 60 (2003).

Chapter 6

Summary and conclusion

In this chapter we summarises the fusion cross-section measurements, analysis and results of two heavy-ion reactions in A $\approx$ 200 region. The compound nuclei (CN) formed from the collision of asymmetric reaction partners, after capture decay to their ground state mainly via evaporation. The study of these decay products provides valuable information about the statistical and dynamic aspects of fusion reactions. The evaporation residues (ER) are the direct indicators of the compound nucleus formation and are the most sensitive probes for studying fusion hindrance. ERs can also provide valuable information about the onset of non-compound nuclear fission (NCNF) processes like quasi-fission (QF) that hinder CN formation.

In this thesis, I mentioned about the fusion cross-sections measurement of two sets of heavy-ion reactions at near and around barrier energies. Through our measurements, we studied the entrance channel behavior of the colliding systems on the fusion process at near-barrier energies. Also, we explored on the competing reaction mechanisms which hinders fusion. To fulfill the objectives, we used a mass spectrometer that works in vacuum mode. We used the Heavy Ion reaction analyzer (HIRA) at IUAC to measure the fusion cross-sections.

6.1 ER measurements for ^{16,18}O+^{181}Ta reactions

Quasi-fission, one of the hurdles in super-heavy element (SHE) production, had been predicted in heavy systems with the charge product, $Z_PZ_T > 1400$ [1]. However, the evaporation residue (ER) cross-sections measured for reactions forming ^{216}Ra compound nucleus are found to exhibit QF in very asymmetric combinations with $Z_PZ_T \approx 700$ [2]. Also, the presence of QF was reported in very asymmetric reactions forming ^{213}Fr, ^{210}Rn, ^{202}Po and ^{202}Pb nuclei [1, 3–6]. Thus a systematic understanding of the occurrence of QF, in pre-actinide region is needed, which will be vital in the study of fusion hindrance.

After capture the di-nuclear system (DNS) passes through a long dynamical path, during which it equilibrates in all degree of freedom to form a CN. This CN which survives from fission, de-excites via γ-ray emission or particle evaporation to form an ER. Thus the formation of ERs depends on capture cross-section (σ_{cap}), CN formation probability (P_{CN}) and its survival probability against fission (W_{sur}) through the relation, $\sigma_{ER} = \sigma_{cap}P_{CN}W_{sur}$. In heavy-ion collisions, the DNS may re-separate before complete equilibration and thereby reduce P_{CN}. This reduces the ER cross-sections. The ER cross-sections, at energies well above the fusion barrier is relatively insensitive to the form of the nuclear potential [3], and are mainly determined by Standard Statistical model (SSM) parameters [6]. Thus parameters like fission barrier scaling factor, k_f which relates to the fission barrier ($B_f(\ell)$) in agreement with the expression $B_f(\ell) = k_f B_f^{LD}(\ell) + \Delta W_{gs}$ (Here, $B_f^{LD}(\ell)$ the rotating liquid drop model fission barrier and ΔW_{gs} the ground state shell correction) and P_{CN} are used to explain the measured ER excitation function at higher energies.

ER cross-sections of two reactions ^{16,18}O+^{181}Ta forming ^{197,199}Tl CN were measured to explore on the presence of QF. Experiments are carried out at 15 UD Pelletron accelerator facility at IUAC, New Delhi. Pulsed beams of ^{16,18}O,

with pulse separation 4 μs, were bombarded on ^{181}Ta target of thickness $\approx$ 170 μg/cm^2 with a carbon backing 20 μg/cm^2. ERs were separated from intense beam background using the Heavy Ion Reaction Analyzer (HIRA). HIRA was kept at 0° with respect to the beam direction with 10 msr entrance aperture. ERs were measured from 68-110 MeV beam energy in steps of 2 MeV. A Multi-Wire Proportional Counter (MWPC) of active area 150×50 mm^2 was placed at the focal plane (FP) of HIRA for the detection of the ERs. Two silicon surface barrier detectors of active area 50 mm^2 each with a collimator diameter 1 mm were placed at a distance of 95.6 mm from the target inside the target chamber at an angle of ±15° with respect to beam direction for normalization of ER cross-sections. A time of flight (TOF) arrangement was set up between anode of MWPC and RF signal to separate the beam-like particles from ERs. Thus obtained ER counts were used to find the ER cross-sections.

Comparisons of α and $\alpha_{\rm BG}$ values predicted quasi-fission in ^{18}O+^{181}Ta reaction and no such process in ^{16}O+^{181}Ta. However, no specific signatures of fusion suppression due to QF were found in the ER excitation function of less asymmetric ^{18}O+^{181}Ta ($\alpha < \alpha_{\rm BG}$) reaction in comparison with more asymmetric ^{16}O+^{181}Ta ($\alpha > \alpha_{\rm BG}$). Also, we have analyzed the measured evaporation residue cross-sections using statistical model code HIVAP[7]. For both reactions, the ER excitation functions are well reproduced by HIVAP calculation with the same fission barrier scaling factor k_f and $P_{\rm CN}$=1, which indicates the absence of non-compound nuclear fission process. For ^{220}Th, CN forming reactions reported a strong sensitivity for entrance channel asymmetry with exit channel [8]. However, a comparison between ^{18}O+^{181}Ta and ^{19}F+^{180}Hf forming ^{199}Tl reactions shows no such strong sensitivity. This may be due to the lower value of fissility of the systems or the high resemblance in mass asymmetry. A systematic study was carried out to find the starting point of the fusion suppression in the

$A \approx 200$ regions. Highly fissile CN showed indirect evidence of the effects, such as lowering P_{CN} from one. This points to the conclusion that a high difference in mass asymmetry is needed to predict the limiting value of mass asymmetry, which triggers NCNF in less fissile systems.

Experiments that explore combinations leading to the same CN are required for better insight. Also, fission measurements of asymmetric reactions leading to the CN ^{197,199}Tl are required for better insight on starting of QF in pre-actinide nuclei.

6.2 ER measurements for ^{18}O+^{182,184,186}W reactions

Fusion reactions at near-barrier energies are influenced by the internal structure and entrance channel parameters of the interacting nuclei [9]. The fusion cross sections in sub-barrier regions were found enhanced by several orders of magnitude over the predictions of one-dimensional barrier penetration models (1D-BPM). Existing theoretical models have already established the role of nuclear deformation and vibration through the coupling of inelastic excitations along with the relative motion [10]. It was identified that reactions with positive Q-values transfer channel (PQNT) channels play a vital role in sub-barrier fusion cross-section enhancement [11]. However, many systems with PQNT channels do not exhibit a below-barrier fusion enhancement. Hence, we studied about the effect of role of positive Q-value of neutron transfer in fusion enhancement below the Coulomb barrier energy region.

We have performed the ER measurements of ^{18}O+^{182,184,186}W reactions, which have positive 2n-transfers Q-values. One of the main objectives of this work is to compare the ER cross-section with nearby systems, ^{16}O+^{182,184,186}W reac-

tions [12, 13], which have negative Q-values for 2n-transfer. To measure the cross-sections we have used a pulsed beam of ^{18}O with 4 μs pulse separation to bombard on the enriched ^{182,184,186}W targets of thickness 70 μg/cm^2, 300 μg/cm^2 and 100 μg/cm^2 respectively. As in the first experiment HIRA at IUAC was used to measure ERs from 68 MeV to 104 MeV in 2-4 MeV steps.

To consider the effect of neutron transfer Q-value in sub-barrier fusion enhancement, we measured the ER cross-sections of ^{18}O+^{182,184,186}W reactions. For asymmetric systems under consideration the fission cross-sections are negligibly small in the measured energy range. Thus, the measured evaporation residue cross-sections can be considered as the fusion cross-sections. All the reactions considered have positive Q-values for 2n transfer. Comparisons of these cross-sections with nearby systems with negative transfer Q-values for 2n helped to understand the role of positive Q-value on neutron transfer. Based on the positive 2n-transfer Q-value, one would have expected fusion enhancement in ^{18}O+^{182,184,186}W reactions. Experimental fusion cross-sections of both ^{18}O and ^{16}O induced reactions showed a strong enhancement compared to the 1D-BPM predictions at below-Coulomb barrier energy regions. On including the deformation of targets, Coupled Channel (cc) calculations explained the enhancement of ^{16}O+^{182,184,186}W reaction. Similarly, measured fusion excitation functions of ^{18}O+^{182,184,186}W reactions were explained by the inclusion of deformation of target and vibrational states of the projectile in the CC calculations. Comparing the fusion cross-sections of ^{18}O induced reactions with ^{16}O induced one, we conclude that the positive Q-value of neutron transfer channels does not affect the observed fusion cross-sections of ^{18}O+^{182,184,186}W reactions.

To quantify the effect of PQNT in the below-barrier fusion enhancement we introduced a quantity relative change (R). The positive or negative values of R, respectively quantify the increase or decrease in experimental cross-sections

as compared to theoretical ones. R is defined as the ratio of the difference between the experimental (σ_{Exp}) and theoretical (σ_{theo}) fusion to the theoretical fusion cross-section. We quantify R by incorporating several possible inelastic excitations together with the relative motion in the CC calculations. On incorporating inelastic channels in CC calculations, R goes to zero for ^{16}O+^{182,184,186}W reactions, where the PQNT effect was not expected. Similarly the inclusion of vibrational excitation of the projectile and deformation of the target in the coupling, theoretical excitation function agrees well with the experimental data for all ^{18}O induced reactions in below-barrier energy regions. The addition of a neutron transfer channel in coupling calculations of ^{18}O induced reactions does not improve the agreement between the experiment and theory. Contrary to expectations, coupling of the neutron transfer channel in CC calculations did not provide any robust increase to the theoretical cross-sections of ^{18}O+ $^{182+,184,186}$W. We confirmed the absence of below-barrier enhancement due to PQNT effects by a self-consistent method.

For making conclusive remarks on the effect of PQNT on heavier systems, a systematic study in the heavy mass regions were carried out. For a systematic study in the heavy mass region, we compared the reduced fusion cross-sections of several ^{18}O induced reactions with that of ^{16}O induced ones (having negative neutron transfer Q-value). When compared to ^{16}O induced reactions in the heavy mass region most of ^{18}O induced reactions do not exhibit a significant increase. The reactions which shows an enhancement in the below-barrier cross-sections compared to the reference system shows an increase in the target deformation after 2n-transfer. Thus from systematics we concluded that a higher deformation following neutron transfer enhances the cross-sections. Transfer measurements of systems with positive Q-value neutron transfer channels are needed, which will be helpful for making more conclusive remarks on transfer reactions.

6.3 Future perspective

In heavier nuclei fission barrier decreases with an increase in the number of protons due to repulsive Coulomb forces. When the proton numbers become large enough, the fission barrier will completely vanish, and an instantaneous break-up of a nucleus occurs. The heaviest known naturally occurring element is Uranium (Z=92). All elements above Uranium have been artificially synthesized in heavy ion laboratories, and they are all relatively unstable. Shell model predicts the presence of nuclei with atomic numbers 126. Though, the occurrence of such super-heavy nuclei is not found in nature. The absence of super-heavy elements in nature was due to the presence of some processes that hinder super-heavy element production. Heavy ion fusion reactions are the most successful mechanisms for super-heavy element production. Studies on heavy-ion fusion reactions will provide a comprehensive understanding of the factors affecting super heavy element production.

Evaporation residue cross-section measurements of heavy-ion collisions are, one of the principal methods to investigate the fusion suppression and enhancement observed in heavy systems. Understanding the causes of the fusion hindrance and enhancement in heavy-ion reactions is crucial in heavy element production. The evaporation residue measurements in the A $\approx$ 200 regions allow us to find factors influencing non-compound nuclear fission reactions and further help in explaining the reasons for fusion hindrances.

In our work, we explored quasi-fission, a process that hinders the formation of heavy nuclei. One of the influencing factors which reduces the heavy element production was the entrance channel mass-asymmetry of the colliding nuclei. In our study, we found that mass-asymmetry (α) and its critical value at Businaro-Gallone (BG) point (α_{BG}) values cannot be used to predict the presence of quasi-fission in experimental cases involving less fissile systems. Also, there was

no strong sensitivity for entrance channel mass-asymmetry on exit channel on systems with low values of fissility.

Further, we studied on the factors which enhance the fusion and thereby the production of heavy nuclei. We found that the positive Q-values of neutron transfer have a significant role in fusion enhancement. We observed that, systems that show an increase in deformations of the colliding nuclei after neutron transfer exhibit fusion enhancement. The increase in deformation after neutron transfer may lead to decrease in fusion barrier height and thereby increase the heavy element production.

The factors leading to fusion hindrances and enhancements in the heavy ion reactions also apply to super-heavy element production. This information will be vital during super heavy elements production.

Bibliography

[1] R. Rafiei, R. G. Thomas, D. J. Hinde, M. Dasgupta, C. R. Morton, L. R. Gasques, M. L. Brown, and M. D. Rodriguez, Phys. Rev. C **77**, 024606 (2008).

[2] A. C. Berriman, D. J. Hinde, M. Dasgupta, C. R. Morton, R. D. Butt, and J. O. Newton, Nature **413** (2001).

[3] L. Corradi, B. R. Behera, E. Fioretto, A. Gadea, A. Latina, A. M. Stefanini, S. Szilner, M. Trotta, Y. Wu, S. Beghini, G. Montagnoli, F. Scarlassara, R. N. Sagaidak, S. N. Atutov, B. Mai, G. Stancari, L. Tomassetti, E. Mariotti, A. Khanbekyan, and S. Veronesi, Phys. Rev. C **71**, 014609 (2005).

[4] A. Shamlath, E. Prasad, N. Madhavan, P. V. Laveen, J. Gehlot, A. K. Nasirov, G. Giardina, G. Mandaglio, S. Nath, T. Banerjee, A. M. Vinodkumar, M. Shareef, A. Jhingan, T. Varughese, D. Kumar, P. S. Devi,

Khushboo, P. Jisha, N. Kumar, M. M. Hosamani, and S. Kailas, Phys. Rev. C **95**, 034610 (2017).

[5] A. Shamlath, M. Shareef, E. Prasad, P. Sugathan, R. Thomas, A. Jhingan, S. Appannababu, A. Nasirov, A. Vinodkumar, K. Varier, C. Yadav, B. Babu, S. Nath, G. Mohanto, I. Mukul, D. Singh, and S. Kailas, Nuclear Physics A **945**, 67 (2016).

[6] R. N. Sagaidak, G. N. Kniajeva, I. M. Itkis, M. G. Itkis, N. A. Kondratiev, E. M. Kozulin, I. V. Pokrovsky, A. I. Svirikhin, V. M. Voskressensky, A. V. Yeremin, L. Corradi, A. Gadea, A. Latina, A. M. Stefanini, S. Szilner, M. Trotta, A. M. Vinodkumar, S. Beghini, G. Montagnoli, F. Scarlassara, D. Ackermann, F. Hanappe, N. Rowley, and L. Stuttgé, Phys. Rev. C **68**, 014603 (2003).

[7] W. Reisdorf, Z. Phys. A. **300**, 227 (1981).

[8] G. Mandaglio, A. Anastasi, F. Curciarello, G. Fazio, G. Giardina, and A. K. Nasirov, Phys. Rev. C **98**, 044616 (2018).

[9] M. Beckerman, Reports on Progress in Physics **51**, 1047 (1988).

[10] K. Hagino and N. Takigawa, Progress of Theoretical Physics **128**, 1061 (2012).

[11] V. V. Sargsyan, G. G. Adamian, N. V. Antonenko, W. Scheid, and H. Q. Zhang, Phys. Rev. C **91**, 014613 (2015).

[12] J. R. Leigh, J. J. M. Bokhorst, D. J. Hinde, and J. O. Newton, Journal of Physics G: Nuclear Physics **14**, L55 (1988).

[13] M. Trotta, A. M. Stefanini, L. Corradi, A. Gadea, F. Scarlassara, S. Beghini, and G. Montagnoli, Phys. Rev. C **65**, 011601 (2001).